NASA/CR–2015-218704/Volume III

Subsonic Ultra Green Aircraft Research: Phase II – Volume III – Truss Braced Wing Aeroelastic Test Report

Marty K. Bradley, Timothy J. Allen, and Christopher K. Droney
Boeing Research and Technology, Huntington Beach, California

April 2014

NASA STI Program . . . in Profile

Since its founding, NASA has been dedicated to the advancement of aeronautics and space science. The NASA scientific and technical information (STI) program plays a key part in helping NASA maintain this important role.

The NASA STI program operates under the auspices of the Agency Chief Information Officer. It collects, organizes, provides for archiving, and disseminates NASA's STI. The NASA STI program provides access to the NTRS Registered and its public interface, the NASA Technical Reports Server, thus providing one of the largest collections of aeronautical and space science STI in the world. Results are published in both non-NASA channels and by NASA in the NASA STI Report Series, which includes the following report types:

- TECHNICAL PUBLICATION. Reports of completed research or a major significant phase of research that present the results of NASA Programs and include extensive data or theoretical analysis. Includes compilations of significant scientific and technical data and information deemed to be of continuing reference value. NASA counter-part of peer-reviewed formal professional papers but has less stringent limitations on manuscript length and extent of graphic presentations.

- TECHNICAL MEMORANDUM. Scientific and technical findings that are preliminary or of specialized interest, e.g., quick release reports, working papers, and bibliographies that contain minimal annotation. Does not contain extensive analysis.

- CONTRACTOR REPORT. Scientific and technical findings by NASA-sponsored contractors and grantees.

- CONFERENCE PUBLICATION. Collected papers from scientific and technical conferences, symposia, seminars, or other meetings sponsored or co-sponsored by NASA.

- SPECIAL PUBLICATION. Scientific, technical, or historical information from NASA programs, projects, and missions, often concerned with subjects having substantial public interest.

- TECHNICAL TRANSLATION. English-language translations of foreign scientific and technical material pertinent to NASA's mission.

Specialized services also include organizing and publishing research results, distributing specialized research announcements and feeds, providing information desk and personal search support, and enabling data exchange services.

For more information about the NASA STI program, see the following:

- Access the NASA STI program home page at http://www.sti.nasa.gov

- E-mail your question to help@sti.nasa.gov

- Phone the NASA STI Information Desk at 757-864-9658

- Write to:
  NASA STI Information Desk
  Mail Stop 148
  NASA Langley Research Center
  Hampton, VA 23681-2199

NASA/CR–2015-218704/Volume III

Subsonic Ultra Green Aircraft Research: Phase II – Volume III – Truss Braced Wing Aeroelastic Test Report

Marty K. Bradley, Timothy J. Allen, and Christopher K. Droney
Boeing Research and Technology, Huntington Beach, California

National Aeronautics and
Space Administration

Langley Research Center
Hampton, Virginia 23681-2199

Prepared for Langley Research Center
under Contract NNL08AA16B

April 2014

Available from:

NASA STI Program / Mail Stop 148
NASA Langley Research Center
Hampton, VA 23681-2199
Fax: 757-864-6500

Abstract

This Test Report summarizes the Truss Braced Wing (TBW) Aeroelastic Test (Task 3.1) work accomplished by the Boeing Subsonic Ultra Green Aircraft Research (SUGAR) team, which includes the time period of February 2012 through June 2014. The team consisted of Boeing Research and Technology, Boeing Commercial Airplanes, Virginia Tech, and NextGen Aeronautics.

The model was fabricated by NextGen Aeronautics and designed to meet dynamically scaled requirements from the sized full scale TBW FEM. The test of the dynamically scaled SUGAR TBW half model was broken up into open loop testing in December 2013 and closed loop testing from January 2014 to April 2014. Results showed the flutter mechanism to primarily be a coalescence of 2nd bending mode and 1st torsion mode around 10 Hz, as predicted by analysis. Results also showed significant change in flutter speed as angle of attack was varied. This non-linear behavior can be explained by including preload and large displacement changes to the structural stiffness and mass matrices in the flutter analysis. Control laws derived from both test system ID and FEM19 state space models were successful in suppressing flutter. The control laws were robust and suppressed flutter for a variety of Mach, dynamic pressures, and angle of attacks investigated.

Acknowledgements

This project and report reflect the combined efforts of the SUGAR team. The team members are Boeing Research and Technology, Boeing Commercial Airplanes, the Virginia Institute of Technology, and NextGen Aeronautics. The coordinated effort of this team has produced this final report.

Funding for this effort is provided by the NASA Fundamental Aeronautics Program, through the Subsonic Fixed Wing organization. The contract number is NNL08AA16B task order NNL11AA00T.

The team would like to thank Erik Olson of the NASA Langley Research Center for his guidance as the NASA Contracting Officer Technical Representative (COTR), and the task technical advisor (TA) Bob Bartels. Additionally, Rob Scott provided significant expertise for the aeroelastic analysis and test activities.

Table of Contents

List of Tables and Figures

Tables

Figures

1.0 Introduction

This test report documents the SUGAR TBW aeroelastic wind tunnel test (Task 3.1) which was conducted in the NASA TDT from Dec 2013 through April 2014. The basis for this test was the detailed FEM sizing/optimization performed in Task 2.1. This task produced a detailed FEM which met all strength, buckling, and flutter constraints. The results showed significant structural weight benefits of a truss-braced wing with minimal weight penalty to pass flutter.

The primary goal of the aeroelastic wind tunnel task was to validate the flutter results. The secondary goal was to investigate benefits of closed loop flutter suppression control laws. For assessing flutter suppression, the objective was to quantify the flutter speed increases and investigate control law effect on gust loads.

The Task 2.1 model chosen for the wind tunnel test is the configuration which has the strut attached at the front spar and sized with 1.09Vd flutter constraints. The 1.09Vd model is slightly softer than the full flutter margin 1.15Vd model and therefore should facilitate the demonstration of aeroelastic instabilities in the tunnel. The V strut configuration which has a strut attached to the wing front spar and another strut attached to the rear spar showed the most structural weight benefit. This configuration wasn't chosen for the test due to concerns about drag and aerodynamic interference of the extra strut. Validating the flutter results for the front spar configuration should validate the flutter results on the V strut configuration since both analyses use the same methods.

The test was done on a dynamically scaled half model in R134 heavy gas. Dynamically scaled components include the wing, strut, and jury. Nearly rigid components include the fuselage, flow through nacelle, and engine pylon. The model was fixed on the electronic turn table which allowed angle of attack to vary. The model was tested open looped and closed looped using a hydraulically actuated inboard and outboard control surface. The model was instrumented with 22 accelerometers, 10 strain gages and 2 RVDT's to measure control surface deflection. Testing was done from Mach =.6 up to M=.94 for angles of attack from -3 to 5 degrees.

2.0 Dynamic Scale Factors and Requirements

The testing of the dynamically scaled aeroelastic side mounted half span model was conducted in R134 heavy gas at the Transonic Dynamics Tunnel (TDT) 16-by-16 foot transonic wind tunnel located at the Langley Research Center in Hampton, Virginia.

When building a dynamic scaled wind tunnel model (WTM) several pieces of information, regarding the full scale aircraft, which must be determined before being transmitted to the model vendor. Those items are aircraft geometry, mass, stiffness and most importantly the scaling factors.

The model dynamic scaling was selected to balance several considerations including TDT operating envelope, TDT test section size, and model manufacturability. Once the basic scale factors (length, density, and velocity) are determined the remaining are derived via the relations shown in Table 2.1. Scale factors for the test are shown in Table 2.2.

The detailed structural finite element model (FEM), shown in Figure 2.1, was used as the starting point for the SUGAR wind tunnel model. This full scale FEM has a 170ft span. The FEM was developed for calculating structural loads and performing structural design, and is based on the Outer Mold Lines (OMLs) defined by the aerodynamics group. The FEM mesh was defined sufficient to capture potential local buckling behavior and provide good stress results and detailed control surface models were incorporated. The target (baseline) equivalent beam stiffnesses were calculated to match the stiffness distributions of the detailed FEM model. Equivalent beam full scale wing, strut and jury stiffness for scaling are shown in Figure 2.2 through Figure 2.4 The figures also show the elastic axis location of the equivalent beams.

The baseline component mass summary, for the half span full scale model, is shown in Figure 2.5. The mass of the wing was broken into 19 sections with the control surfaces separated into additions sections as shown in Figure 2.6. The weight, C.G. and inertia for each section matching the full fuel mass case is listed in Table 2.3. In order to meet the stiffness requirements for the strut & jury, the target scaled weight could not be met. So, an estimate of the model beam's weights (strut & jury) was scaled to full size thus requiring ~1490 lbs to be added to the detailed FEM. The strut and jury section breakdown and mass distribution are shown in Figure 2.7 and Table 2.4, respectively.

The goal of the analysis was to make a beam-rod FEM to become the "as built" analytical model of WTM. This analytical model would be used in all aspects of aeroelastic analyses to verify that the model was safe to operate in the wind tunnel. The first step in achieving this goal was to create full scale beam-rod FEM using the mass and stiffness that was presented in the previous section. A comparison of the full scale Detailed FEM and the Beam-Rod FEM is shown Figure

2.8. Flutter results of these two full scale FEMs are shown in Figure 2.9; the Beam-Rod results match the Detailed FEM very well.

The second step toward achieving an "as built" analytical model, was done by applying the scaling factors to the full scale model thus "shrinking it" to the same size as the WTM. Coordinating with the model vendor was critical in order to determine what was achievable and match what is being designed and manufactured. The "as built" FEM was updated as the design matured; a history of FEM evolution is shown in Table 2.5. Analysis was conducted throughout the model construction time period and updates to the "as built" FEM were being made.

The SUGAR WTM was attached to the Oscillating Turntable (OTT) mount residing on the east side of the TDT test section. A beam-rod FEM of the OTT was provided by NASA so it could be incorporated into the analysis. Wind tunnel boundary conditions have been studied to try and keep similitude with the free flying vehicle symmetric flutter mechanism. A comparison of flutter results for the free free detailed FEM and half model of the detailed FEM with the wind tunnel boundary conditions are shown in Figure 2.10. Flutter speeds have changed but the flutter mechanism is still a combination of the same primary modes. Also, as shown in Figure 2.11, the wind tunnel boundary conditions cause a small change in primary mode shapes but the modes are similar to the free free modes. The z deflection for the plots is the average front and rear spar deflection. The torsional slope is the difference between the z defection at the front spar and rear spar divided by the x distance between the spars. Since we have good similitude with the fixed boundary conditions we were able to simplify the test versus a free flying model or a pitch and plunge free arrangement.

2.1 Full Scale vs. Test Scale Configuration Differences

This section describes configuration differences between the full scale analysis model and the test model. First, as shown in Figure 2.12 tunnel integration concerns required a fuselage length reduction from 18.7 ft to 13.4 ft. This change had no appreciable effect on the flutter results. The engine/nacelle position was moved 12.5 inches aft and 5 inches down. The tested position is a more realistic position for the engine/pylon. This difference did change the flutter solution but didn't change the primary flutter mechanism. Finally, as the test analysis model was updated to the as built mass distribution the unstable flutter damping decreased to the point where it might not be larger than the inherent structural damping. Therefore, as shown in Figure 2.13, six ballast weights of just under 3 lbs each were added to aft section of the main spar. The ballast weights brought the flutter damping back to an acceptable value.

Table 2.1 – SUGAR Wind Tunnel Model Scale Factor Equations

Item	Equation
Basic Scale Factors	
LENGTH (Lm/Lp)	λ
DENSITY (ρm/ρp)	ρ
VELOCITY (Vm/Vp)	v
Derived Scale Factors	
DYNAMIC PRESSURE (qm/qp)	λv^2
MASS (Mm/Mp)	ρ λ^3
STATIC UNBALANCE (Sm/Sp)	ρ λ^4
MOMENT OF INERTIA (Im/Ip)	ρ λ^5
FREQUENCY (ωm/ωp)	v/ λ
TIME (Tm/Tp)	λ/v
SPRING CONSTANTS	
LINEAR (Khm/Khp) ROTATIONAL	ρλ^4v^2
ROTATIONAL (Kθm/Kθp)	ρλ^4v^2
STIFFNESS	
BENDING (EIm/EIp)	ρλ^4v^2
TORSION (GJm/GJp)	ρλ^4v^2
FORCE (Fm/Fp)	ρλ^2v^2
ACCELERATION (Am/Ap)	v^2 / λ

Table 2.2 – Scale Factors

Full-Scale Data - Full Span Values					A (fps)
Weight (lb)	Span (ft)		Mach	Vel (KEAS)	549.5
143164	170		0.82	400	

Full-Scale Data - Half Span Values							
Weight (lb)	Span (ft)	Mach	Altitude (ft)	Dyn Pres (psf)	Density (s/cf)	Velocity (fps)	Re
29530	85	0.8200	15915.36	542.47	0.001451	864.56	4.35E+07

Basic Scale Factors			Derived Scale Factors					
Length	Density	Velocity	Mass	Acceleration	Force	Stiffness	Frequency	Dyn Pres
0.150	1.1000	0.5211	0.003713	1.8103	0.006721	1.5122E-04	3.4740	0.2987

Spring Constants		Moment of Inertia	Time
Linear	Rotational		
0.0448050	0.001008	8.35313E-05	0.287852619

Model-Scale Data						
Weight (lb)	Span (ft)	Mach	n Pres (psf)	Density (s/cf)	Velocity (fps)	Re
109.63	12.75	0.820	162.03	0.001597	450.52	5.07E+06

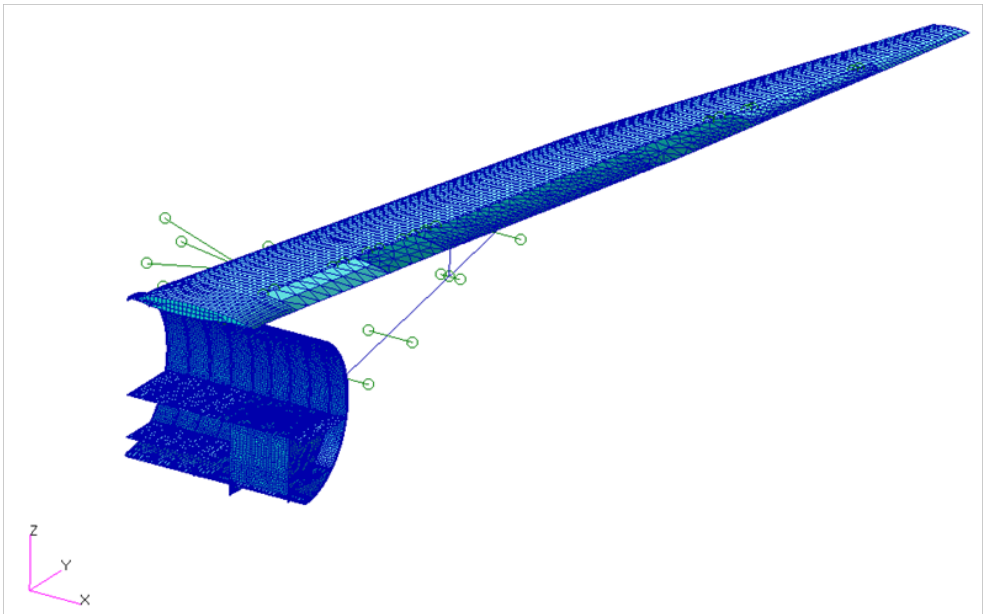

Figure 2.1 – SUGAR Detailed FEM

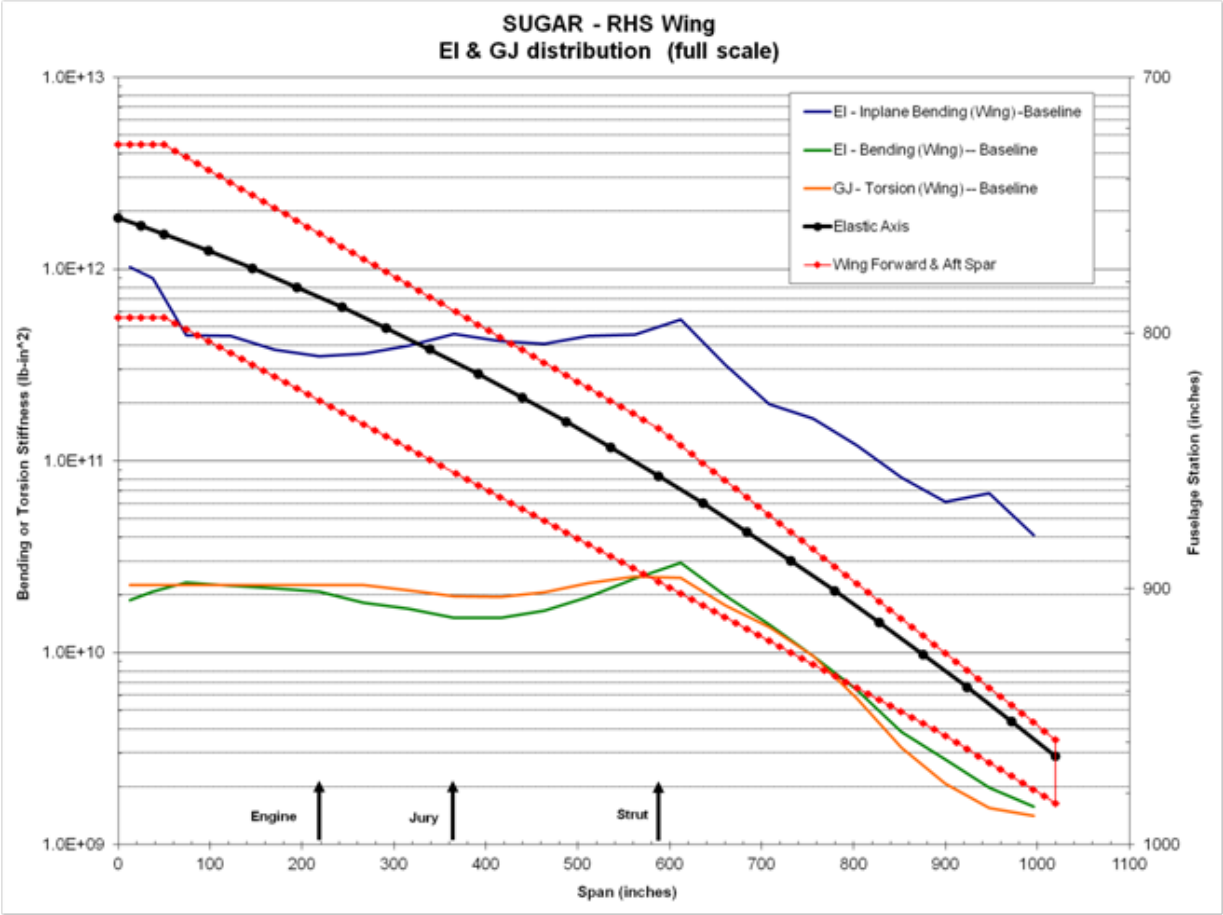

Figure 2.2 – Full Scale Wing Stiffness

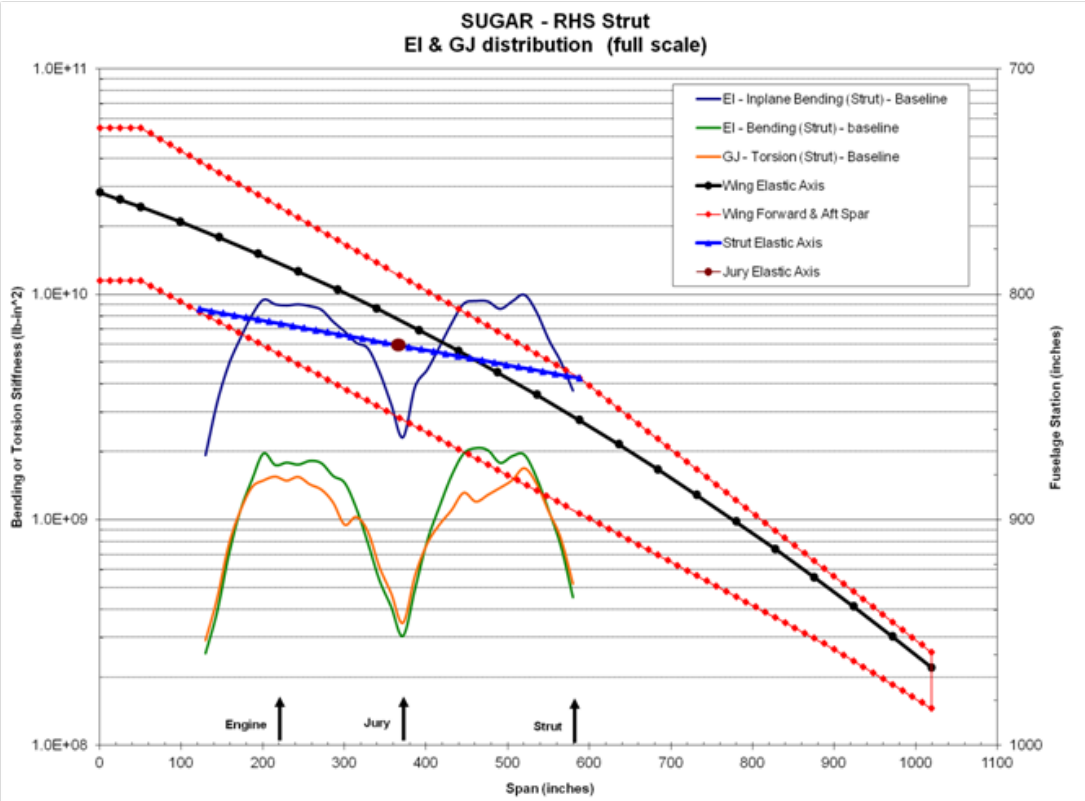

Figure 2.3 – Strut Full Scale Stiffness

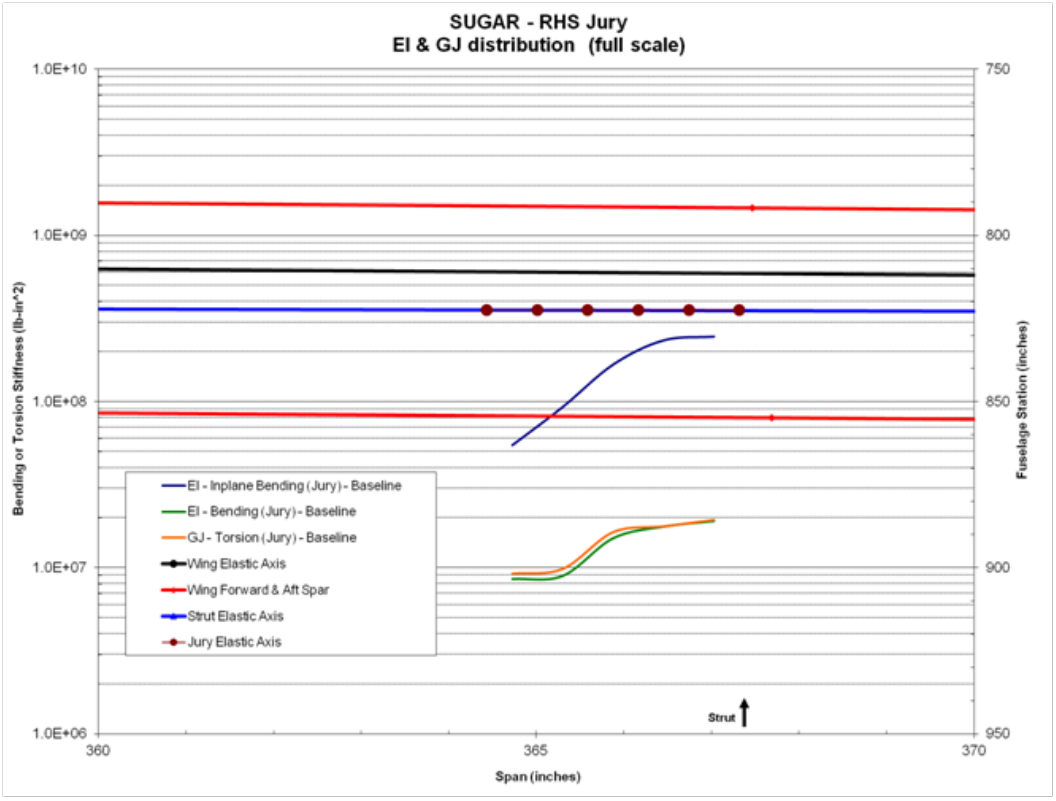

Figure 2.4 – Jury Full Scale Stiffness

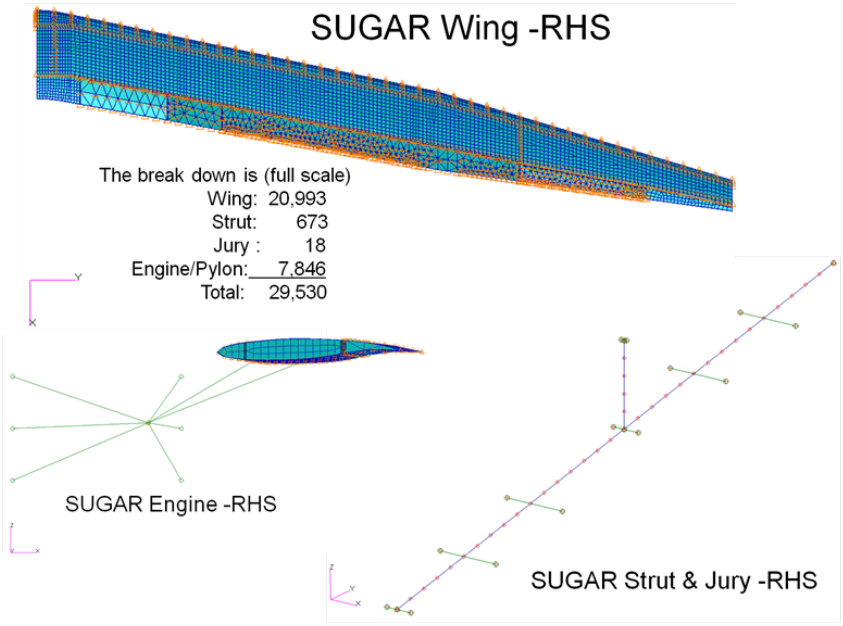

Figure 2.5 – SUGAR Baseline Mass Component Summary

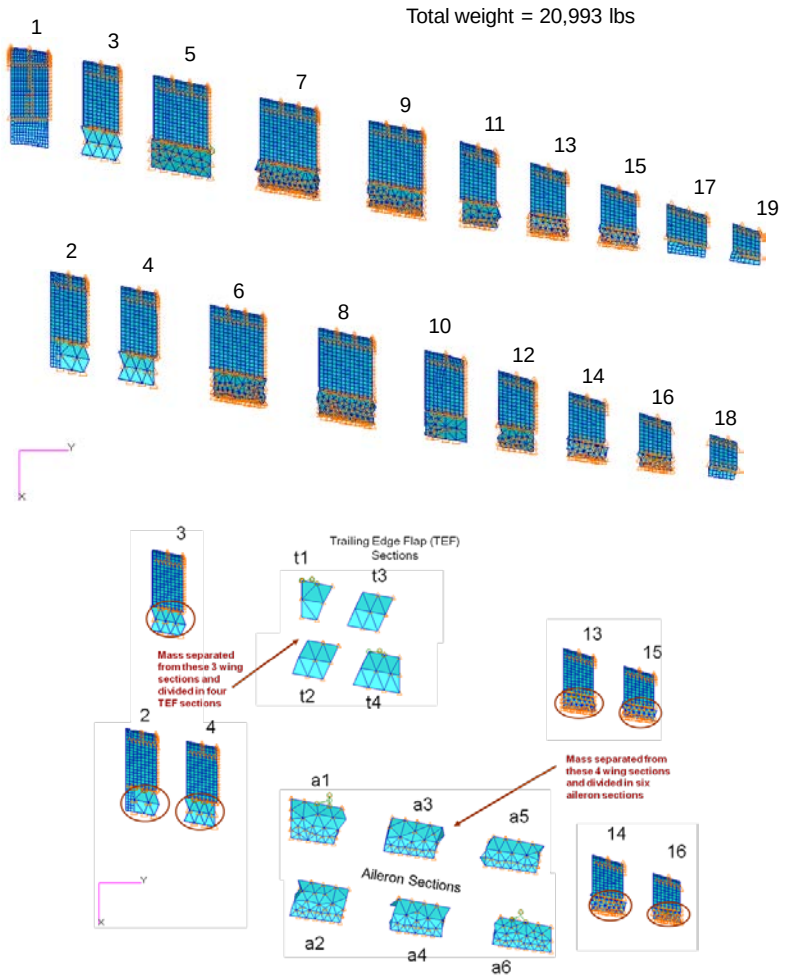

Figure 2.6 – Wing and Control Surface Mass Section Breakdown

Table 2.3 – Wing Full Scale Mass Distribution

DESCRIPTION			WT (LBS)	F.S. (X)	B.L. (Y)	W.L. (Z)	IROLL (IX)	IPITCH (IY)	IYAW (IZ)
Wing	Section	1	1732.10	761.52	33.56	302.61	414592	1237980	1558053
Wing	Section	2	1374.30	768.23	83.13	298.57	280058	794038	1027237
Wing	Section	3	1329.50	776.43	131.85	297.01	251223	704068	913964
Wing	Section	4	1327.20	785.79	179.88	295.69	251777	690313	900334
Wing	Section	5	2157.80	801.35	239.68	294.54	1005435	1421339	2346573
Wing	Section	6	2072.90	815.35	312.71	292.53	892266	1335313	2152403
Wing	Section	7	2078.20	830.71	387.65	290.82	938457	1343348	2199588
Wing	Section	8	1985.50	846.16	460.80	289.15	866233	1295008	2078732
Wing	Section	9	2043.40	860.42	532.84	287.36	919577	1319290	2148786
Wing	Section	10	1450.60	868.95	595.91	285.52	313832	799207	1049634
Wing	Section	11	357.00	887.68	637.46	289.40	80032	318255	380653
Wing	Section	12	1337.10	896.36	702.13	286.97	223995	529852	698115
Wing	Section	13	243.40	901.77	733.21	286.37	52765	110728	153522
Wing	Section	14	199.40	910.31	781.44	284.79	43796	75763	112549
Wing	Section	15	171.80	922.09	829.03	283.44	36923	57931	90009
Wing	Section	16	126.30	933.02	873.32	282.06	19781	36285	53004
Wing	Section	17	200.90	947.87	921.66	280.79	54768	58943	110049
Wing	Section	18	119.50	959.00	967.01	279.58	13811	27294	39380
Wing	Section	19	150.00	966.98	1004.00	278.48	19709	25854	43664
TEF	Section	t1	69.30	814.31	76.61	304.55	9989	12679	21055
TEF	Section	t2	65.20	822.91	109.82	303.67	8940	11011	18588
TEF	Section	t3	64.60	828.85	141.77	302.96	8587	10819	18088
TEF	Section	t4	82.60	836.61	176.58	302.15	12297	14871	25729
Aileron	Section	a1	50.10	940.41	722.68	288.33	4825	3619	8106
Aileron	Section	a2	42.20	947.17	753.11	287.33	3625	2308	5700
Aileron	Section	a3	39.20	951.87	783.54	286.46	3144	2051	4997
Aileron	Section	a4	34.30	956.32	812.44	285.45	2430	1586	3872
Aileron	Section	a5	39.30	961.96	844.33	284.30	4324	1560	5757
Aileron	Section	a6	49.20	966.28	877.78	283.18	4531	1895	6256
TOTAL			20992.90	829.44	374.86	292.06	6741722	12243208	18174397

MOMENTS OF INERTIA (ABOUT C.G.)

IROLL=	1163434294	LB*IN^2 OR	251116	SLUG*FT^2
IPITCH=	63430994	LB*IN^2 OR	13691	SLUG*FT^2
IYAW=	1224772528	LB*IN^2 OR	264355	SLUG*FT^2

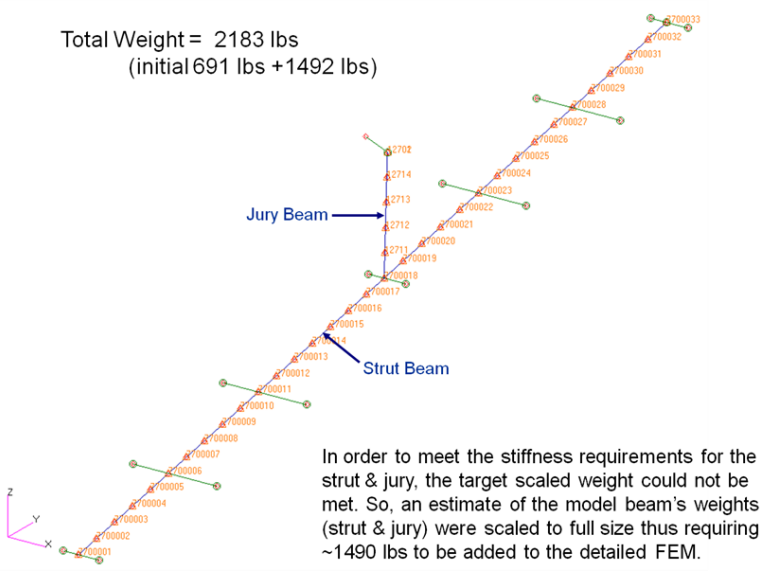

Figure 2.7 – Strut and Jury Section Breakdown

Table 2.4 – Strut and Jury Full Scale Mass Distribution

DESCRIPTION		WT (LBS)	F.S. (X)	B.L. (Y)	W.L. (Z)	IROLL (IX)	IPITCH (IY)	IYAW (IZ)
----------	Strut Beam	433.60	822.07	357.82	221.11	8278872	607422	7762777
ID: 7700001	CONM2 #1	52.18	806.60	122.75	158.34	0	0	0
ID: 7700002	CONM2 #2	52.18	807.54	136.96	162.13	0	0	0
ID: 7700003	CONM2 #3	52.18	808.47	151.18	165.93	0	0	0
ID: 7700004	CONM2 #4	52.18	809.41	165.40	169.73	0	0	0
ID: 7700005	CONM2 #5	52.18	810.34	179.62	173.52	0	0	0
ID: 7700006	CONM2 #6	52.18	811.28	193.83	177.32	0	0	0
ID: 7700007	CONM2 #7	52.18	812.21	208.05	181.12	0	0	0
ID: 7700008	CONM2 #8	52.18	813.15	222.27	184.91	0	0	0
ID: 7700009	CONM2 #9	52.18	814.08	236.48	188.71	0	0	0
ID: 7700010	CONM2 #10	52.18	815.02	250.70	192.51	0	0	0
ID: 7700011	CONM2 #11	52.18	815.96	264.92	196.30	0	0	0
ID: 7700012	CONM2 #12	52.18	816.89	279.14	200.10	0	0	0
ID: 7700013	CONM2 #13	52.18	817.83	293.35	203.90	0	0	0
ID: 7700014	CONM2 #14	52.18	818.76	307.57	207.69	0	0	0
ID: 7700015	CONM2 #15	52.18	819.70	321.79	211.49	0	0	0
ID: 7700016	CONM2 #16	52.18	820.63	336.00	215.29	0	0	0
ID: 7700017	CONM2 #17	52.18	821.57	350.22	219.08	0	0	0
ID: 7700018	CONM2 #18	52.18	822.50	364.44	222.88	0	0	0
ID: 7700019	CONM2 #19	52.18	823.48	379.33	226.86	0	0	0
ID: 7700020	CONM2 #20	52.18	824.46	394.22	230.83	0	0	0
ID: 7700021	CONM2 #21	52.18	825.44	409.11	234.81	0	0	0
ID: 7700022	CONM2 #22	52.18	826.42	424.00	238.78	0	0	0
ID: 7700023	CONM2 #23	52.18	827.40	438.89	242.76	0	0	0
ID: 7700024	CONM2 #24	52.18	828.38	453.78	246.74	0	0	0
ID: 7700025	CONM2 #25	52.18	829.36	468.67	250.71	0	0	0
ID: 7700026	CONM2 #26	52.18	830.34	483.56	254.69	0	0	0
ID: 7700027	CONM2 #27	52.18	831.32	498.44	258.67	0	0	0
ID: 7700028	CONM2 #28	52.18	832.30	513.33	262.64	0	0	0
ID: 7700029	CONM2 #29	52.18	833.28	528.22	266.62	0	0	0
ID: 7700030	CONM2 #30	52.18	834.26	543.11	270.59	0	0	0
ID: 7700031	CONM2 #31	52.18	835.24	558.00	274.57	0	0	0
ID: 7700032	CONM2 #32	52.18	836.22	572.89	278.55	0	0	0
ID: 7700033	CONM2 #33	52.18	837.20	587.78	282.52	0	0	0
----------	Jury Beam	11.50	822.50	366.29	265.01	4260	4252	104
ID: 12701	CONM2 #1	5.00	822.50	367.32	288.31	0	0	0
ID: 12702	CONM2 #2	5.00	822.50	367.32	288.31	0	0	0
ID: 12711	CONM2 #3	1.50	822.50	367.32	288.31	0	0	0
ID: 12712	CONM2 #4	1.50	822.50	365.01	235.97	0	0	0
ID: 12713	CONM2 #5	1.50	822.50	365.59	249.05	0	0	0
ID: 12714	CONM2 #6	1.50	822.50	366.17	262.14	0	0	0
TOTAL		2182.94	818.23	352.27	219.48	8283132	611674	7762881

MOMENTS OF INERTIA (ABOUT C.G.)

IROLL=	45267561	LB*IN^2 OR	9771	SLUG*FT^2
IPITCH=	9999878	LB*IN^2 OR	2158	SLUG*FT^2
IYAW=	48420407	LB*IN^2 OR	10451	SLUG*FT^2

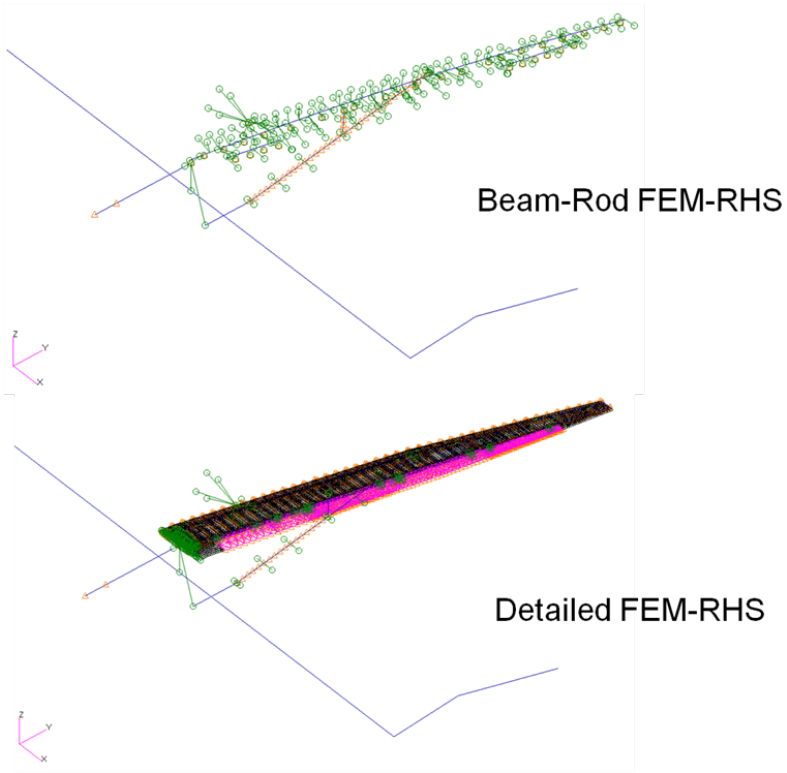

Figure 2.8 – Full Scale Beam Rod and Detailed FEMS

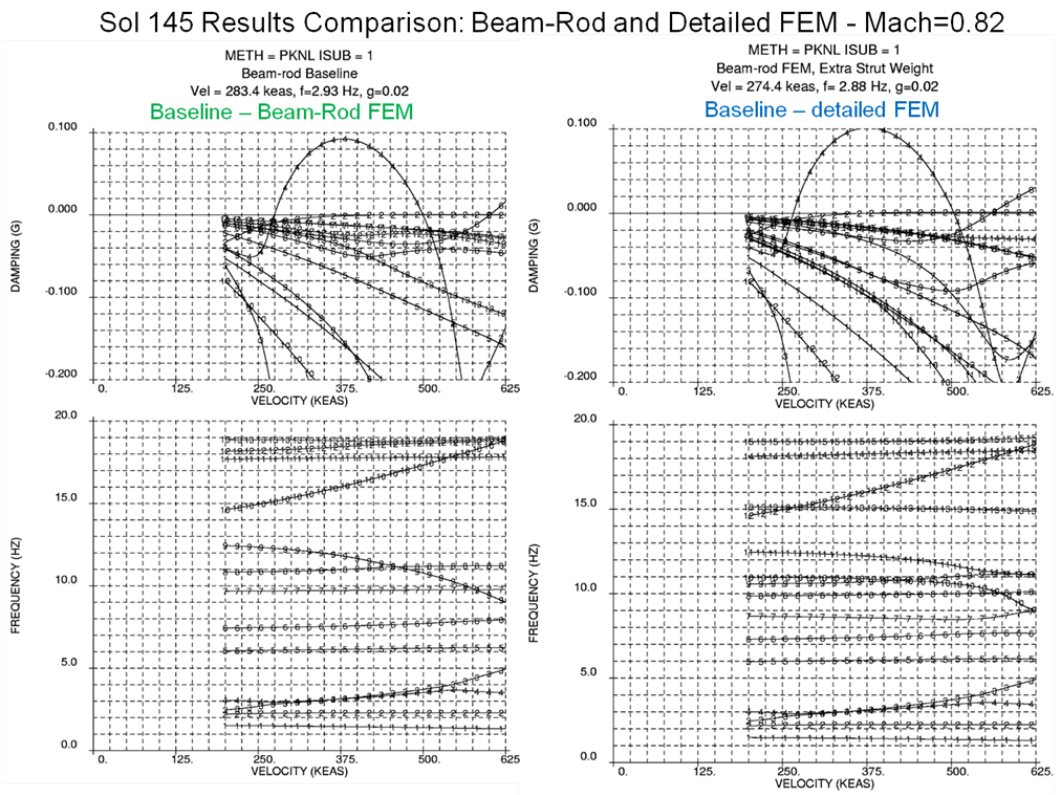

Figure 2.9 – Flutter Result Comparison of Full Scale Detailed FEM to Beam Rod FEM

Table 2.5 – Scaled Beam-Rod FEM History

$Revision history - NextGen

$ V2: strut root yaw spring removed
$ V3: reposition strut joint to match current CAD design
$ V4: update all wing group CONM2's to represent current CAD running mass actuals
$ V4: CONM2s revised include: 10701-10719, 13701-13704, 14701-14704
$ V5: update strut and jury group CONM2's to represent current CAD running mass actuals
$ V5: strut CONM2s: (7700001-7700033), jury CONM2: 12714
$ V6: update fuselage mass to 384 lbs, update strut root fuselage beam
$ V7: comprehensive mass model update

$ Brief Beam-Rod FEM history - Boeing

$ Scaled_FEM9 4/10/13
$ - TDT mount to wing spar at X=37.5
$
$ Scaled_FEM11 4/17/13
$ - consolidated PBAR cards (combine I1 I2 & J on one card)
$ - Added V4 CONM2 updates from NextGen
$
$ Scaled_FEM12 5/10/13
$ - TDT mount to wing spar at X=25.0
$
$ Scaled_FEM13 5/17/13
$ - Fixed Fuselage spline points, added more reduced frequencies (k's)
$ - updated Fuselage CAERO card to reflect wind tunnel model
$
$ Scaled_FEM14 6/4/13
$ - Added V5 CONM2 updates from NextGen
$ - PBARS Area values updated to as built
$ - Running SOL 145 with R134a Ref density
$ - updated Fuselage CAERO Card IDs
$
$ Scaled_FEM15 6/17/13
$ - Engine pylon changed to a CBEAM and the single CONM2 distributed to four
$ - Corrected OB Aileron HL and attachment to better match wind tunnel model
$ - Updated IB Aileron Grid points
$
$ Scaled_FEM16 7/11/13
$ - Update the IB and OB Aileron's Weight, I_{xx}, and Actuator stiffness to reflect
$ the "as built" properties. The delta changed in weight added back into wing CONM2's.
$ - The stiffness value for each control surface actuator is set to 120,298 in-lbs/rad.
$ - Corrected typo on MKAERO Card, two reduces frequencies.
$
$ Scaled_FEM17 8/3/13
$ - Added V6 & V7 updates from NextGen

$
$ Scaled_FEM19 1/10/14
$ - Initial FEM correlation to GVT results (WTM installed in the TDT test section, with tape)
$ - Removed the TDT mounting system; FEM is now cantilevered at GRID 40457
$ - Increased bending stiffness on wing elements and strut attachment beam by 6.6%
$ - Increased torsional stiffness on inner wing elements (10301 - 10309) by 10%
$
$ Scaled_FEM20 3/18/14
$ - Starting with FEM19
$ - Decreased bending stiffness on strut attachment beam (for Mode 3)
$ - Decreased bending stiffness on certain wing elements (for Mode 3)
$ - Increased bending stiffness on certain wing elements (for Modes 1 & 5)
$ - Maintained torsional stiffness on inner wing elements (for Mode 4

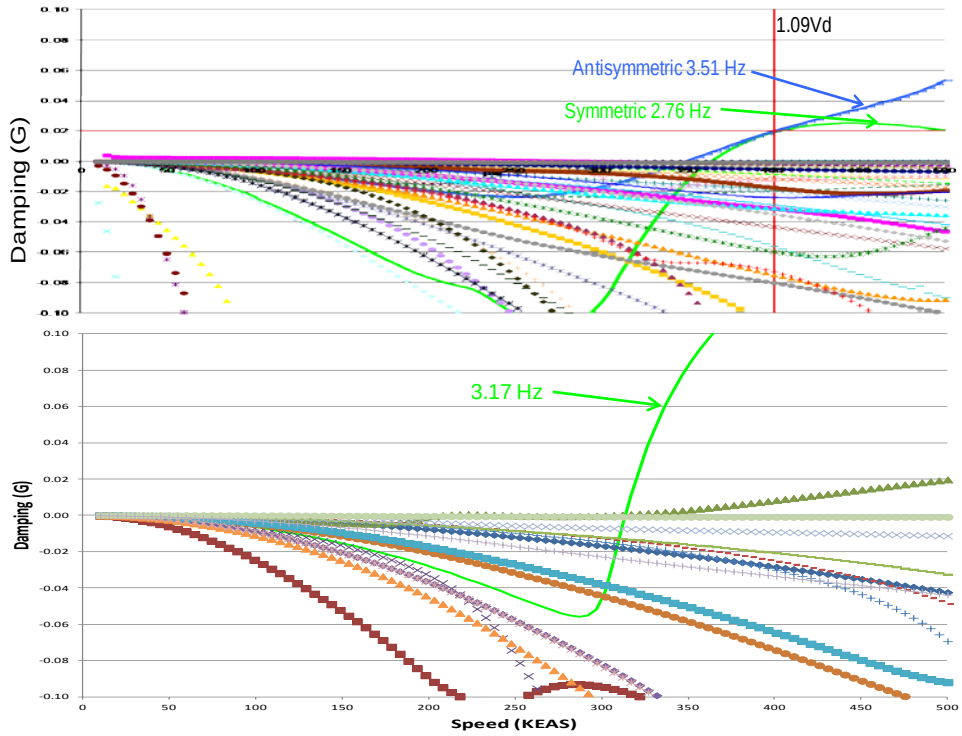

Free-Free

Wind Tunnel Boundary Conditions – Half Model

Figure 2.10 – Boundary Condition Study Flutter Comparison

Primary Bending Mode

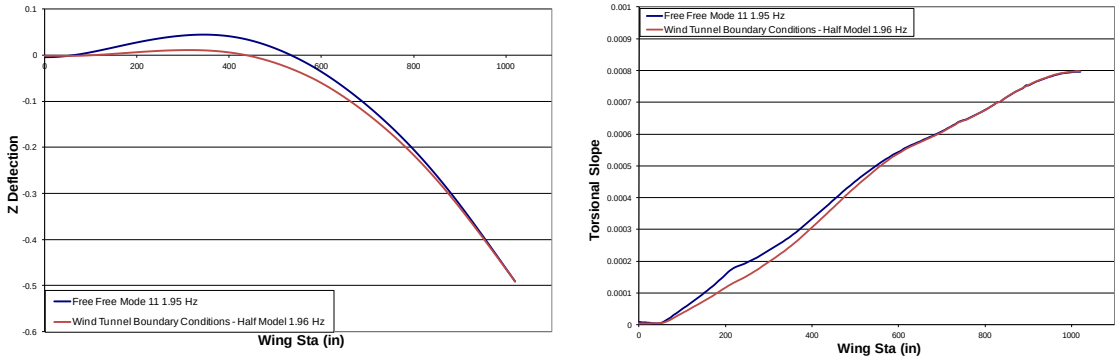

Z deflection is average front spar and rear spar deflection

Primary Torsion Mode

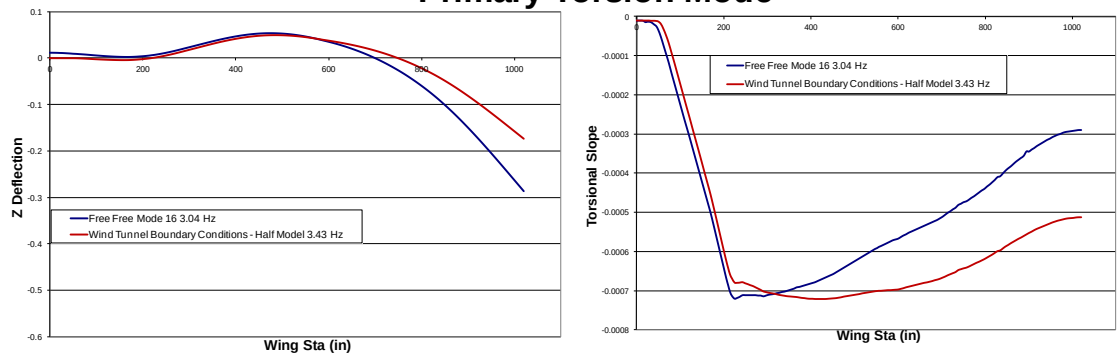

Torsional slope is difference between front and rear spar z deflections divided by the x distance between spars

Figure 2.11 – Boundary Condition Study Mode Shapes

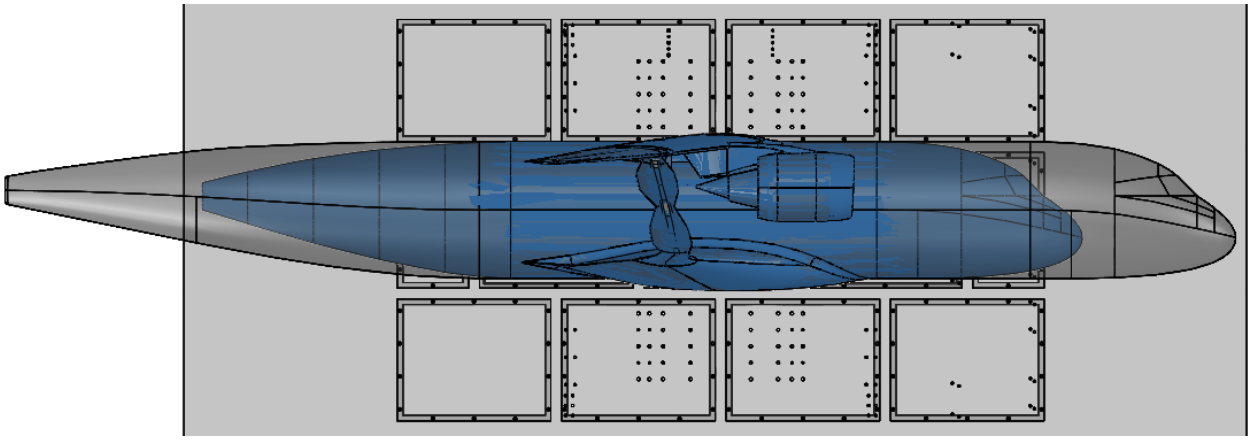

Figure 2.12 – Fuselage Length Reduction

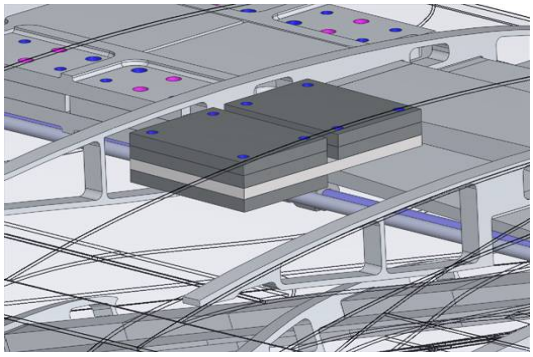

	Flutter mass design 9/17				Local inertia terms		
	Weight	Xcg	Ycg	Zcg	Ixx	Iyy	Izz
Location	lbs	in	in	in	lbs-in^2	lbs-in^2	lbs-in^2
1	2.92	123.22	40.77	45.06	1.80	4.10	5.50
2	2.92	124.35	46.61	44.91	1.81	4.10	5.50
3	2.92	126.56	58.89	44.58	1.80	4.10	5.50
4	2.92	127.75	67.60	44.44	1.75	4.15	5.50
5	2.92	129.66	77.32	44.20	1.81	4.10	5.50
6	2.92	132.95	91.17	43.63	2.01	4.09	5.50

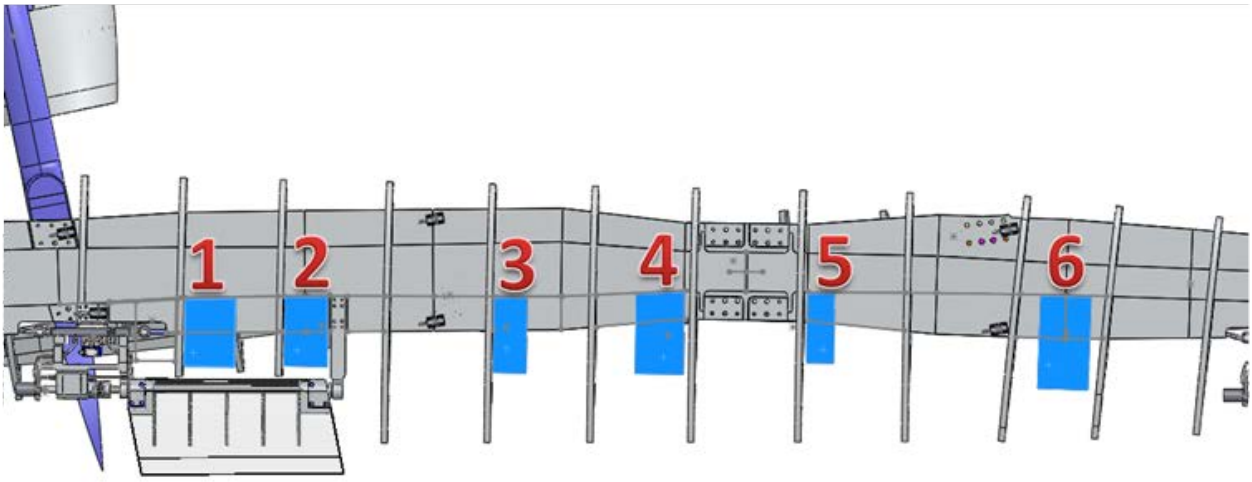

Figure 2.13 – Flutter Ballast Weights

3.0 Model Design and Analysis

The main features of the model are shown in Figure 3.1. The model features the cruciform wing and strut beam, h section jury beam, rigid fuselage, flow through nacelle, and 2 actively controlled trailing edge surfaces.

The model uses a classical flutter model construction approach, where a single internal beam represents the entire stiffness composition of a wing or strut member, and segmented skins are used for an aerodynamic fairing that does not contribute additional stiffness. The process used to develop equivalent beam cross-sections to meet the stiffness requirements is shown in Figure 3.2. The large span wing couldn't be machined as a single piece, so there are two wing beams with a joint in the middle. Stiffness requirements were met for the wing, strut, and jury. Mass requirements were met for the wing. Based on classic flutter model construction, model strut and jury mass estimates exceed scaled requirements. However, the extra mass was shown to be inconsequential to flutter results and acceptable for test.

Actuator system design (Figure 3.3) was based on the successful system used for a number of actively controlled flutter models, including the Boeing joined wing sensorcraft free-flying model, and consisted of a high flow Moog servovalve, a custom designed hydraulic actuator, a coupler, and a RDVT sensor. Large hinge moment and high bandwidth requirements for flutter suppression were challenges for the control system design. The coupler wasn't able to fit in the OML so a small cutout in the skin was made to accommodate it.

The mounting structure attaches to the electronic turn table and wing spar and strut as shown in Figure 3.4. A summary of the model instrumentation which included 22 accelerometers, 10 strain gages, and 2 RVDT's is shown in Figure 3.5. The model was designed to have the NASA model systems criteria required safety margin for the five design condition shown in Figure 3.6.

Validation testing included actuator characterization, coupling strength, strain gage calibration, mass property verification, and GVTs. Actuator characterization involved recording the control surface position as it was commanded to sweep through a range of frequencies. Results showed actuator performance was adequate for flutter suppression control laws. A test was completed to determine hinge moment capability of the coupler, as spatial constraints forced the selection of an undersized model. The coupler hinge moment capability is lower than the actuator and close to some conservatively derived maximum hinge moment requirements. The strain gages were calibrated by recording values with a known applied load, and correlation with the finite element analysis result of each test case. The same loads were applied at a few times during testing to make sure the strains didn't change. The model was weighted to make sure it matched the analysis model. GVTs were conducted in the model prep area, and in the tunnel with and without skin tape. There were also multiple GVTs over the course of the test to

verify that the model behavior was consistent. A comparison of the GVT results to the analysis model is documented in the test results section.

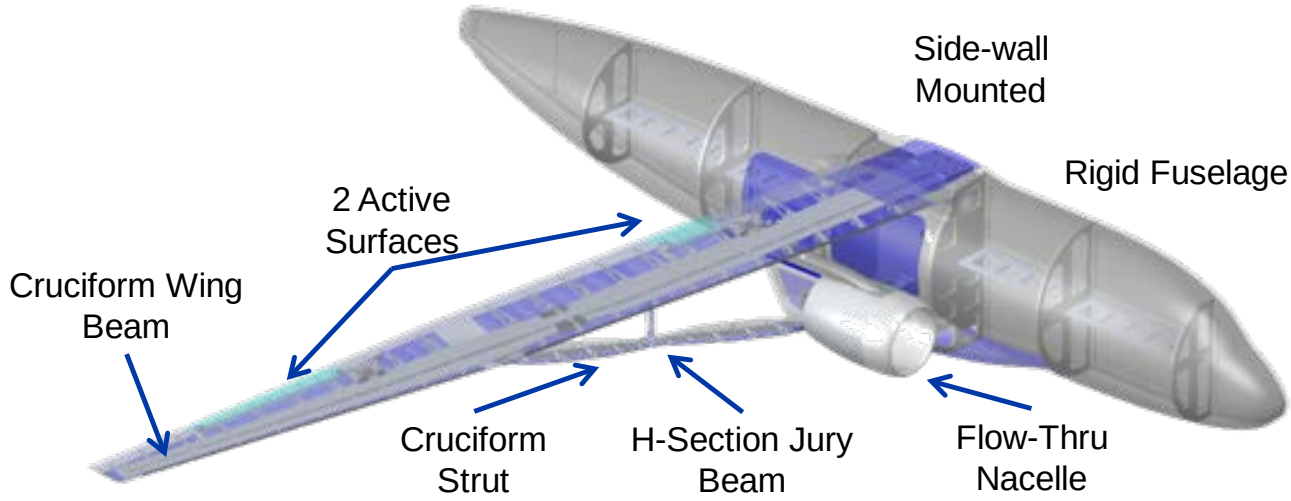

Figure 3.1 – Wind Tunnel Model Overview

Scaled Stiffness Targets → Section Solver → Initial CAD Layout

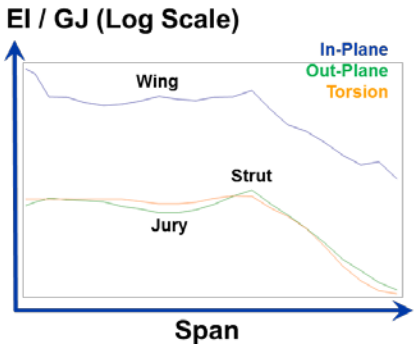

Y-location	out-plane	in-plane	torque
[in]	EI11	EI22	GJ
1.875	2.86E+06	1.55E+08	3.40E+06
5.636	3.15E+06	1.35E+08	3.40E+06
11.134	3.51E+06	6.83E+07	3.40E+06
18.344	3.38E+06	6.76E+07	3.40E+06
25.541	3.28E+06	5.75E+07	3.40E+06
32.823	3.16E+06	5.30E+07	3.40E+06

Boeing SUGAR - Cruciform Cross-Section Solver

	Center Block		Side Blocks	
Variables	2A	2B	2a	2b
[in]	0.817	0.382	0.214	0.101

Current Section Properties	Yna	Iopx	Iipz	J
	[in]	[in^4]	[in^4]	[in^4]
	NA	0.0038	0.029	0.0114

Target Section Properties	Yna	Iopx	Iipz	J
	[in]	[in^4]	[in^4]	[in^4]
	NA	0.0039	0.0293	0.0115

Section Property	Total	Iopx	Iipz	J
	[in]	[in^4]	[in^4]	[in^4]
Error	-9.7619E-08	-0.00004	-0.00029	-0.000115
Error %	-3.0	-1.00	-1.00	-1.00

Solver Constraints

Description	Variable	V > Than	V < Than
Total Height [in]	Htot	0.375	0.825
Total Width [in]	Wtot	0.500	9.000
Side Block Width [in]	Wsb	0.125	6.000
Side Block Thickness [in]	Tsb	0.100	0.101
Out-plane error [%]	Iopx	0.99	1.01
In-plane error [%]	Iipz	0.99	1.01
Torsional error [%]	J	0.99	1.01

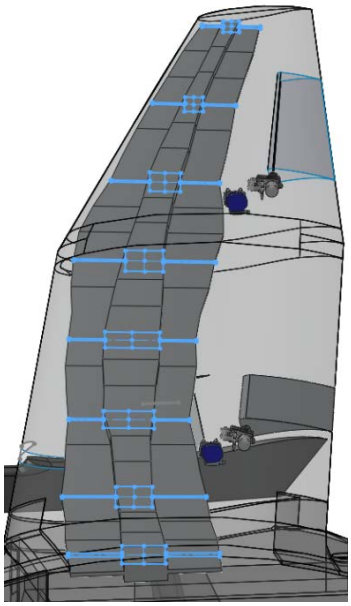

Figure 3.2 – Equivalent Beam Design

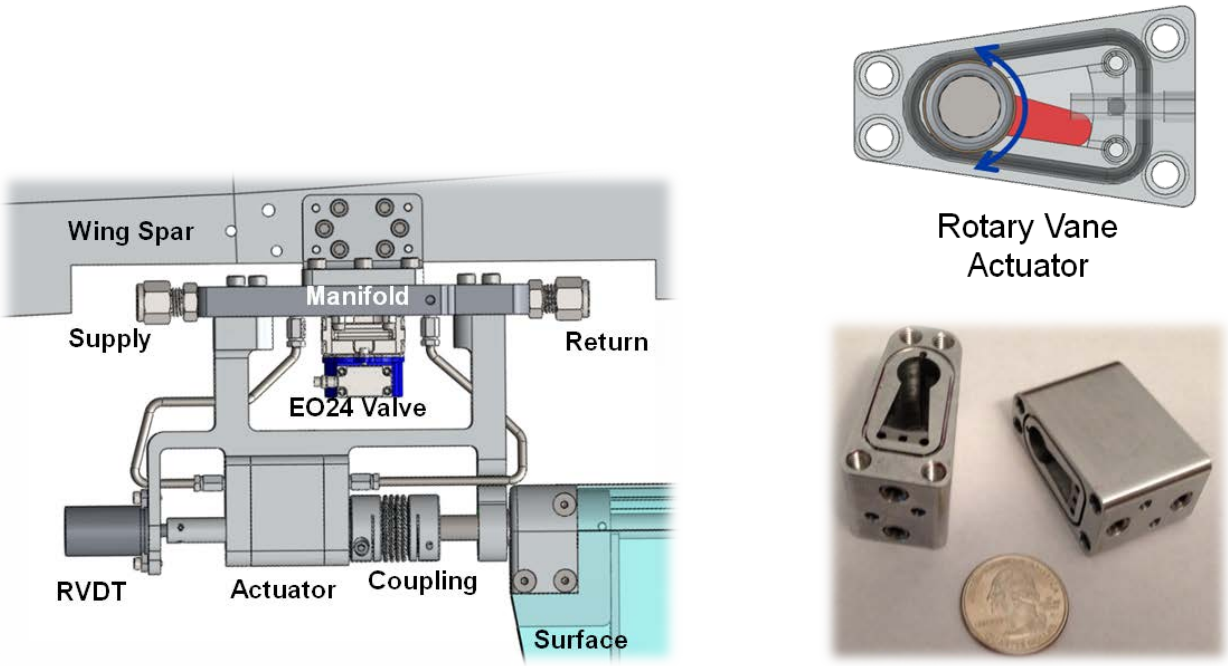

Figure 3.3 – Control System Design

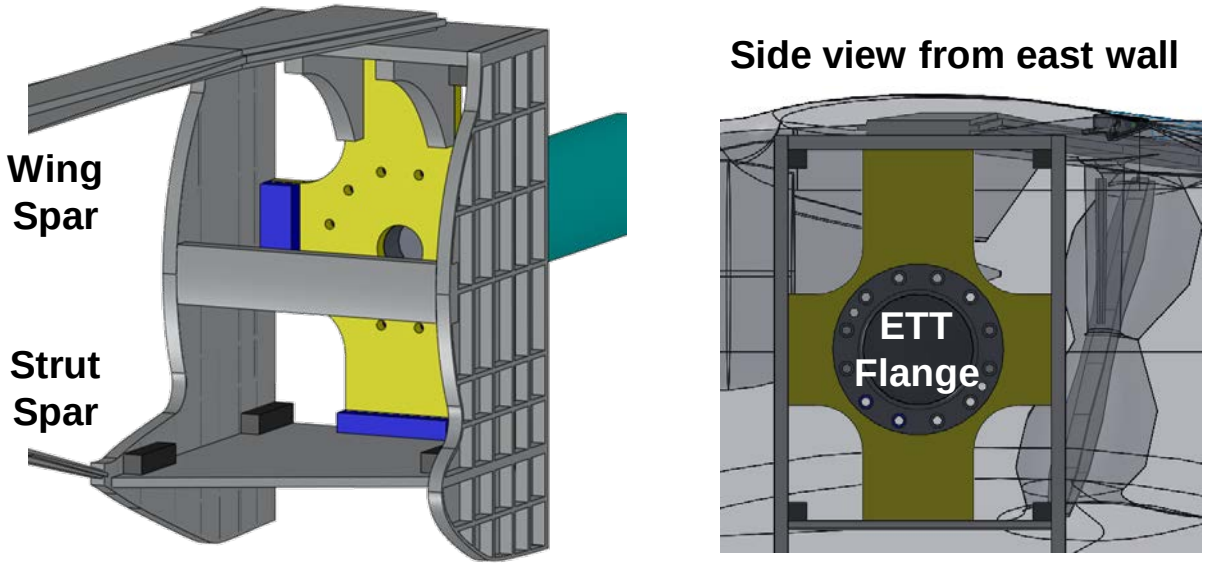

Figure 3.4 – Wind Tunnel Model Mounting Structure

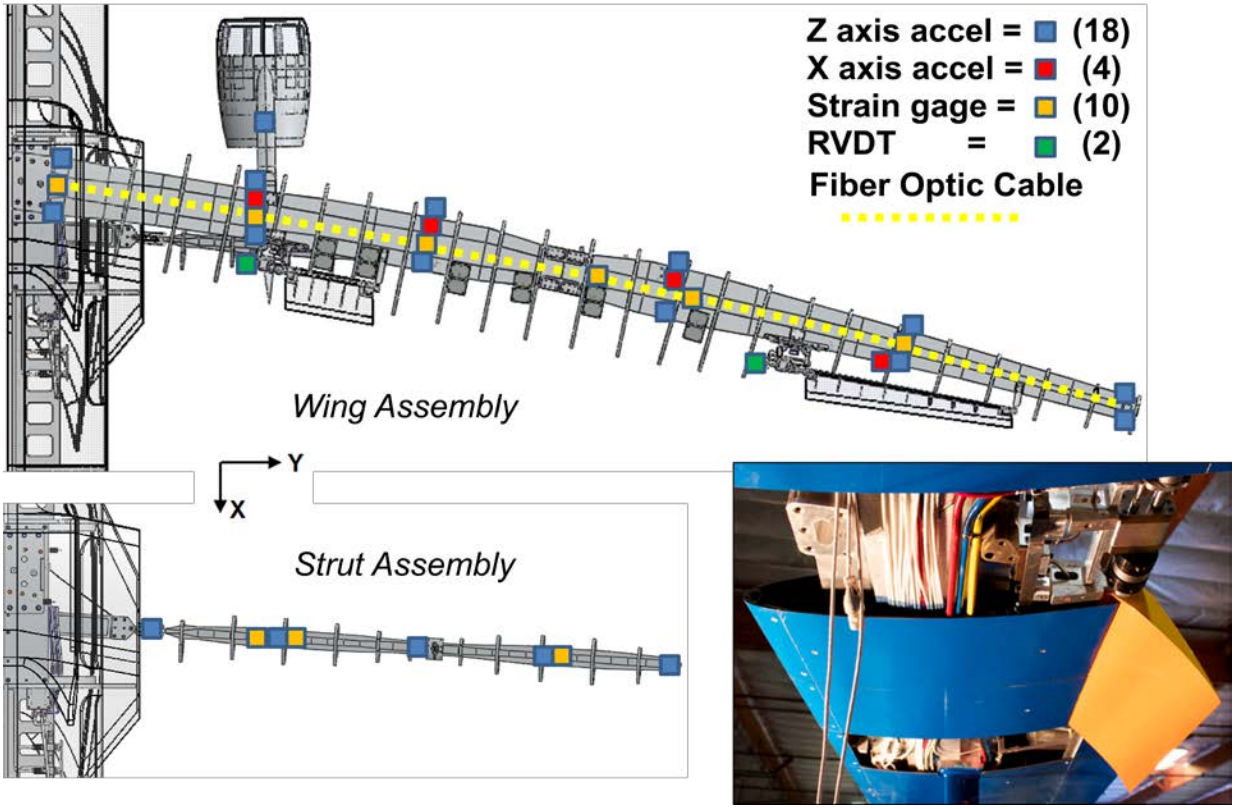

Figure 3.5 – Instrumentation Summary

- Case 1: Maximum bending at model mount attachment
- Case 2: Maximum bending at wing root & mid-spar joint
- Case 3: Maximum bending of outboard wing spar
- Case 4: Maximum drag
- Case 5: Gust loads for nacelle attachment

- Strain limits per cases above exceeded on a couple of occasions, yet most of the test was ran at negative AOA

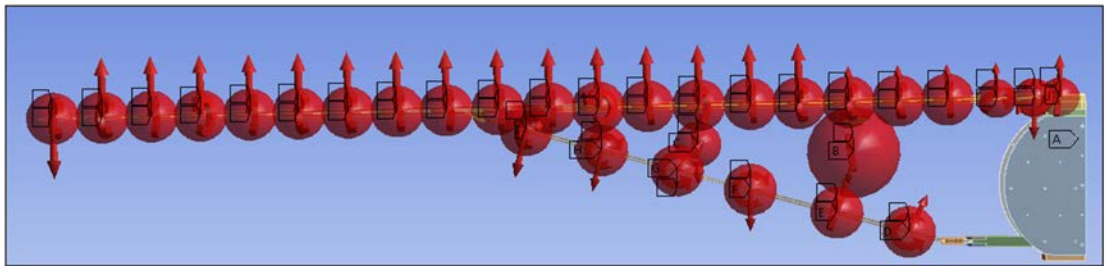

Figure 3.6 – Critical Load Cases

4.0 Dynamic Aeroelastic State Space Model

The current process takes the analysis modes and unsteady doublet lattice aerodynamics and generates a dynamic aeroelastic state space model which is used to develop control laws. Unsteady aerodynamics is represented by a P-transform method in the time domain requiring no additional aero states. Multiple models were generated as the analysis FEM matured. Final models were based on FEM19 which was used to generate the tested control laws. Models included 40 states for 20 flexible modes up to 100 Hz. Models contain outputs at all accelerometer locations consisting of displacement, rate, and acceleration in all three coordinate directions and rotational displacement and rate about all three coordinate directions. Models contain inputs consisting of the inboard and outboard wing trailing edge control surface deflection, rate, and acceleration to accommodate coupling actuator dynamics. Final FEM19 models include 13 dynamic pressures at Mach =0.75 and two dynamic pressures at Mach = 0.6, 0.65, and 0.7 .

5.0 Control Law Design

5.1 Overview

Two separate control law designs were developed and tested in the closed-loop testing at the TDT. The first design was developed for a pair of System Identification (SysID) models of the TBW model. The SysID models were derived from control surface sweeps performed in open-loop testing. The second control law was designed for the FEM19 State Space Model (SSM) dynamics. Both control law designs were based on Linear Quadratic Regulator (LQR) design techniques with a Kalman Filter state estimator. Both "designs" are actually comprised of several point designs (2 SysID models and 18 SSMs) and employ a "nearest neighbor" algorithm based on Mach and dynamic pressure (Q) to perform "gain scheduling". Figure 5.1 shows where the various models (SysID and SSMs) were defined in relation to the pre-holiday flutter boundaries. Both designs proved to be robust to variations in Mach, Q, and angle of attack (AOA).

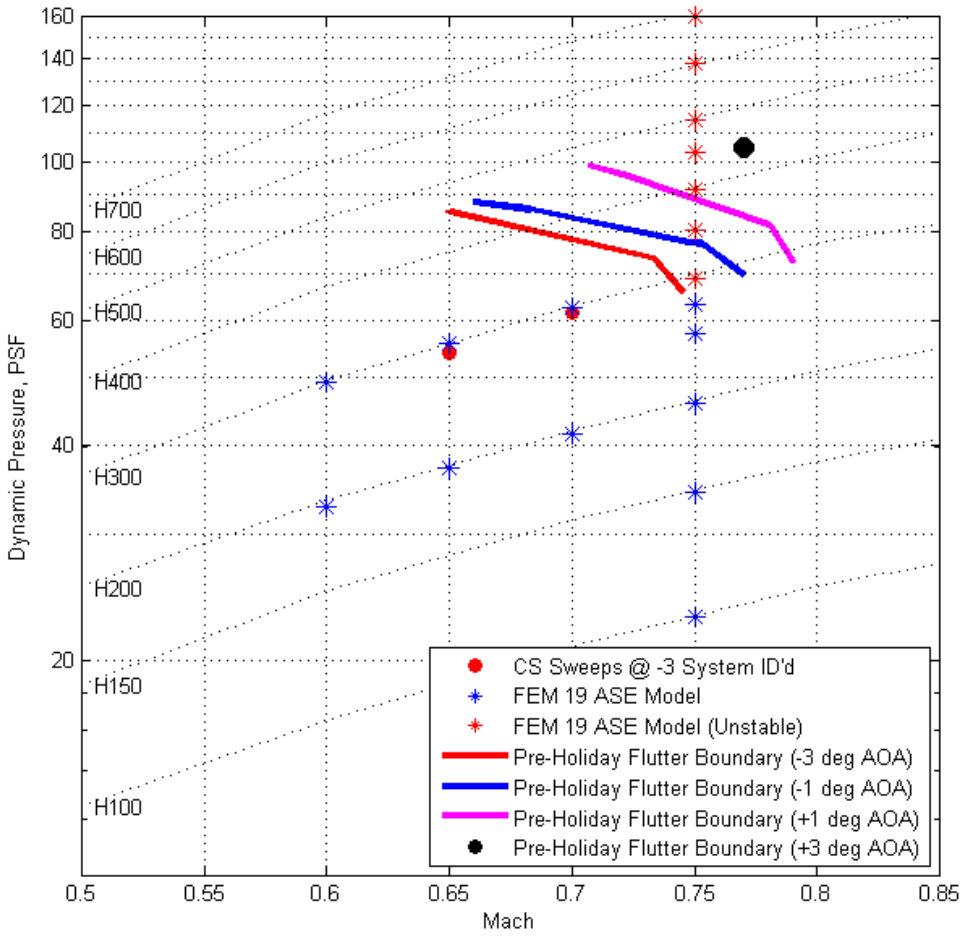

Figure 5.1 – Model Definition Points

5.2 System Identification Model Development

The SysID methods employed to derive the two models were based on methods developed previously for the Aerodynamic Efficiency Improvement program. The SysID method uses an optimizer to tune the simulation model to match the test data collected in the control surface sweeps. The derived models were based on open-loop control surface sweeps at Mach 0.65, Q 53.9 psf (TDT Run 10, Tab Points 529 and 530) and Mach 0.7, Q 61.6 psf (Run 10, Tab Points 551 and 552). All of the sweeps were performed at an AOA of -3°. The FEM19 SSMs were used as a starting point in the process. The up side to the SysID modeling is that if the process converges to a solution, you have a high degree of confidence in the model. The down sides to this approach to model generation are the necessity for open-loop control surface sweeps and the large amount of memory and processor capacity required. Each of these models took over a day to generate, even given the fairly accurate starting point. The original plan for the TDT tests was to forgo the SysID step in order to save time and just use the FEM models for designing the

controller. The variation in the TBW model's GVT data from pre-holiday to post-holiday provided both more time to develop the SysID models and the desire to make sure more wind tunnel time wasn't lost tuning the controller once testing began.

A comparison of the SysID model's mode frequencies and damping is shown in Table 5.1. Figure 5.2 shows a comparison of the Mach 0.65 SysID model to its FEM19 SSM counterpart at for the inboard control surface to the outboard wing tip (forward) accelerometer (Z axis). In general, the SysID and FEM19 models agree fairly well, but the FEM19 models tend to be more attenuated in the 5 to 10 Hz range.

Table 5.1 – SysID to FEM19 Model Comparison - Frequency & Damping

Mach 0.65				Mach 0.70			
SysID Freq (Hz)	FEM19 Freq (Hz)	SysID Damping	FEM19 Damping	SysID Freq (Hz)	FEM19 Freq (Hz)	SysID Damping	FEM19 Damping
5.67	6.03	0.0082	0.0081	5.70	6.03	0.0063	0.0066
6.24	6.02	0.0724	0.0773	6.35	6.14	0.0717	0.0806
9.78	9.98	0.0189	0.0207	9.99	10.20	0.0122	0.0106
11.03	10.91	0.0219	0.0277	10.93	10.78	0.0392	0.0397
19.56	18.74	0.0252	0.0205	19.59	18.78	0.0238	0.0214
25.79	25.67	0.0682	0.0105	26.73	25.63	0.0124	0.0119
28.04	27.77	0.0010	0.0117	28.22	27.78	0.0011	0.0121
28.33	28.37	0.0102	0.0267	28.60	28.39	0.0227	0.0286
29.36	28.87	0.0023	0.0122	29.38	28.84	0.0017	0.0134
38.62	38.62	0.0090	0.0090	38.64	38.64	0.0092	0.0092
40.21	40.21	0.0231	0.0231	40.21	40.21	0.0257	0.0257
46.92	46.92	0.0106	0.0106	46.94	46.94	0.0109	0.0109
48.09	48.09	0.0231	0.0231	48.05	48.05	0.0263	0.0263
61.52	61.52	0.0064	0.0064	61.52	61.52	0.0066	0.0066
68.32	68.32	0.0082	0.0082	68.32	68.32	0.0085	0.0085
76.34	76.34	0.0088	0.0088	76.35	76.35	0.0094	0.0094
82.76	82.76	0.0158	0.0158	82.80	82.80	0.0174	0.0174
87.47	87.47	0.0083	0.0083	87.48	87.48	0.0086	0.0086
93.16	93.16	0.0068	0.0068	93.16	93.16	0.0071	0.0071
95.11	95.11	0.0079	0.0079	95.12	95.12	0.0082	0.0082

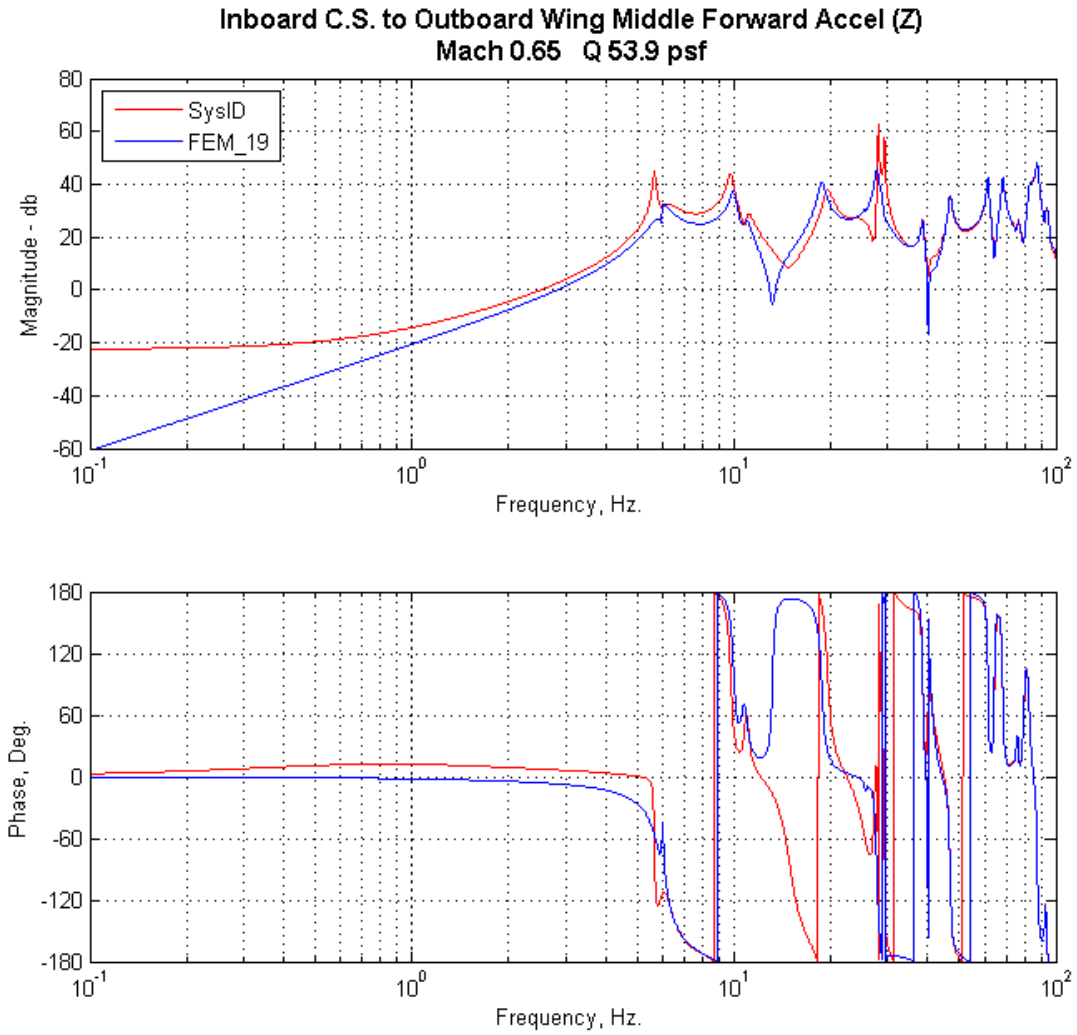

Figure 5.2 – Bode Plot Comparison of SysID Model to FEM19 SSM

5.3 SysID Simulation

The SysID version of the Simulink simulation is shown in Figure 5.3. From the beginning, the simulation architecture was designed so that inserting the controller in the TDT's dSpace control system would be as easy as possible. For the sake of clarity, the controller interfaces depicted in the figures have been simplified to just their core components. The actuator block (shown in orange) contains the model of the actuators. The outputs of the actuator are the inputs to the plant (control surface positions, velocities, and accelerations) and the sensed position of the control surfaces (the RVDT signals). The actuator model is followed by the plant (in state space form), the outputs of which (Y) are the accelerometer readings. The primary inputs to the SysID controller are the accelerometer readings (filtered through the dSpace system) and the RVDT signals. The current tunnel Mach and Q are input for nearest neighbor gain scheduling.

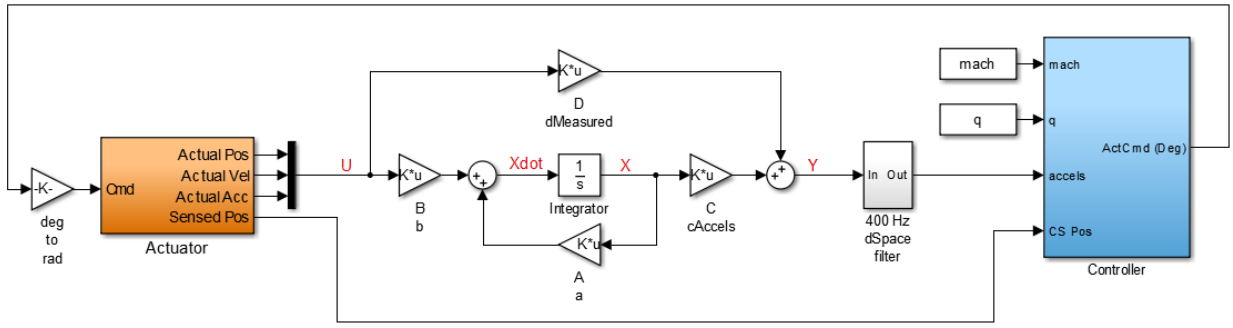

Figure 5.3 – SysID Simulation

5.4 SysID Control Law Design

Figure 5.4 shows the controller design for the SysID system, again slightly simplified. A nearest neighbor algorithm is used to determine which set of gains / state space model to use this pass through the controller. There is some hysteresis built into the algorithm to prevent bouncing between the point designs when the tunnel is near a boundary condition. All of the gains, etc., are predetermined to minimize computational overhead and make the controller block as fast as possible. Tests showed the controller needed to be run at 500 Hz minimum, but the dSpace system was able to run at 1000 Hz for the tests.

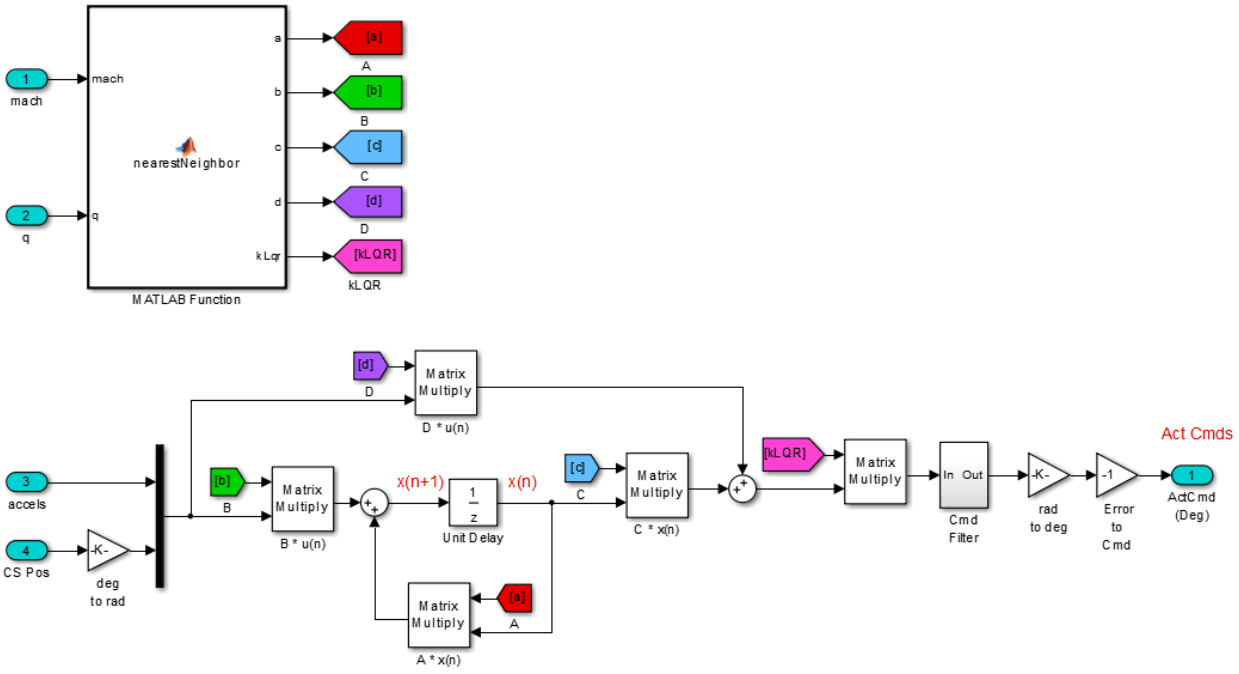

Figure 5.4 – SysID Controller

The sensed control surface positions and filtered accelerometer outputs are combined and fed through a Kalman filter state space estimator to calculate the estimator outputs $(\hat{X})$. The

resulting outputs from the estimator ($\hat{X}$) are multiplied by the LQR gains. A "Cmd Filter" is then applied to obtain the two control surface commands for output to the actuators.

The estimator coefficients are derived by first designing the full order estimator gains. The gains are then applied to the SysID model to form a state space model. The state space model is reduced to 10 states ("balanced" reduction) and discretized at the dSpace frequency, 1000 Hz, with "tustin" pre-warping.

The LQR gains are derived using a full order LQR design process primarily weighting the first 5 modes (10 states) with heaviest weighting on the 10 and 20 Hz modes.

The "Cmd filter" is second order, 15 Hz, 0.65 damping, "tustin" pre-warping, that has been discretized to 1000 Hz.

The weightings for the LQR gains were tuned to achieve our primary goal of actively damping the 10 Hz flutter mode while maintaining good stability margins. Figures 5.5 and 5.6 show the resulting Bode plots for both the inboard and outboard control surfaces at the Mach 0.65 condition. The plots show the 10 Hz mode has been attenuated approximately 9 db in the inboard loop and approximately 15 db in the outboard loop. In Figure 5.7, the Nichols plots for both of the control surface loops, shows the robust margins of 9 db gain and 45° phase (depicted as black diamond shapes in the plot) have been maintained. Figures 5.8, 5.9, and 5.10 show similar plots for the Mach 0.7 condition. This condition is closer to the flutter condition and as such was harder to control resulting in slightly lower, but still acceptable, margins. The final designs were simulated in the time domain and proved to be stable.

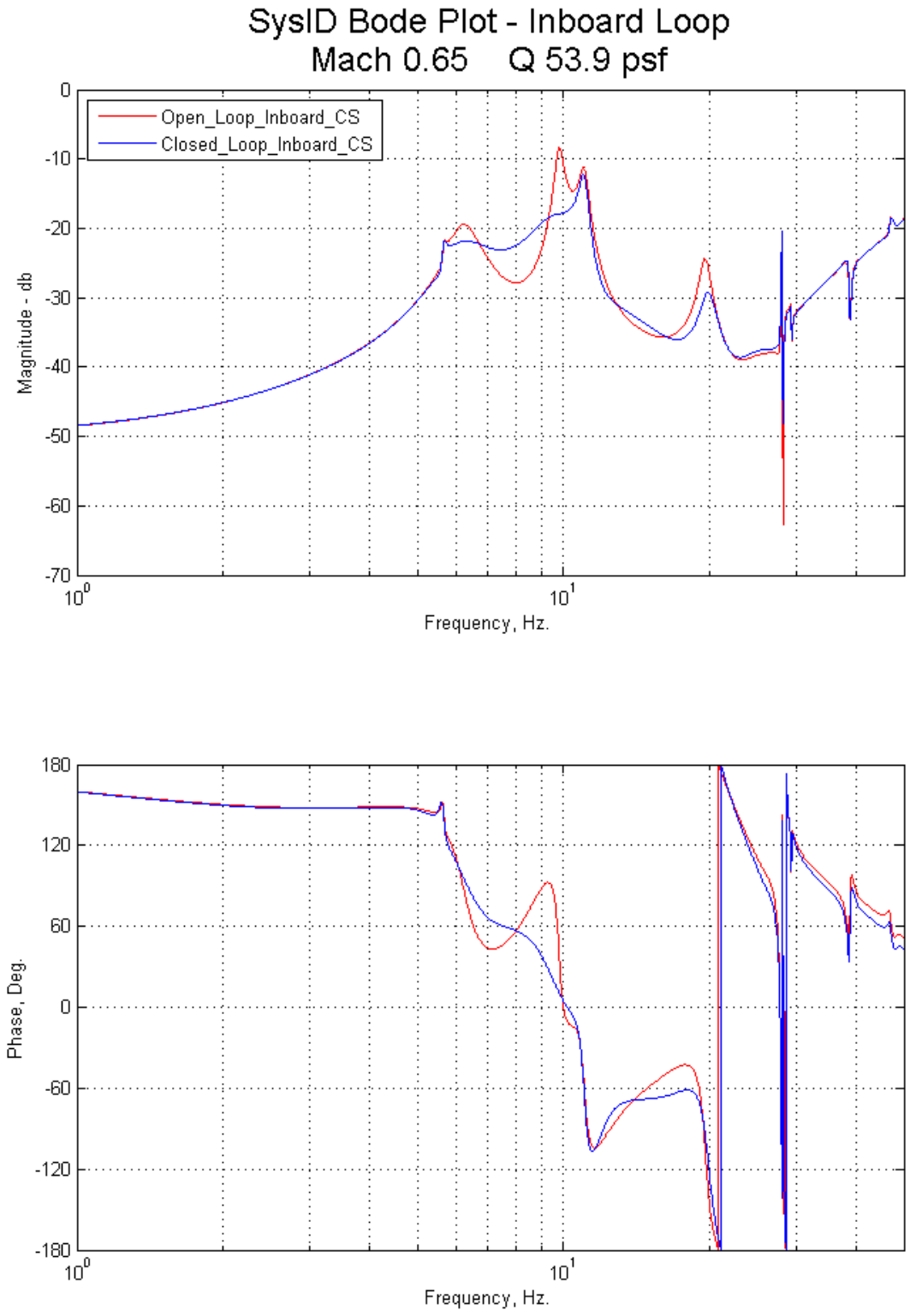

Figure 5.5 – Inboard Control Surface Open-Loop/Closed-Loop Bode Plot Comparison (Mach 0.65)

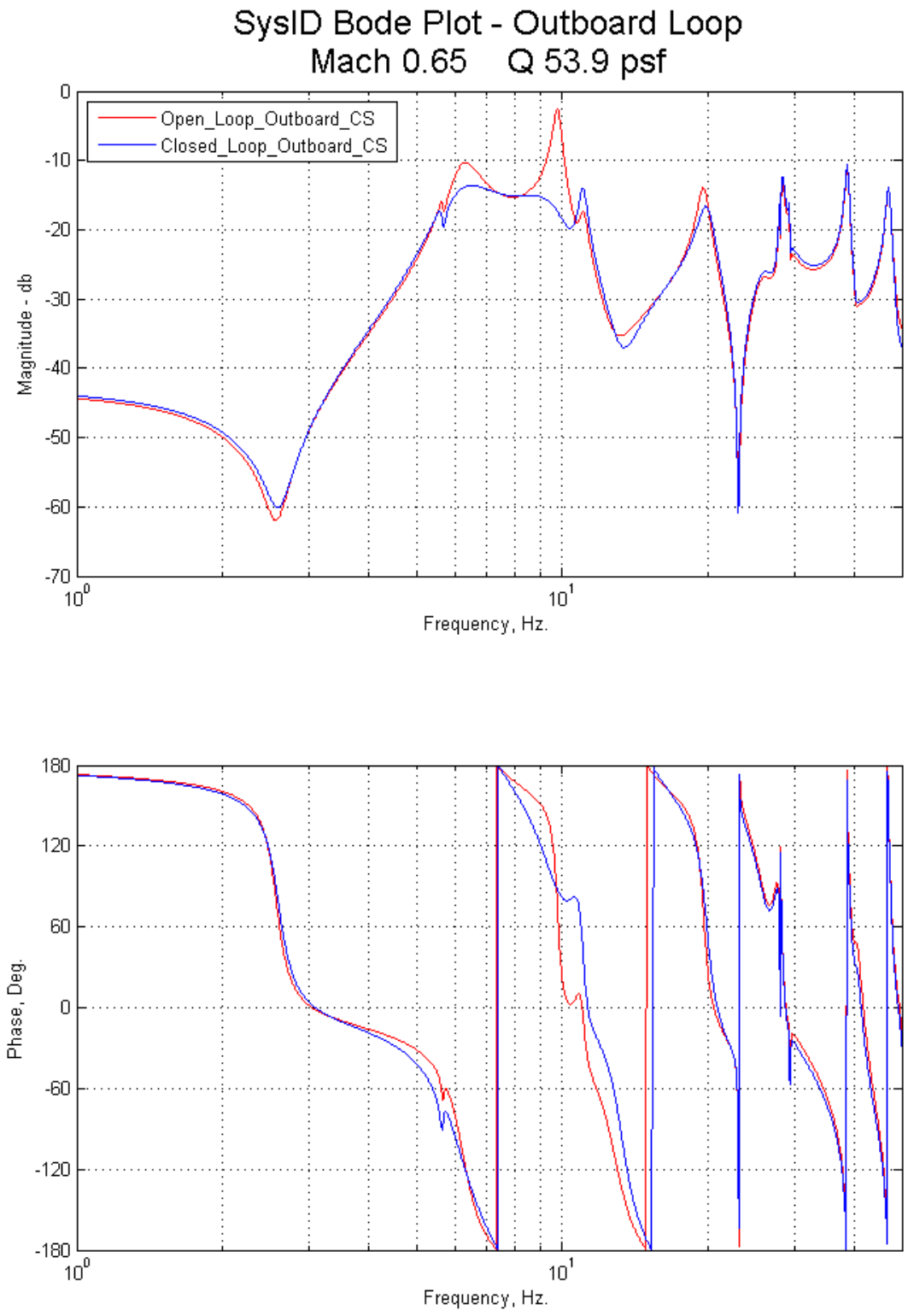

Figure 5.6 – Outboard Control Surface Open-Loop/Closed-Loop Bode Plot Comparison (Mach 0.65)

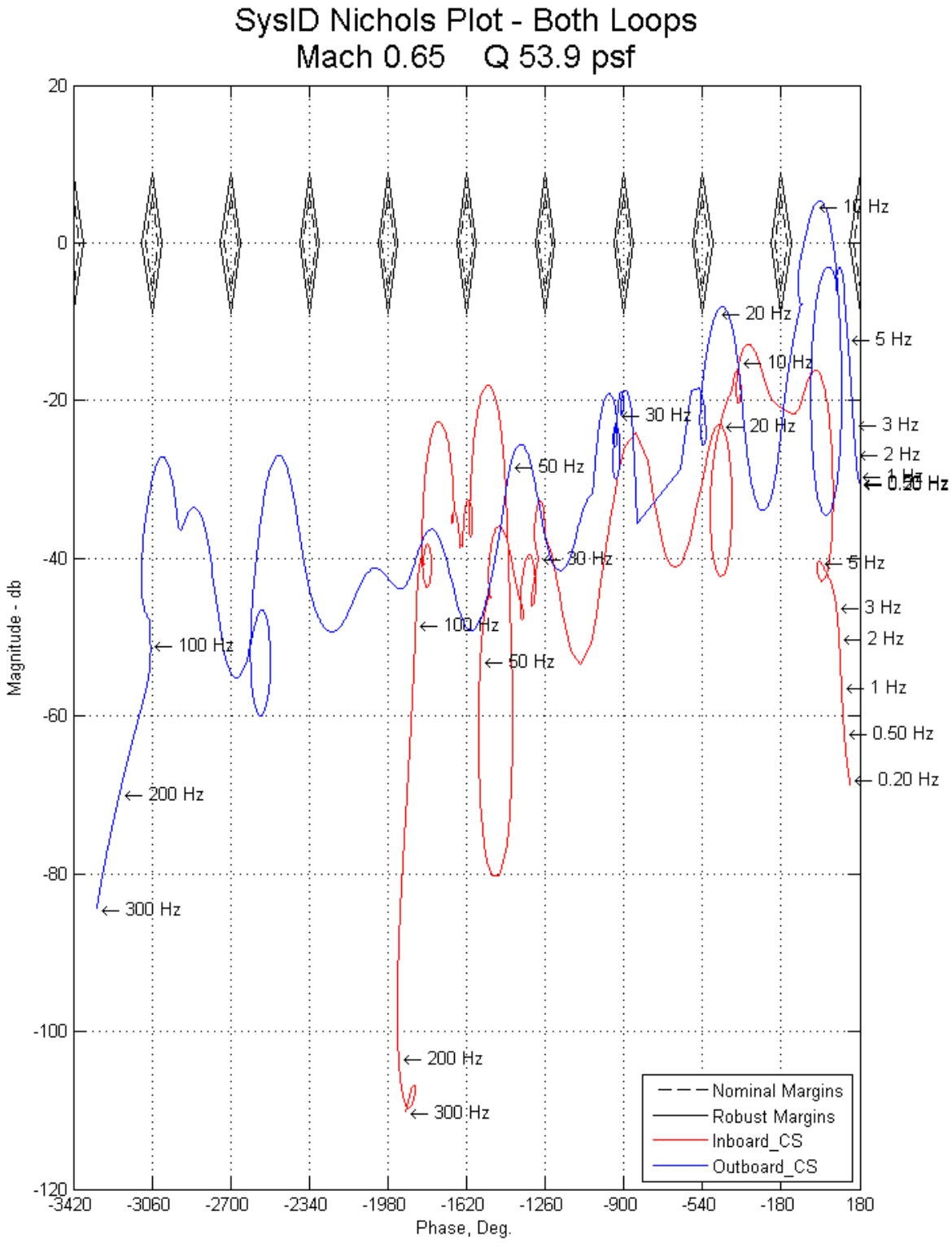

Figure 5.7 – SysID Mach 0.65 Nichols Plot

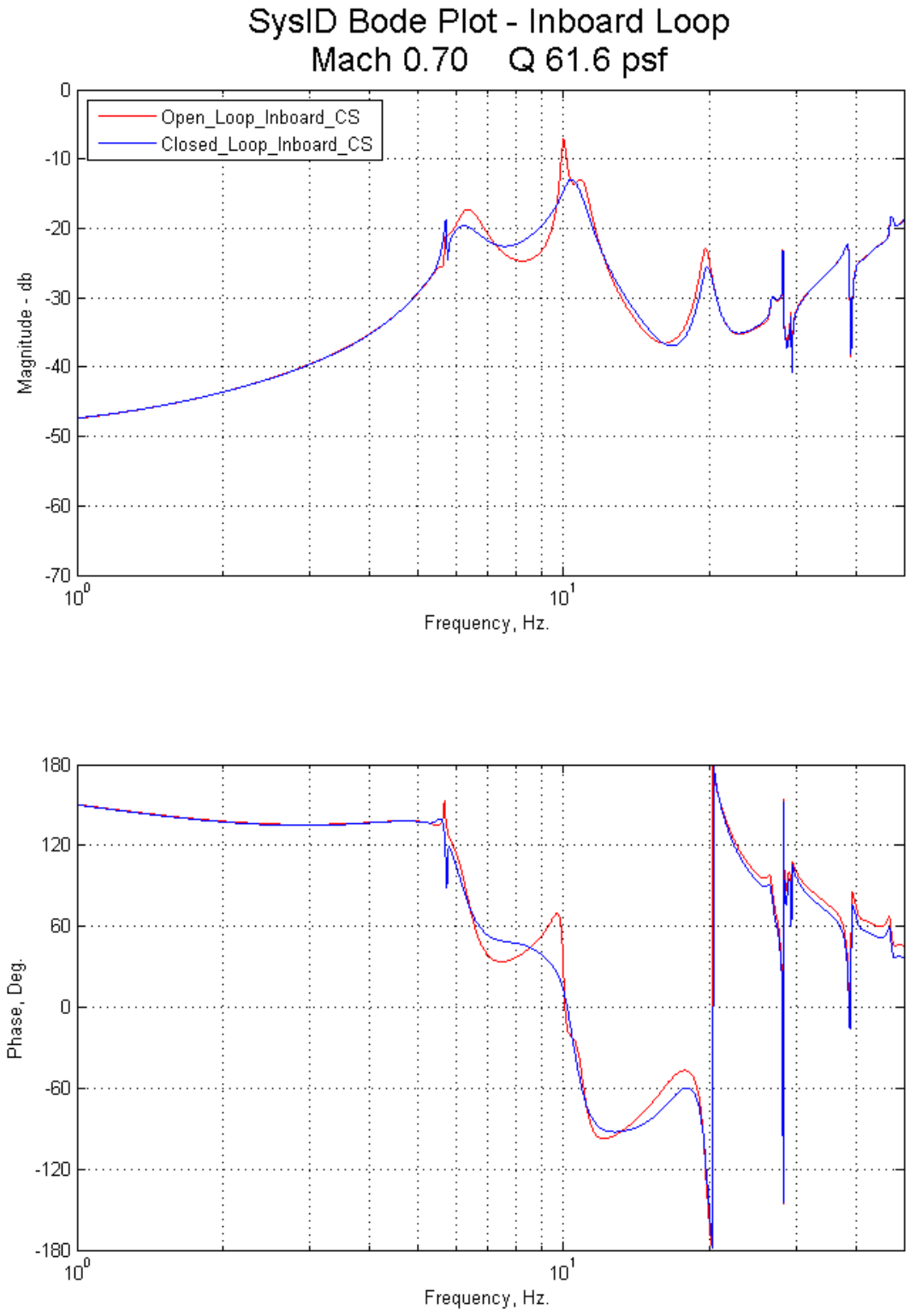

Figure 5.8 – SysID Inboard Control Surface Open-Loop/Closed-Loop Bode Plot Comparison (Mach 0.7)

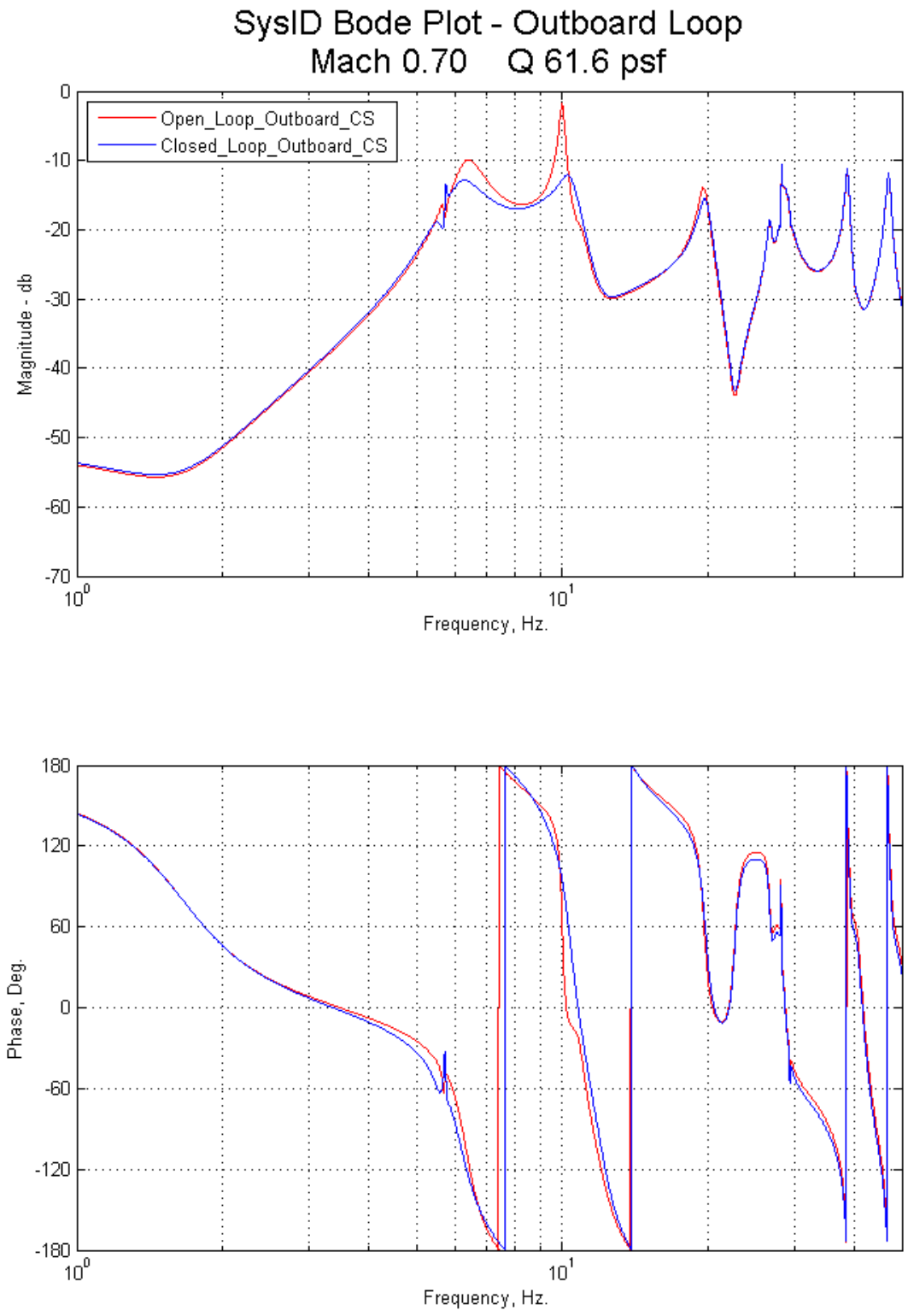

Figure 5.9 – SysID Outboard Control Surface Open-Loop/Closed-Loop Bode Plot Comparison (Mach 0.7)

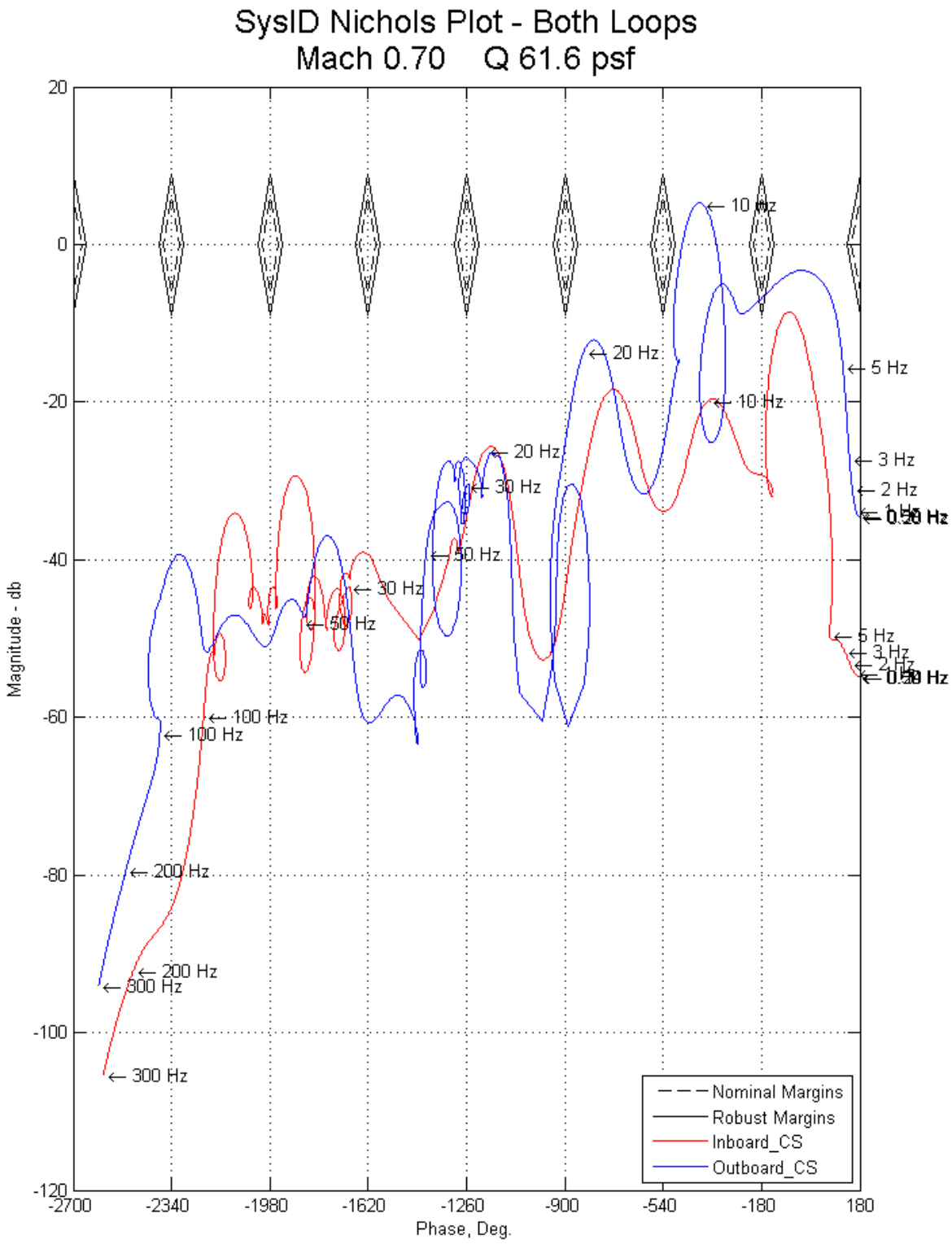

Figure 5.10 – SysID Mach 0.7 Nichols Plot

5.5 SysID Wind Tunnel Testing

Code was inserted in the controller to gather data that could be used to validate the stability margins derived from the simulation against actual test data. Unfortunately, the data gathered was too noisy to quantifiably validate the simulation. Figure 5.11 shows one of the better plots of this data. The plot compares the stability margins derived from one of the early TDT runs (Run 48, Tab Point 2354, Mach 0.7, Q 61.2 psf) to the expected simulation results.

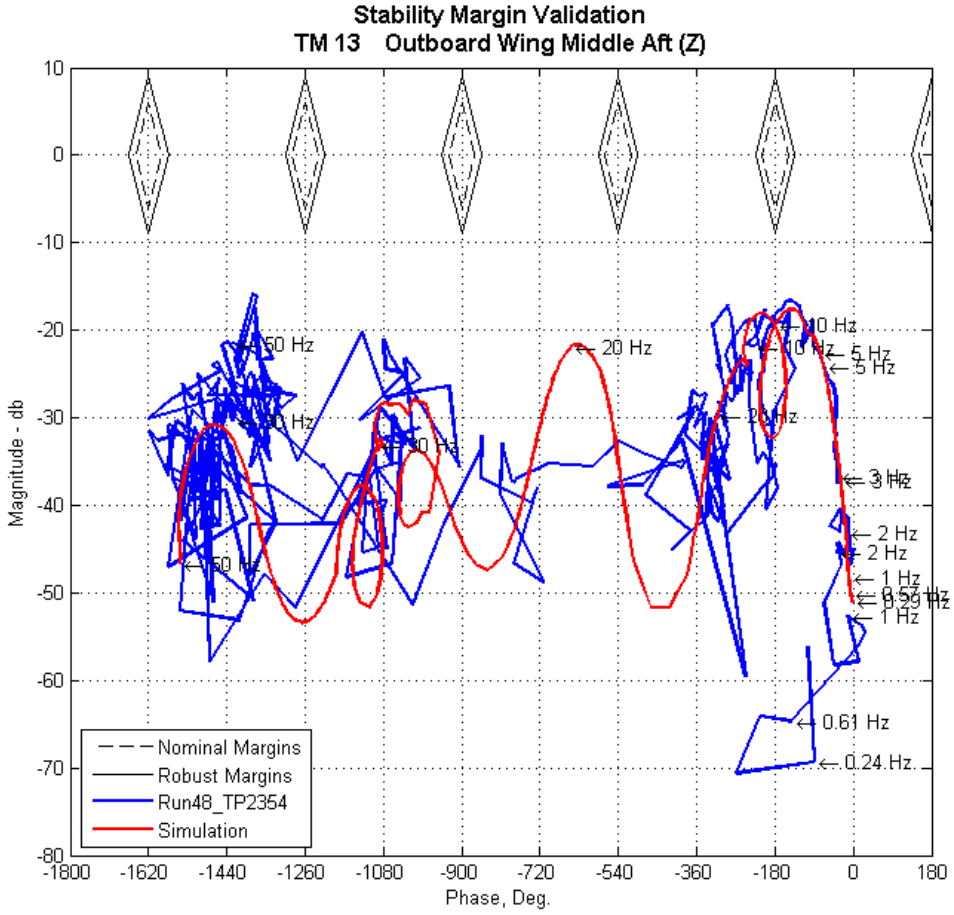

Figure 5.11 – Sample Tunnel Data Stability Margin Comparison

An example of the controller actually controlling flutter is shown in Figure 5.12. The TDT operators have the ability to turn the controller on and off in real time and the plot shows one of these occasions where the TBW is in a flutter condition. The data in red shows the wing beginning to flutter, while the data in blue shows flutter being controlled. The SysID controller supported TDT runs 48 through 54 where Mach varied from 0.23 up to 0.81, Q varied between 10 and 97 psf, and AOA varied from -3° to 1°. Almost all of testing with the SysID controller was based on the one design point at Mach 0.65, Q 53.9 psf, and entailed no gain scheduling. In all these cases where the controller was engaged, flutter was controlled.

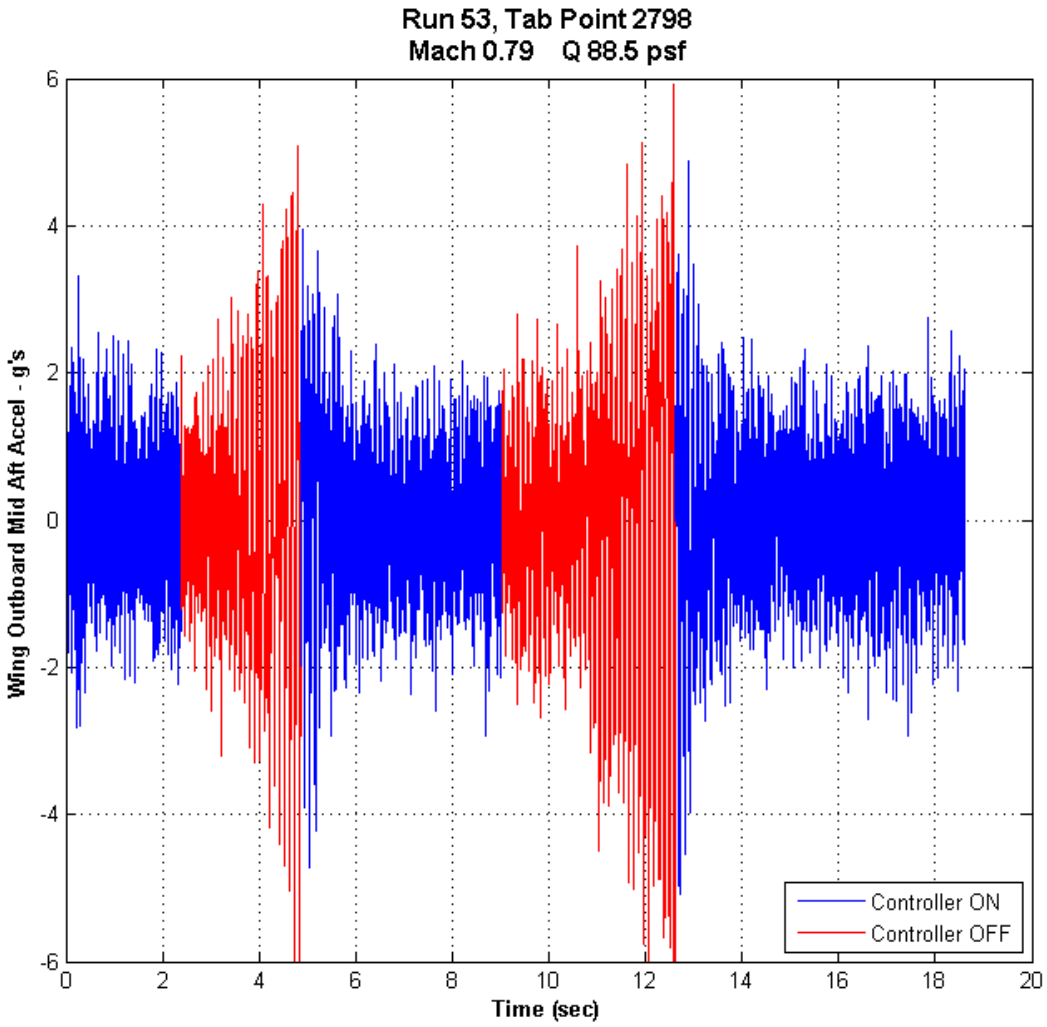

Figure 5.12 – SysID Controller – Open-loop/Closed-loop Demonstration

5.6 FEM19 Simulation and Control Law Design

Since a functioning controller was in place, there was time to attempt to design a new controller based on the FEM19 SSMs. Based on experience with the SysID gain design process, some changes were incorporated for the FEM19 controller. The FEM19 simulation architecture is essentially the same as the SysID version. The main difference is that the actuator commands are fed back within the controller, so the RVDT outputs are no longer required to be input to the controller. Figure 5.13 shows the FEM19 simulation.

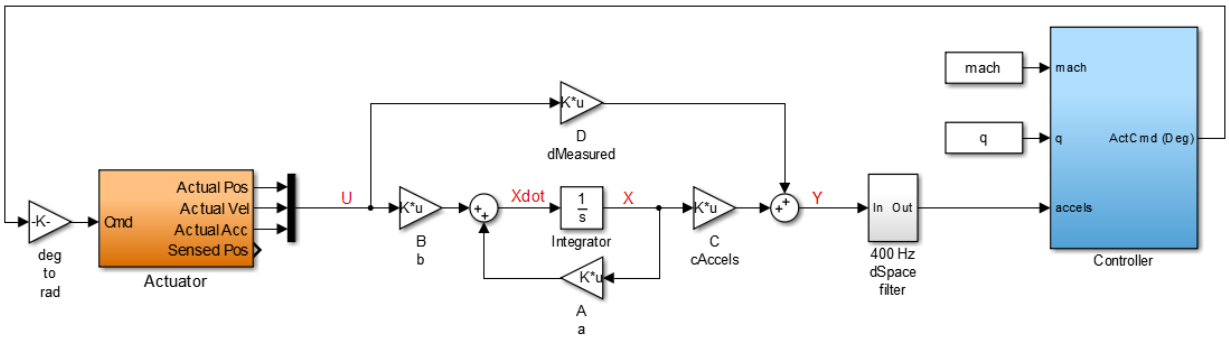

Figure 5.13 – FEM19 Simulation

The FEM19 controller architecture (Figure 5.14) is "essentially" the same as the SysID controller. The major difference is the actuator commands are fed back instead of using the RVDT signals. The other obvious change is the lack of LQR gains in the diagram. The gains are there, they've just been embedded in the estimator's realization prior to calculating the estimator coefficients. Also, a 15° limit is imposed on the actuator commands and the hysteresis in the nearest neighbor algorithm was modified such that the states and actuator commands could be zeroed out briefly when transitioning between design points. The "Cmd filter" frequency was increased to 40 Hz (second order, 40 Hz, 0.65 damping, "tustin" pre-warping, that has been discretized to 1000 Hz).

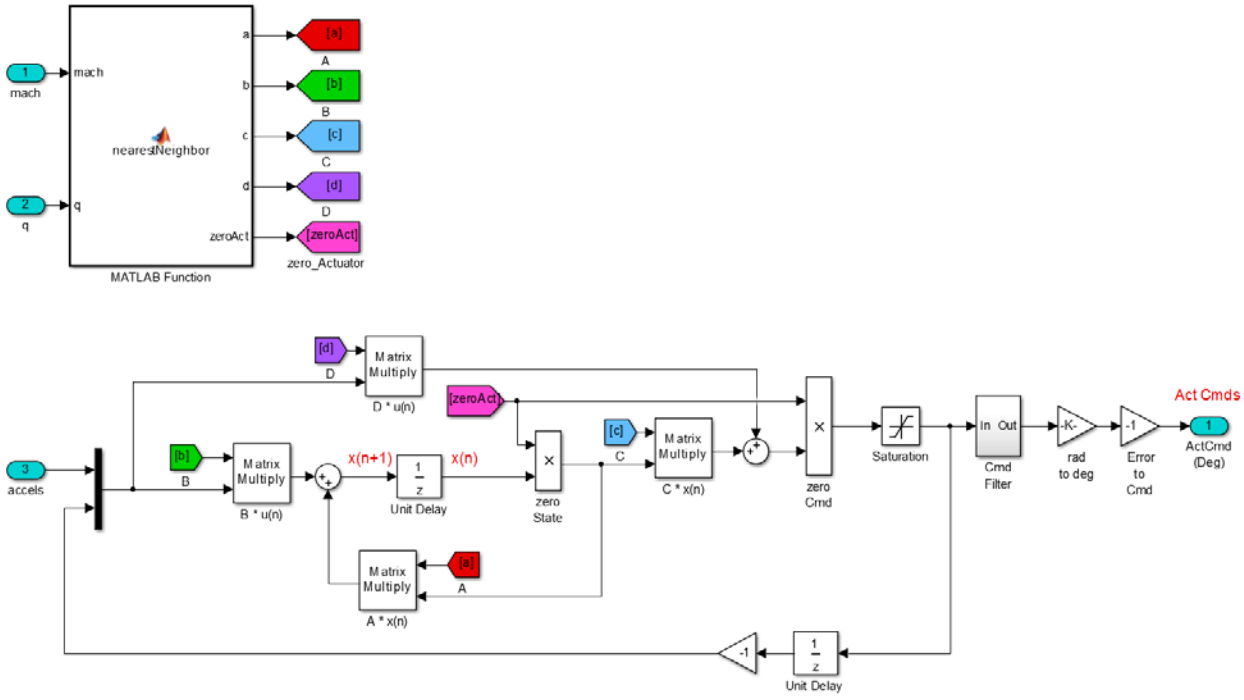

Figure 5.14 – FEM19 Controller

The process for deriving the LQR and estimator gains is fundamentally different from the SysID version. In order to increase stability margins, the FEM19 SSM was augmented with a pair of second order filters (40 Hz, 0.98 damping) to model the two actuator's states and allow the LQR process to put gains on them. In order to keep the LQR gains on the actuator's states in check, the system was augmented with a pair of third order filters effectively penalizing very high gains to prevent driving the actuator bandwidth too high because of its inherent non-linearities. The third order filter is a second order filter (10 Hz, 0.6 damping) over a second order filter (100 Hz, 0.7 damping) multiplied by a first order filter (101 Hz). The LQR gains are derived using a full order LQR design process on the augmented model primarily weighting the first 5 modes with heaviest weighting on the 10 Hz flutter mode. It was found that heavily weighting the third state of the third order filter kept the actuator gains within the desired range.

The estimator gains are calculated and the LQR gains are embedded into estimator to form a new state space model. This model is reduced (balanced reduction) to 20 states (10 modes) and discretized at 1000 Hz.

The weightings for the LQR gains were tuned to actively damp the 10 Hz flutter mode while maintaining good stability margins. Figures 5.15, 5.16, and 5.17 show the resulting Bode and Nichols plots at the Mach 0.7 condition. The plots show that the 10 Hz mode has been attenuated about 7 db in the inboard loop and about 6 db in the outboard loop, but the robust margins (9 db and 45°) were maintained. In fact, the robust margins were maintained for all but the two most unstable cases (Mach 0.75, Q 137.7 psf and Mach 0.75, Q 160.6 psf) and the nominal margins (6 db and 30°) were maintained in those cases.

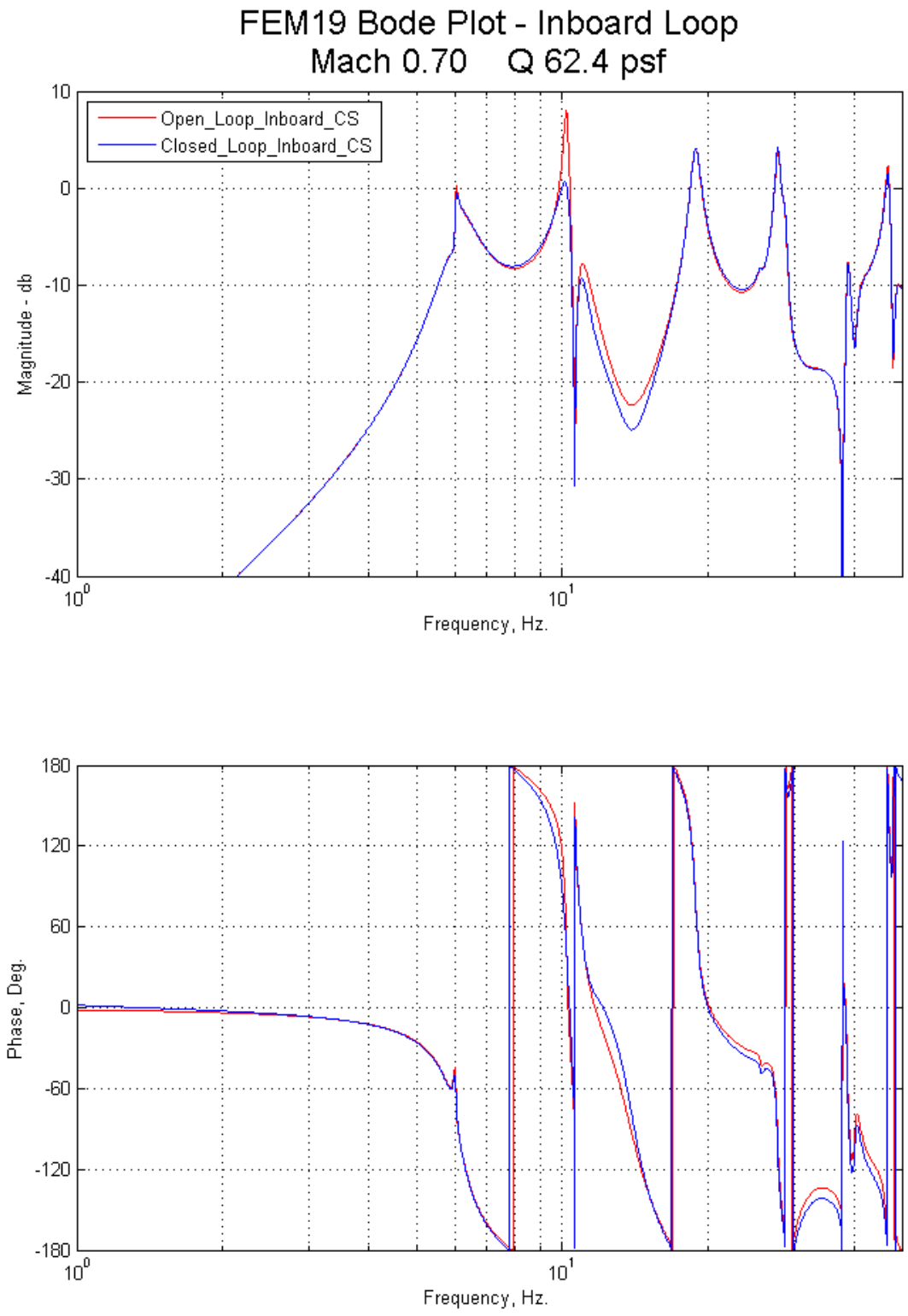

Figure 5.15 – FEM19 Inboard Control Surface Open-Loop/Closed-Loop Bode Plot Comparison (Mach 0.7)

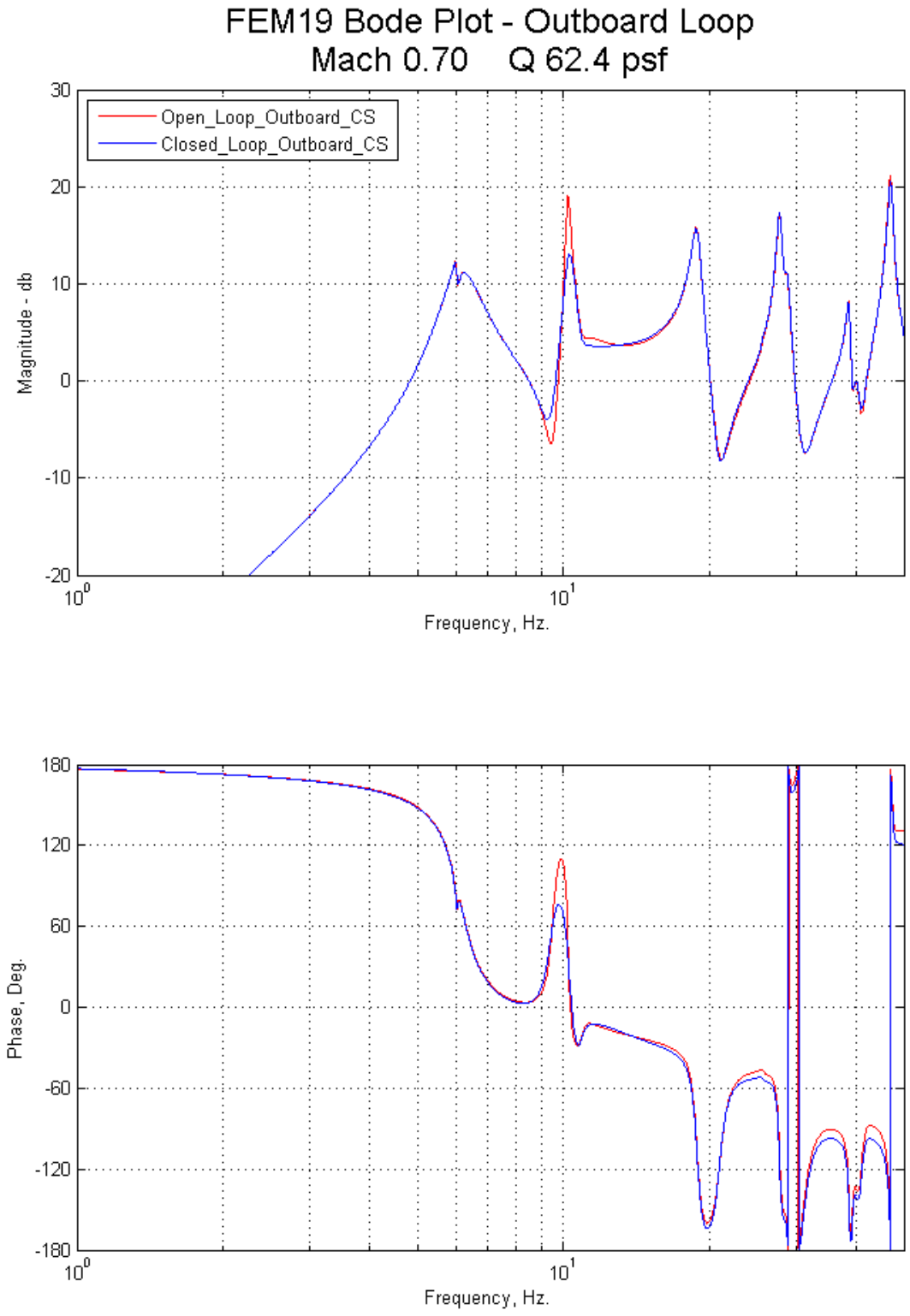

Figure 5.16 – FEM19 Outboard Control Surface Open-Loop/Closed-Loop Bode Plot Comparison (Mach 0.7)

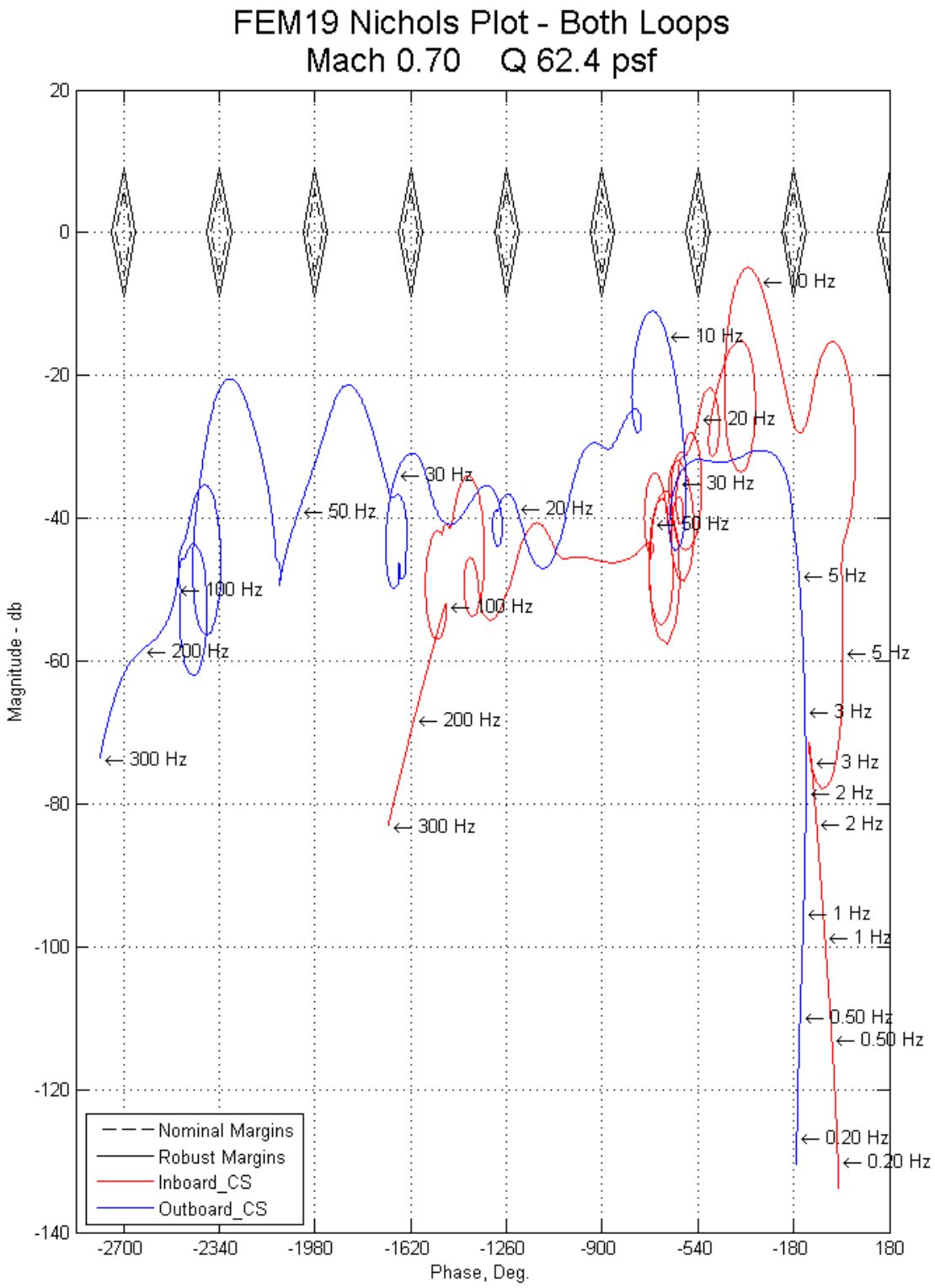

Figure 5.17 – FEM19 Mach 0.7 Nichols Plot

The final designs were tested in the time domain. Figure 5.18 shows a comparison of the simulated time responses, with the control loops open and closed, for one of the unstable cases (Mach 0.75, Q 68.9 psf). As expected, the open loop accelerations grow unbounded.

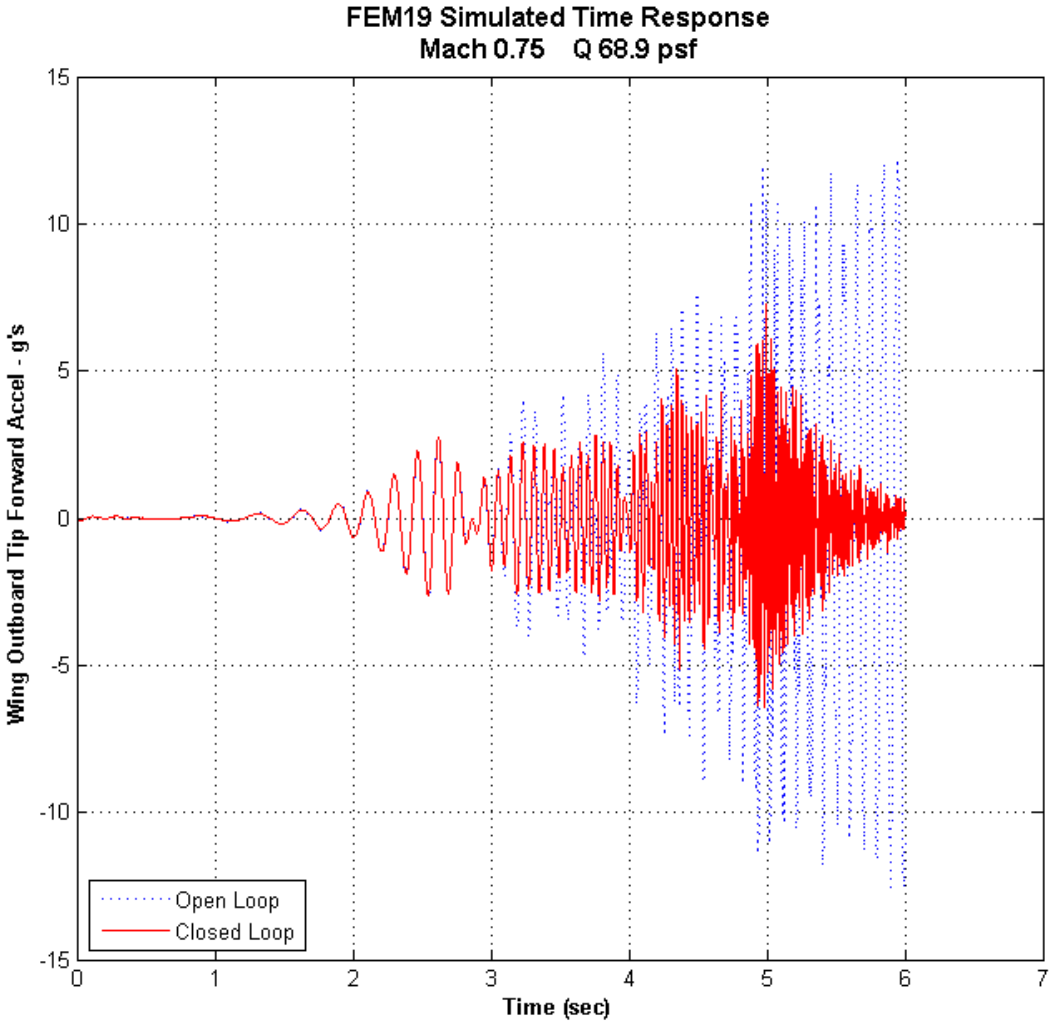

Figure 5.18 – FEM19 Simulated Time Response

5.7 FEM19 Wind Tunnel Testing

Figure 5.19 shows an example of the controller controlling flutter at an unstable condition. Again, the data in red shows the wing beginning to flutter when the controller is turned off and the data in blue shows controller damping out the flutter. The FEM19 controller supported TDT runs 55 through 63 where Mach varied from 0.35 up to 0.83, Q varied between 21 and 115 psf, and AOA varied from -3° to 5°.

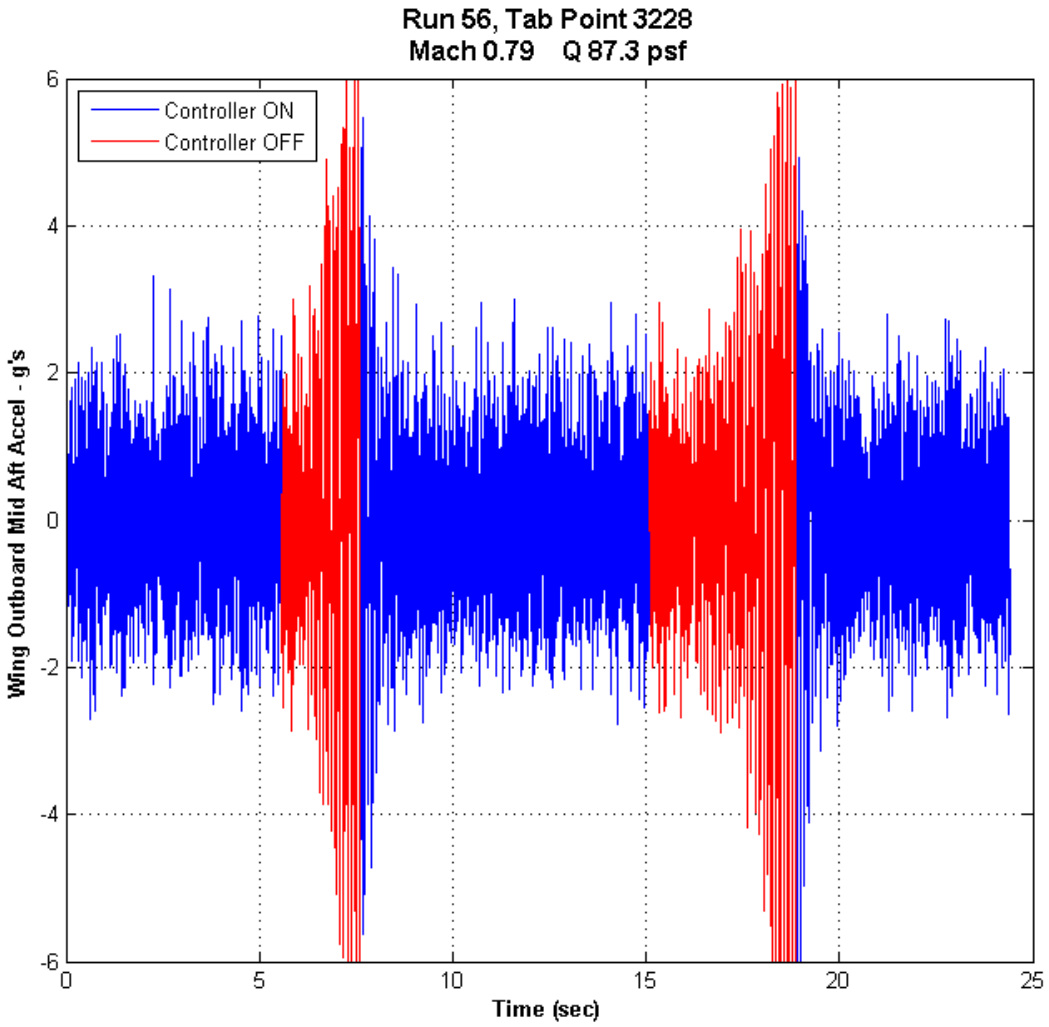

Figure 5.19 – Fem19 Controller – Open-loop/Closed-loop Demonstration

5.8 System Identification Model Development – Version 2

With two functioning controllers in hand, a decision was made to try and develop a controller based on control surface sweeps at an unstable point. In order to do this, of course, a controller would have to be functioning at the time to keep flutter attenuated. Data was acquired, but several issues prevented the models from converging to a solution. Large amplitude, high frequency sweeps were required to overcome the inherent noise in the system. However, the combination of amplitudes and frequencies required were too high for the actuators which became flow rate limited. Also, some unexpected non-linearities became apparent in the data that could not be accounted for in the SysID process. Between the actuator limitations, the inherent noise in the system, and the non-linearities, the SysID process failed to converge on a solution.

5.9 Conclusions

The main conclusion that can be drawn from this control law effort is that the LQR design process worked very well in this instance, allowing the 10 Hz flutter mode to be targeted directly in the gain design process. The cycle time for iterations was reduced and the ability to switch from the SysID models over to the FEM models was very smooth. The FEM19 SSMs based on the pre-holiday model proved to be sufficient for designing a robust control system, potentially reducing the need for open-loop testing in the future. Flutter suppression was demonstrated with two different control systems that proved to be very robust over a wide range of Mach, Q, and AOA.

6.0 Test Procedures

Test points investigated include flutter points, control surface sweeps, gust vane oscillation points, and control surface dwells.

Flutter points involve slowly increasing Mach and dynamic pressure along constant pressure H lines while visually monitoring model vibration as well as PSDs and time histories for signs of instability. Any sign of instability and a bypass valve button is pushed and the tunnel winds down. An example of an unstable open loop flutter point is shown in Figure 6.1. The plot is a time history of the nacelle pylon accelerometer. The flutter points were run both open and closed looped. Once the control laws allowed the Mach and dynamic pressure to increase past the open loop flutter boundary a technique was used to open the loop and quickly close the loop and see if the open loop system looked stable. This technique allowed for determining the back side of the Mach dip open loop flutter boundary.

Control surface sweeps involve running a fixed amplitude sweep from 0 to 30 Hz to generate the data required for the system ID control laws. The sweeps were run inboard alone, outboard alone, and both inboard and outboard. The sweeps were run both open looped and closed loop. The response due to the control sweeps for the closed loop point in the open loop unstable region was lost in the overall noise and insufficient for system ID.

The gust vanes were oscillated both open and closed loop to investigate the control laws effect on gust loads.

Control surface dwells involve oscillating the control surface at the 10 Hz flutter frequency and then stopping the oscillation and recording the response. This technique allows for a good estimate of system damping in the open loop stable region.

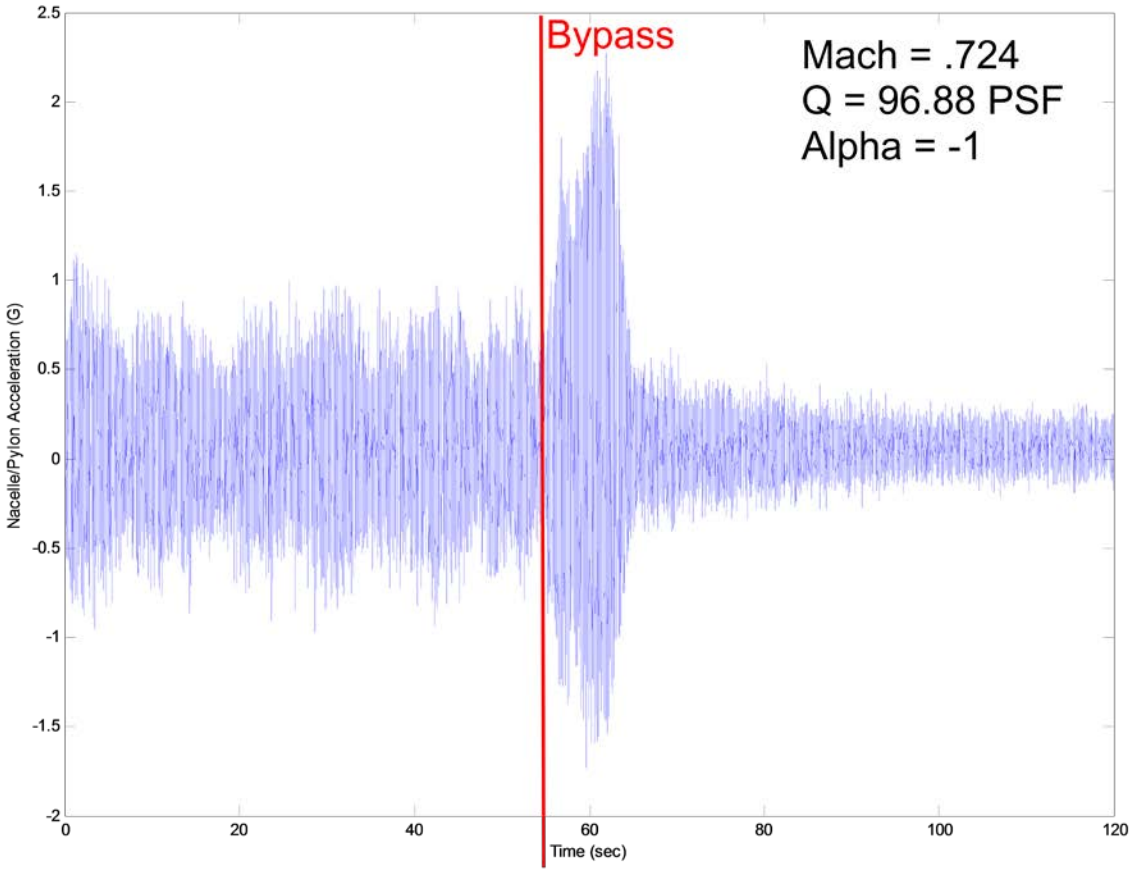

Figure 6.1 – Unstable Open Loop Flutter Point

7.0 Test Results

Testing was broken up into pre-holiday open loop testing and post-holiday closed loop testing.

7.1 GVT and FEM Correlation

GVTs were run to correlate our analysis model to the test frequencies and mode shapes. The final preholiday in tunnel GVT results were compared to the pretest FEM18 analysis model results. A comparison of the analysis and test frequencies and modal assurance criteria(MAC) is shown in Figure 7.1. The two primary flutter modes are second bending mode 3 and first torsion mode 4. The GVT vs. FEM18 frequencies are significantly different and the mode 3 MAC was .9. FEM19 was created to better match the preholiday GVT result. This was mostly accomplished by removing the electronic turn table model we had attached to the FEM. In addition, small changes to the wing stiffness were required. A comparison of preholiday GVT and FEM 19 is shown in Figure 7.2. This shows a very good comparison between test and analysis. After the preholiday testing a cutout was made in a fairing at the root of the strut. It was suspected that there wasn't enough clearance between the strut root joint and the fairing and some fouling was occurring. This was tested by looking at GVT results with and without a wedge added which contacted the fairing. The cut out and wedge are shown in Figure 7.3. A summary of GVT frequencies showing which GVTs the FEMS are based on is shown in Table 7.1. The table shows significant difference in Mode 3 frequencies pre and post holidays. Part of the difference is due to the post holiday cutout in the strut root fairing. The GVT results with the wedge included don't get all the way back to the pre holiday values. A FEM20 was created by updating stiffnesses again to match the post holiday GVT results. The post holiday GVT is compared to FEM20 in Figure 7.4. Again, there is good correlation between test and analysis. The resulting FEM20 equivalent beam full scale wing, strut and jury stiffness for scaling are compared to the baseline stiffness in Figure 7.5 and Figure 7.6. Note, the strut stiffness distribution did not change from the baseline; and the jury stiffness distribution was set to a constant value because of the size and ability to manufacture in order to keep within mold-line.

7.2 Doublet Lattice Aerodynamic Correction Factors Update

To improve the test vs. analysis comparisons, the doublet lattice static aerodynamic correction factors, described in Section 2.1.8.5 of the TBW Final Report (Volume I – Truss Braced Wing Design Exploration), were updated to better match all the test mean wing strain gage results. This was done for Machs 0.7, 0.75, and 0.82. Figure 7.7 shows the improved correlation with test results for the outboard root strain gage at Mach = 0.7.

7.3 Pre-Holiday Flutter Points

All the pre-holiday flutter points at alpha -3, -1, +1, and +3, are shown in Figure 7.8 through Figure 7.11. Blue Xs are stable and red Xs are unstable. The pre-holiday unstable points for the

four angles of attack are shown in Figure 7.12. The results show a significant variation with angle of attack. This is in contrast to tradition linear flutter results which don't change for different angles of attack or loads. This angle of attack variation is unique to the truss braced wing due to its large in-plane loads and reduced stiffness of the inboard wing.

7.4 Non-linear Flutter Method

A method to include preload and large displacement effects in the flutter analysis is shown in Figure 7.13. The process starts by generating loads in Nastran solution 144. Next the loads are applied to the model in a Nastran solution 106 nonlinear run including the large displacement parameter. Finally the linear solution 145 is run from a restart of the stiffness and mass matrix output from the 106 run.

7.5 Pre-Holiday Flutter Test vs. Analysis

Pre-holiday flutter comparison between test and analysis is shown in Figure 7.14. The comparison is with the static corrections from Section 7.2 used in the solution 144 analysis, and no corrections to the doublet lattice unsteady aerodynamics for the flutter solution 145 analysis. The black line shows the traditional linear 145 solution. The analysis including the preload and large displacements predicts an angle of attack trend which matches the test data. The analysis also is accurate in predicting the minimum flutter speed at each angle of attack. The Mach trend using the theoretical doublet lattice does not match the test data.

7.6 Post-Holiday Flutter Points

Post-holiday alpha -3, -1, +1, and +3, flutter points are shown in Figure 7.15 through Figure 7.18. At alpha -3 degrees, stable points were found at dynamic pressures above the unstable region. The pre-holiday and post-holiday flutter test results are shown in Figure 7.19. The trends are very similar. The post-holiday flutter speeds have increased as would be expected due to the increase separation between the primary modes post holiday. The post-holiday analysis vs. test is shown in figure Figure 7.20. Again, angle of attack trend and minimum flutter speed modeled well.

7.7 Post-Holiday Stable Flutter Point Root Mean Square

The post-holiday stable flutter points root mean square (RMS) results for the wing tip, nacelle pylon, outboard strut, and wing root accelerometers are shown in Figure 7.21 through Figure 7.24. All plots show a sharp rise in RMS as the flutter boundary is approached except the strut gage. The strut gage peaks at lower Machs than the flutter boundary. The strut gage peaks between M=0.72 to M=0.74. The alpha = -3 results show peak RMS values in the high Q region above the unstable region.

7.8 Post-Holiday Dwell Points Damping Estimates

Dwell time history decays were recorded at some 102 points, varying in Angle Of Attack (AOA), Mach, and/or dynamic pressure. A technique, scripted in Matlab, of fitting a set of damped sine waves to the decay response was employed to access modal damping. On average 3 sine waves were used to best fit the response, with one frequency and corresponding damping capturing a majority of the response.

The basic steps in the process for a given dwell are illustrated using Run Number 44 Tab Point 2007. The raw time history for this Tab Point is plotted in Figure 7.25. Next, the decay portion of the time history to be fit is select and is displayed in Figure 7.26. A Fast Fourier transform (FFT) is performed on the time history to assess the frequency content of the decay which provides a start point for the fit process, the FFT results are shown in Figure 7.27. The 3 sine wave fit for the decay time history is shown in Figure 7.28. The comparison of the 3 sine waves that make up the total fit are shown Figure 7.29. The Matlab GUI with fit results, Run Number 44 Tab Point 2007, is shown in Figure 7.30. The fit frequency values are in Hertz and the damping values are zeta.

A total of 82 dwells were fit and damping values recorded. One accelerometer, Measurand ID "ACCWINP", on the wing nacelle pylon was used for all the dwell data reduction. The data is shown in Table 7.2 through Table 7.5 for the AOA's of -3, -2, -1. 0 +1, +2, and+3. The damping value being reported is structural damping, g, which is two times zeta (from fit process output). A positive damping value means the sine wave response is diverging while a negative value means the response is damping out.

The estimated damping results for all the dwells are plotted in Figure 7.31 through Figure 7.34. The frequency and structural damping"g" values are labeled for each point; positive damping values are highlighted in red. The results show the damping values getting smaller as the flutter boundary is approached. There is also a section of low damping that occurs at lower Machs and Q than the flutter boundary. Damping then increases as the Mach and Q increases before reducing again before the flutter boundary. Some of the estimated values show small positive damping. It should be noted that all dwell points were stable and the positive damping means there was a limit cycle oscillation or the model was approaching flutter onset. These positive damping results illustrate the difficulty in estimating damping using the test data. The values were positive in the time slice analyzed but the results would've been negative if a different time slice was chosen.

7.9 Closed Loop Flutter

Control laws for both system ID and FEM19 SSM were successful in suppressing flutter. The control laws were robust and suppressed flutter for a variety of Mach, dynamic pressures, and angle of attacks investigated. The post-holiday test results for alpha = -3,-1, +1, and +3 shown in

Figure 7.35 through Figure 7.38 include the stable closed loop points. The results show the stable closed loop test points going through the open loop unstable region and staying stable to much higher dynamic pressures.

7.10 Closed Loop Gust

A comparison of open and closed loop gust response RMS for the inboard wing strain gage are shown in Figure 7.39 through Figure 7.44. The gust responses were recorded as the airvane oscillation system (AOS) was swept from 0.5 to 13.5 Hz in 100 seconds, then a dwell at 13.5 Hz for 10 seconds, followed by a sweep from 13.5 Hz to 0.5 Hz in 60 seconds. The control laws used for the plotted results were based on the FEM19 SSM. The results show a peak response at the first bending mode and a smaller peak at the second bending mode. The second bending mode is a primary flutter mode and its gust response grows as the Mach and dynamics pressure approach the unstable region. The flutter suppression designed control laws show a large amount of gust load alleviation(GLA) at the second bending peak and a small amount of load alleviation everywhere else. A PSD type gust analysis would show some amount of GLA since the resulting load is a result of input gusts at all frequencies. A tuned discrete gust critical at the flutter frequency would show significant GLA while a tuned gust critical at other frequencies would show a small amount of GLA.

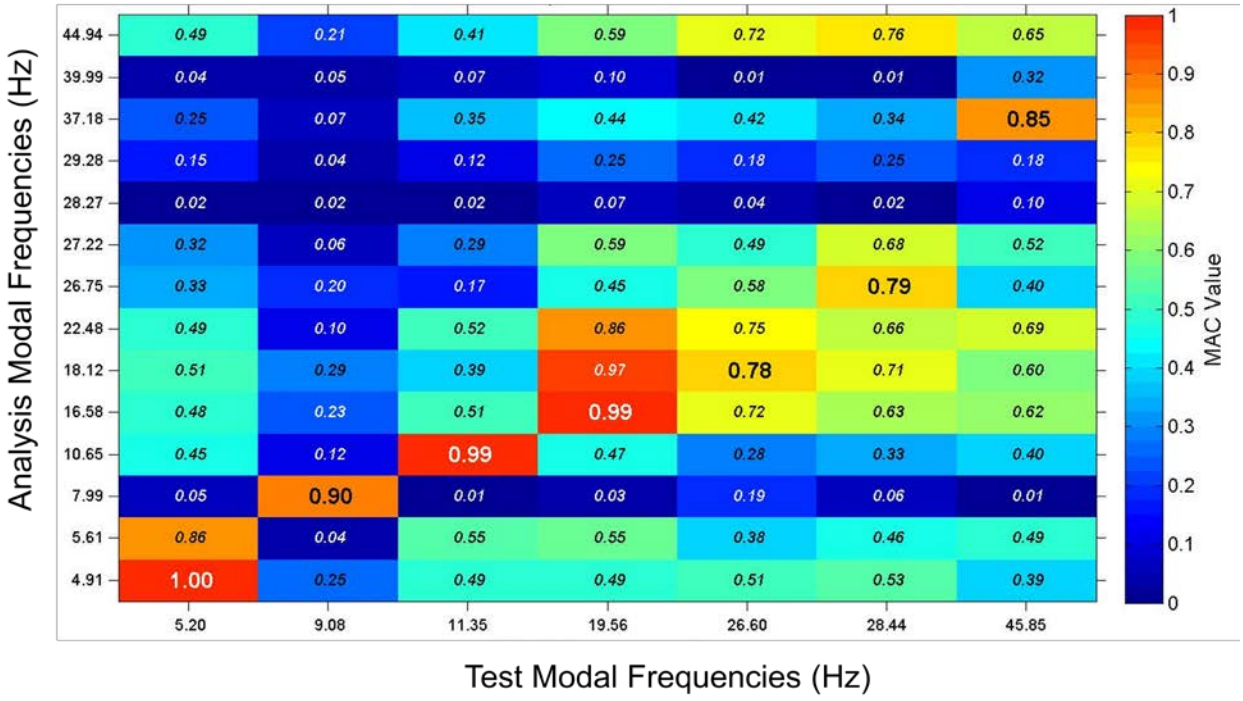

Figure 7.1 – Pre-Holiday GVT vs FEM18

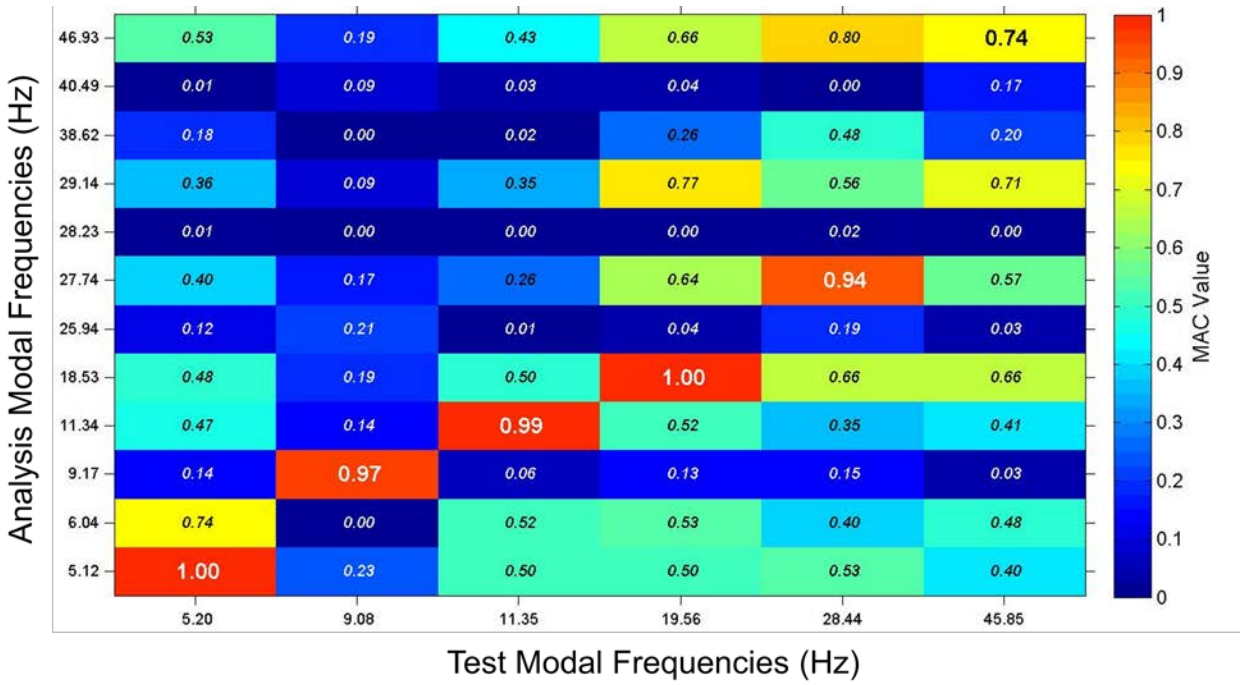

Figure 7.2 – Pre-Holiday GVT vs FEM19

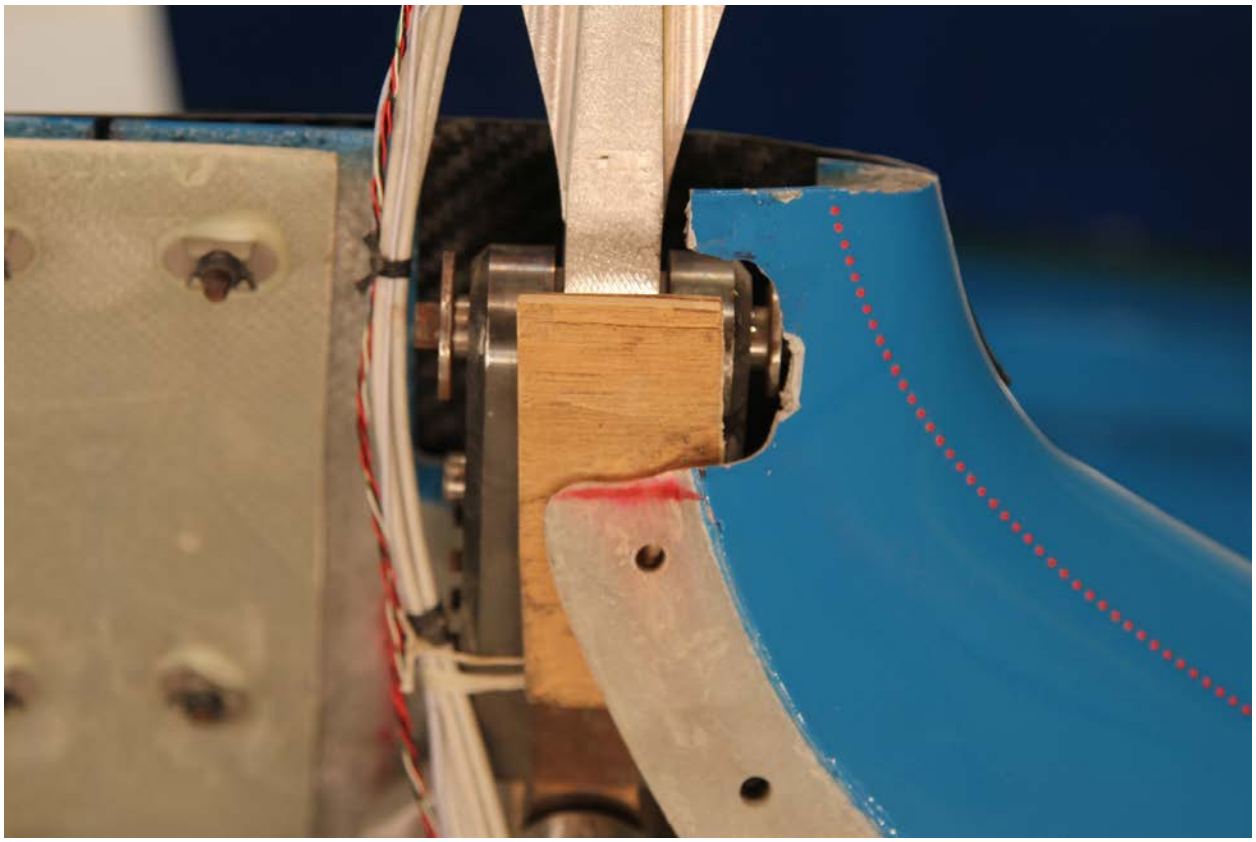

Figure 7.3 – Strut Root Fairing Cutout and Wedge

Table 7.1 – GVT Frequency Summary

		FEM 19								FEM 20					
Run		2	36	37	39	39	39	41	41	41	41	43	43	43	43
Point		14	1759	1768	1814	1819	1821	1848	1849	1850	1851	1892	1893	1894	1895
	Mode				2VPP	2.25V	1.5V	Wedge			Wedge		Wedge	Wedge	Wedge
	1	5.20	5.38	5.16	5.14	5.14	5.16	5.18	5.11	5.16	5.19	5.08	5.14	5.14	5.15
	3	9.10	8.47	8.61	8.60	8.65	8.61	9.04	8.68	8.46	8.70	8.43	8.72	8.75	8.73
	4	11.35	11.28	11.34	11.35	11.34	11.37	11.42	11.35	11.25	11.28	11.14	11.18	11.19	11.19
	5	19.57	19.45	18.95	18.80	18.78	18.84	19.19	18.69	18.70	19.04	18.62	19.04	19.09	19.12
	7	28.45	29.60	28.05	27.95	27.96	28.03	28.54	29.22	27.60	28.01	27.83	28.13	28.16	28.17

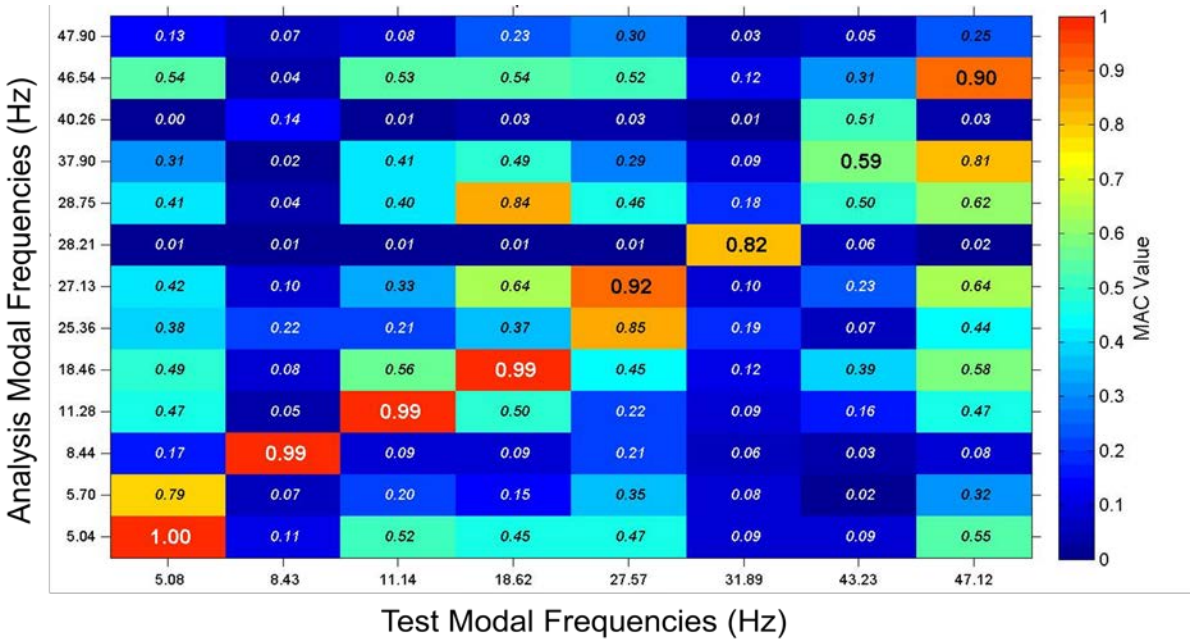

Figure 7.4 – Post-Holiday GVT vs FEM20

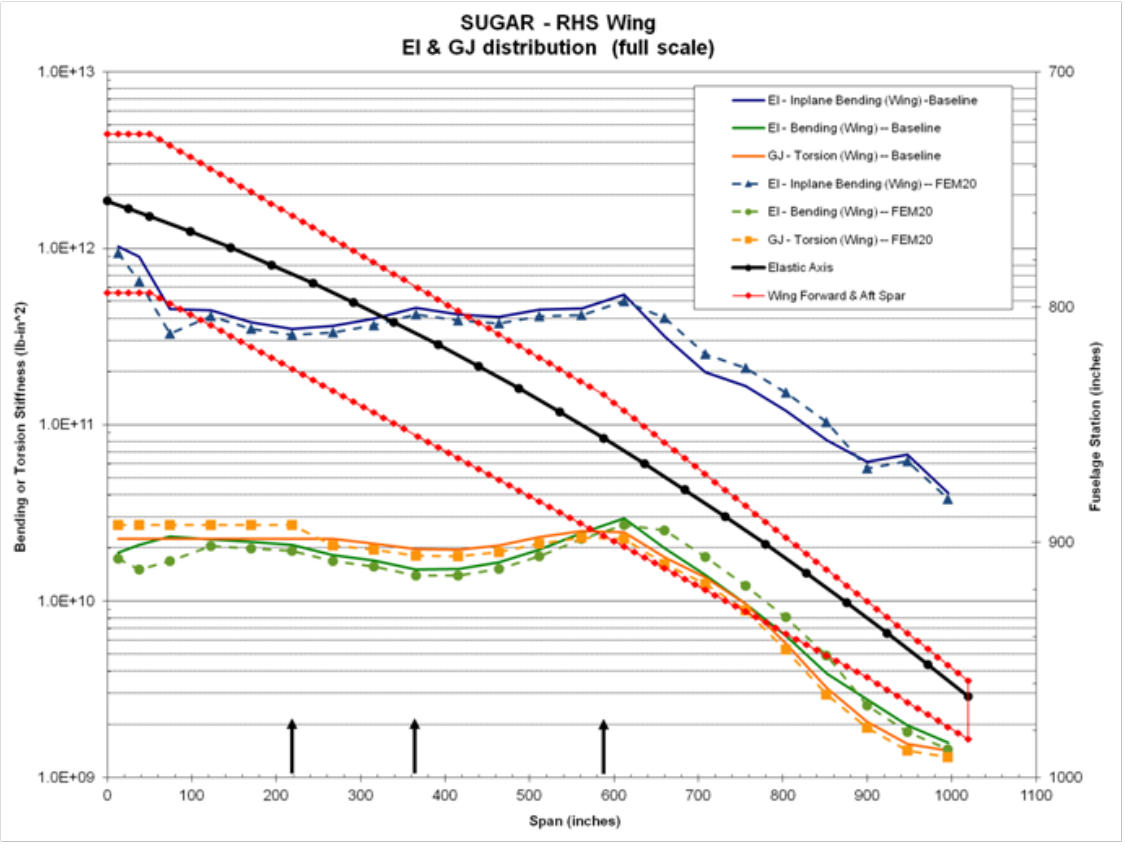

Figure 7.5 – FEM20 Wing Stiffness Distribution (Full Scale)

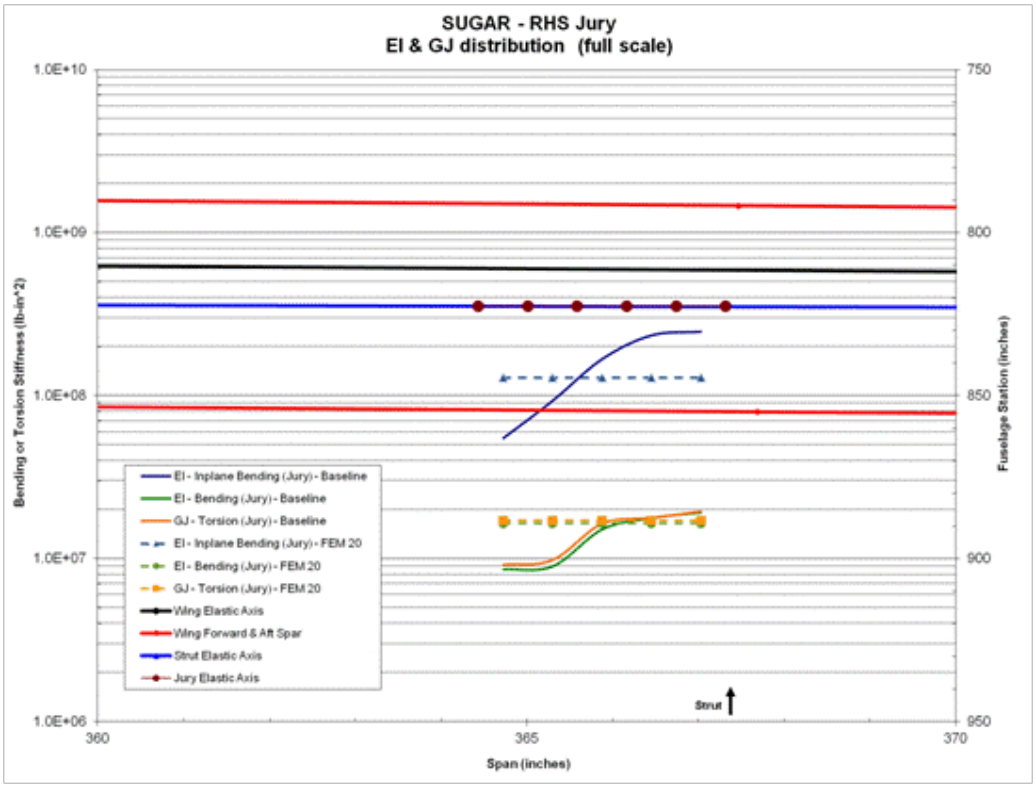

Figure 7.6 – FEM20 Jury Stiffness Distribution (Full Scale)

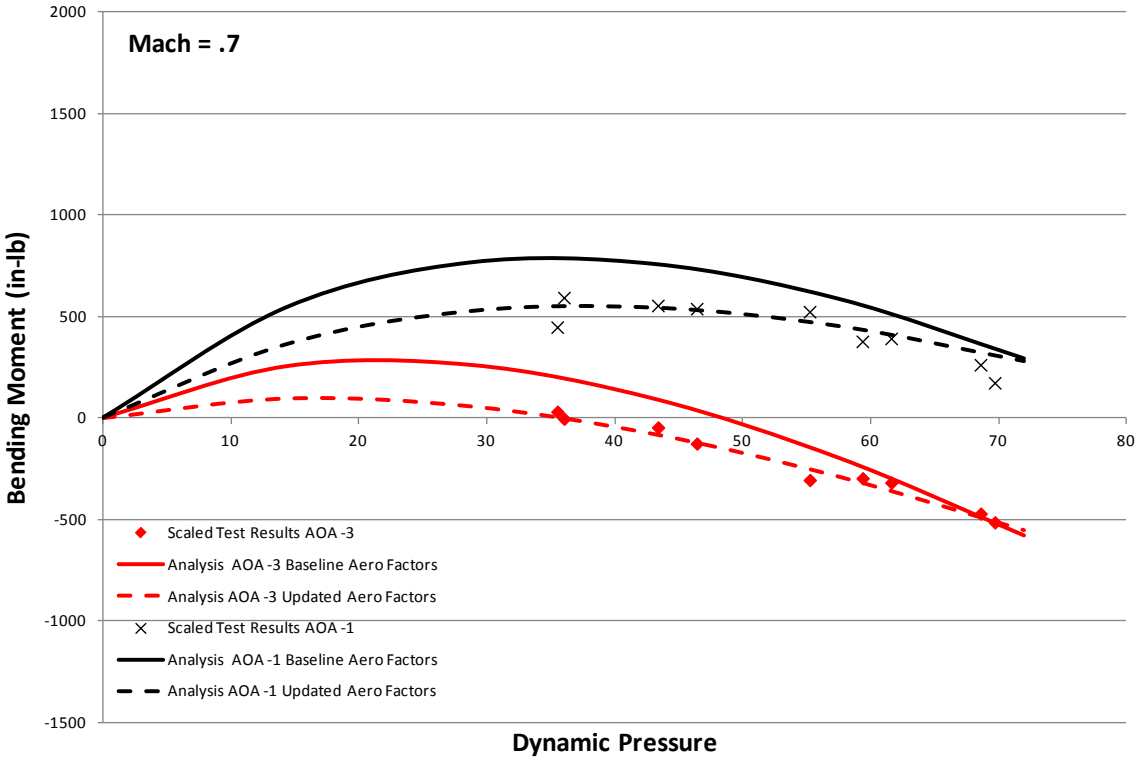

Figure 7.7 – Updated Static Aero Factors

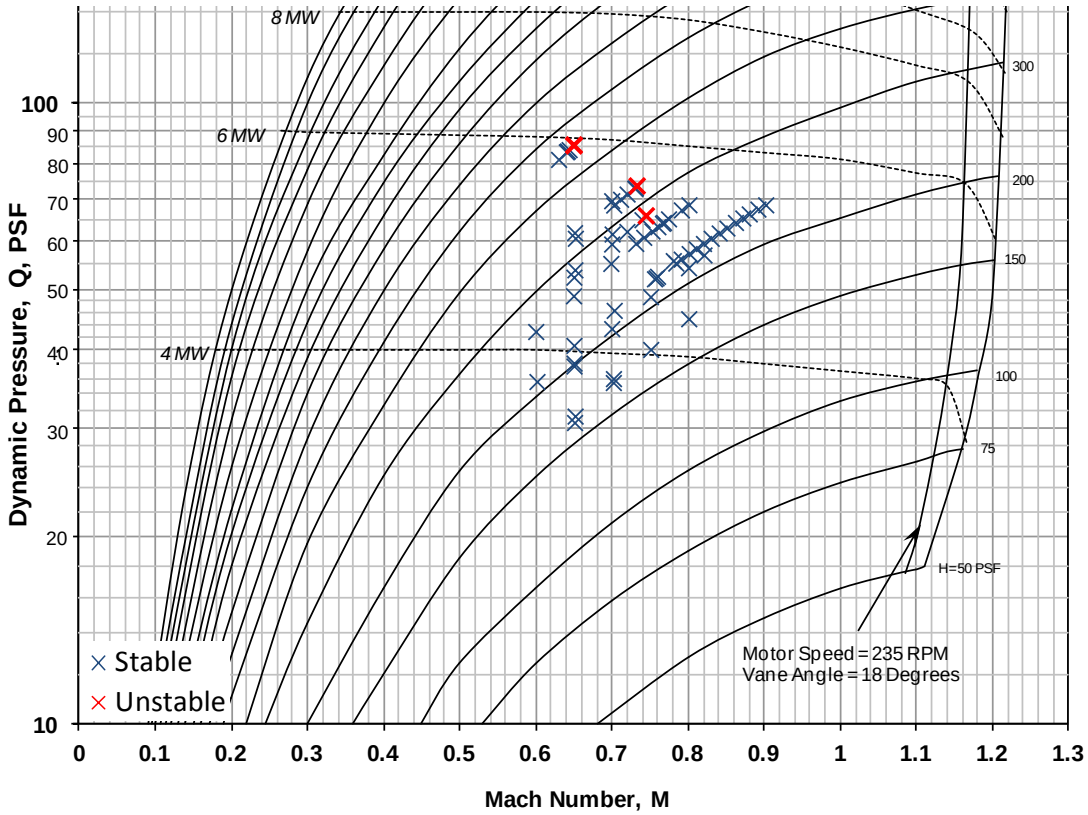

Figure 7.8 – Pre-Holiday Flutter Test Results Alpha=-3

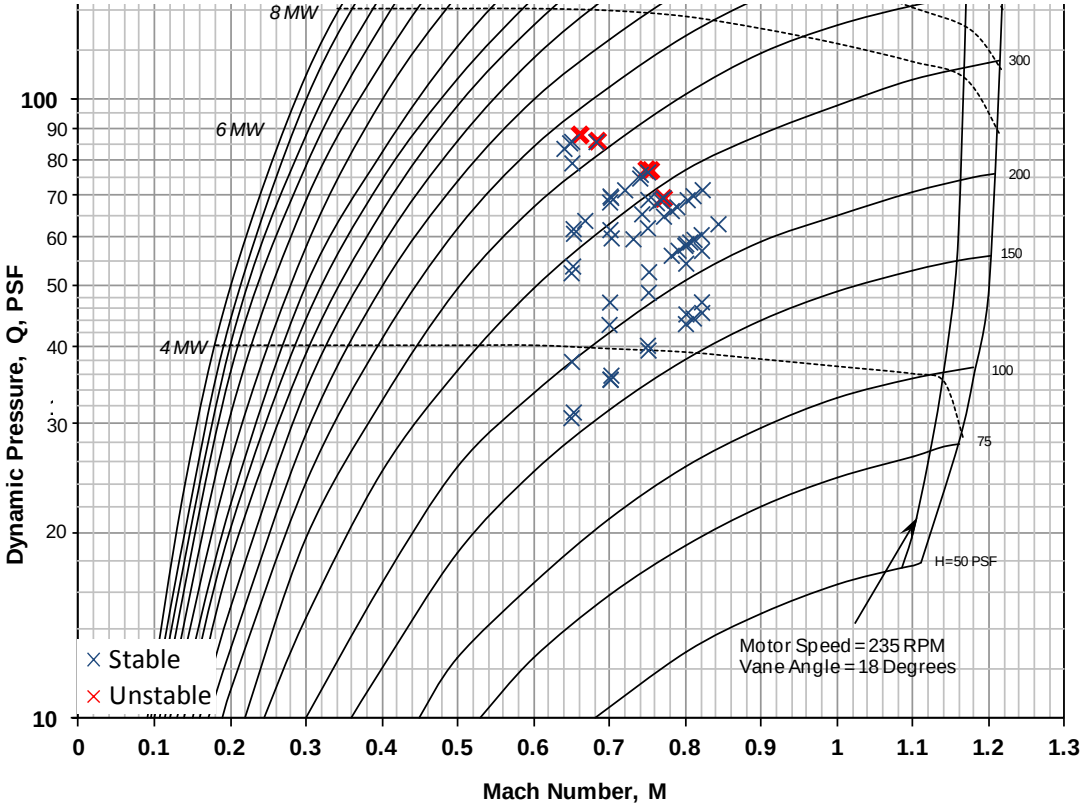

Figure 7.9 – Pre-Holiday Flutter Test Results Alpha = -1

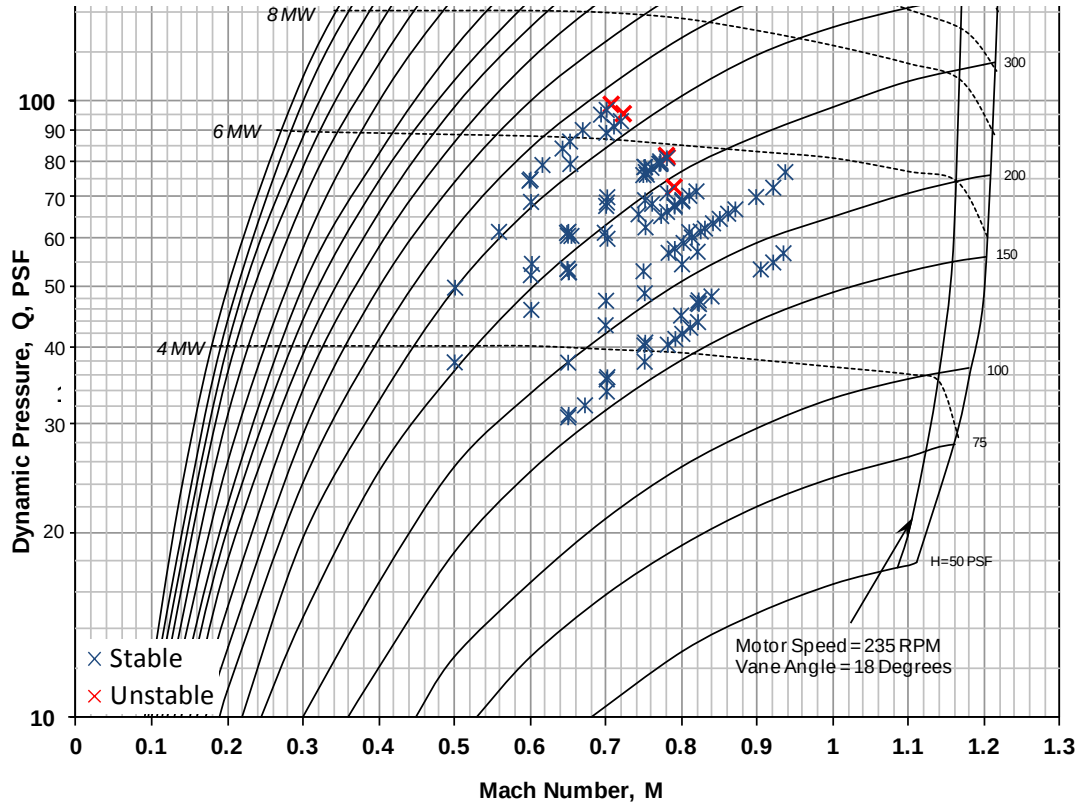

Figure 7.10 – Pre-Holiday Flutter Test Results Alpha = +1

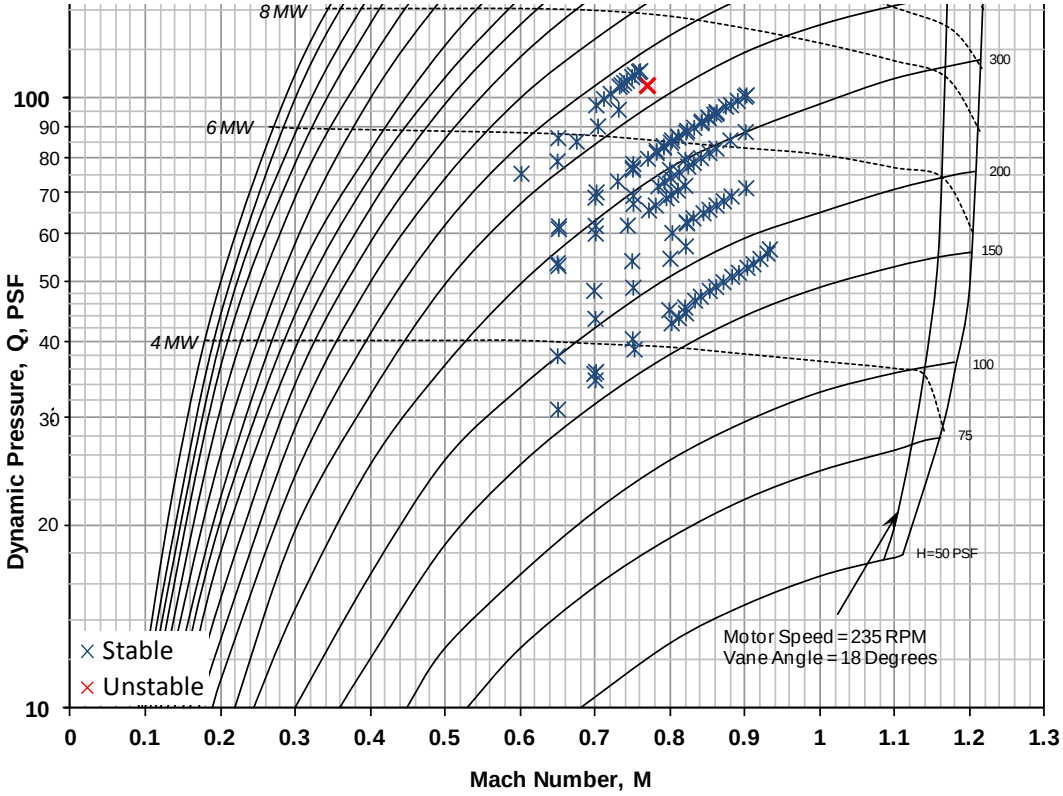

Figure 7.11 – Pre-Holiday Flutter Test Results Alpha = +3

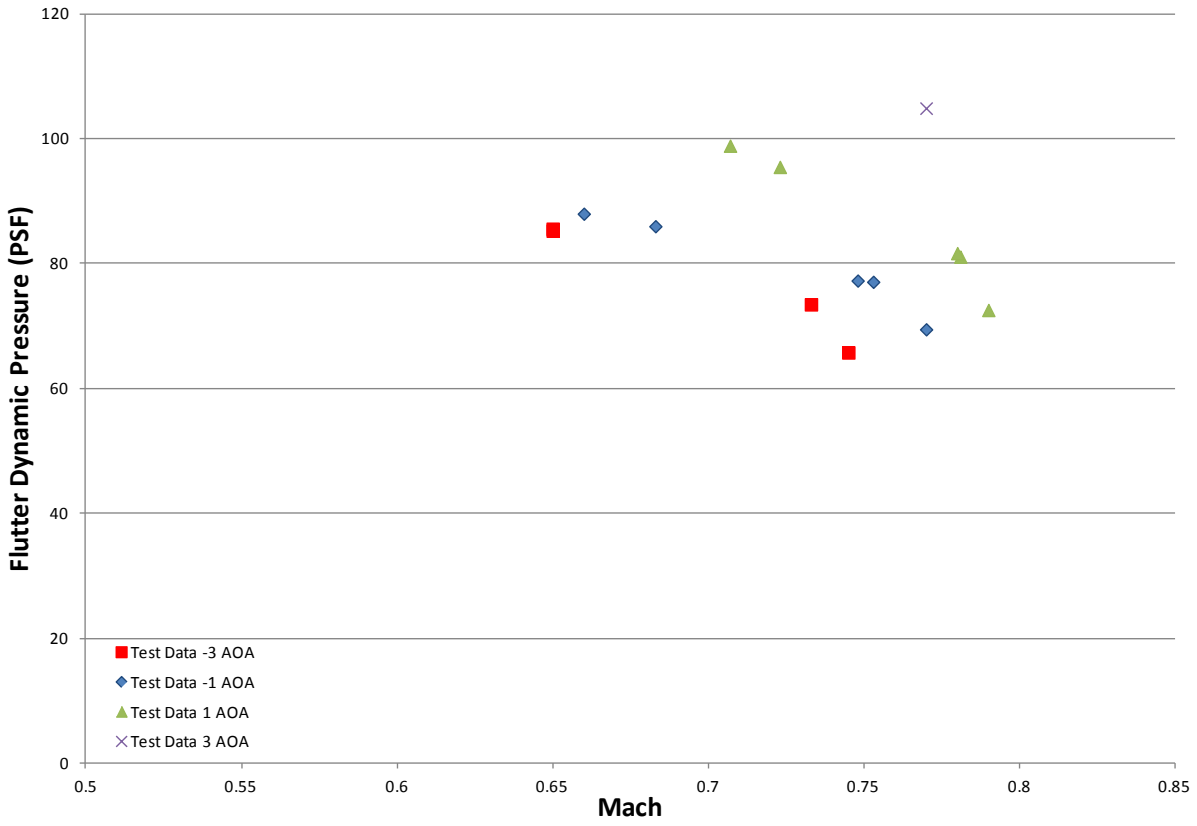

Figure 7.12 – Pre-Holiday Unstable Points

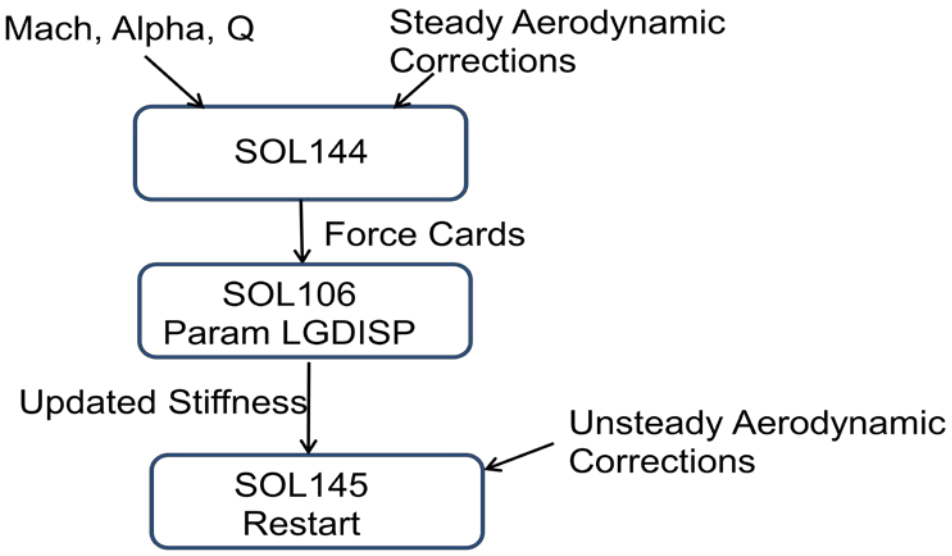

Figure 7.13 – Preload and Large Displacement Flutter

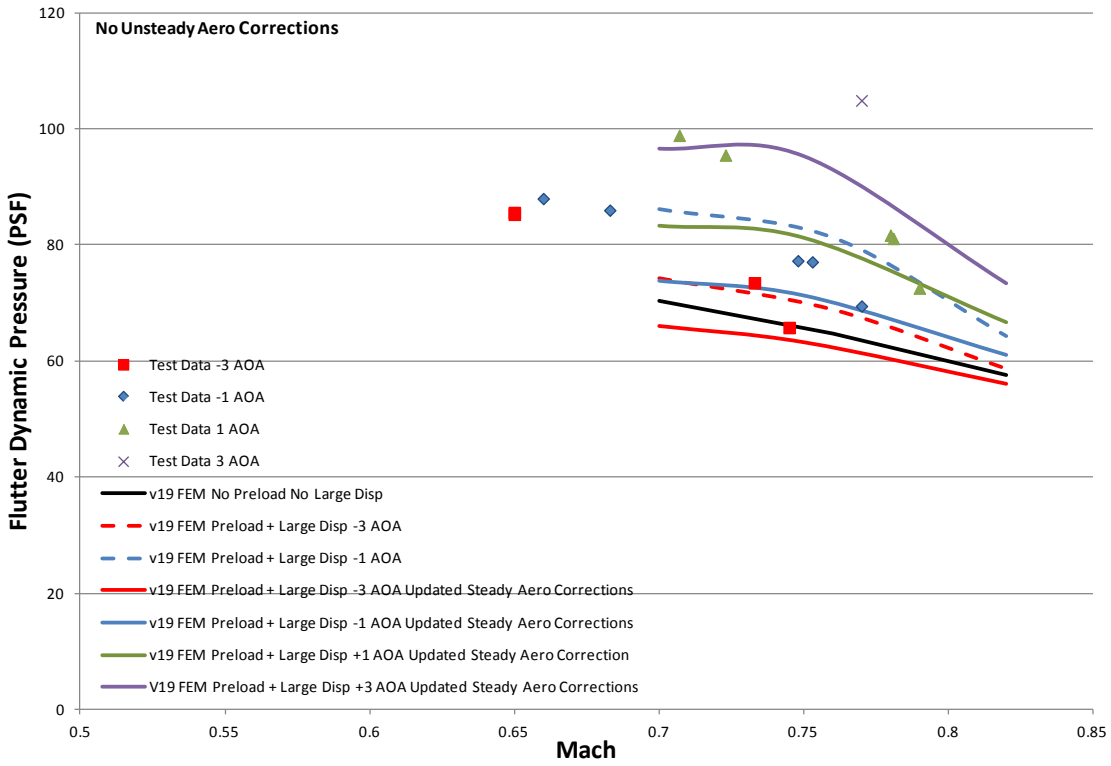

Figure 7.14 – Pre-Holiday Test vs Analysis

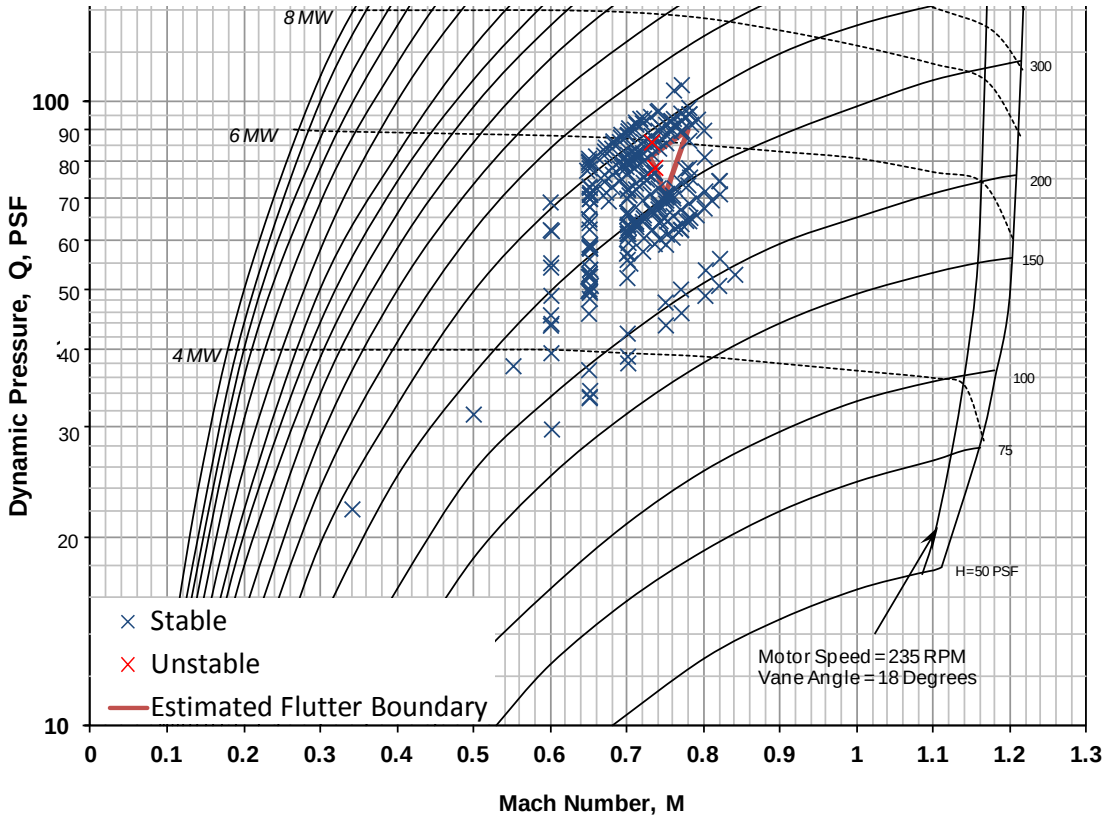

Figure 7.15 – Post-Holiday Flutter Results Alpha –3

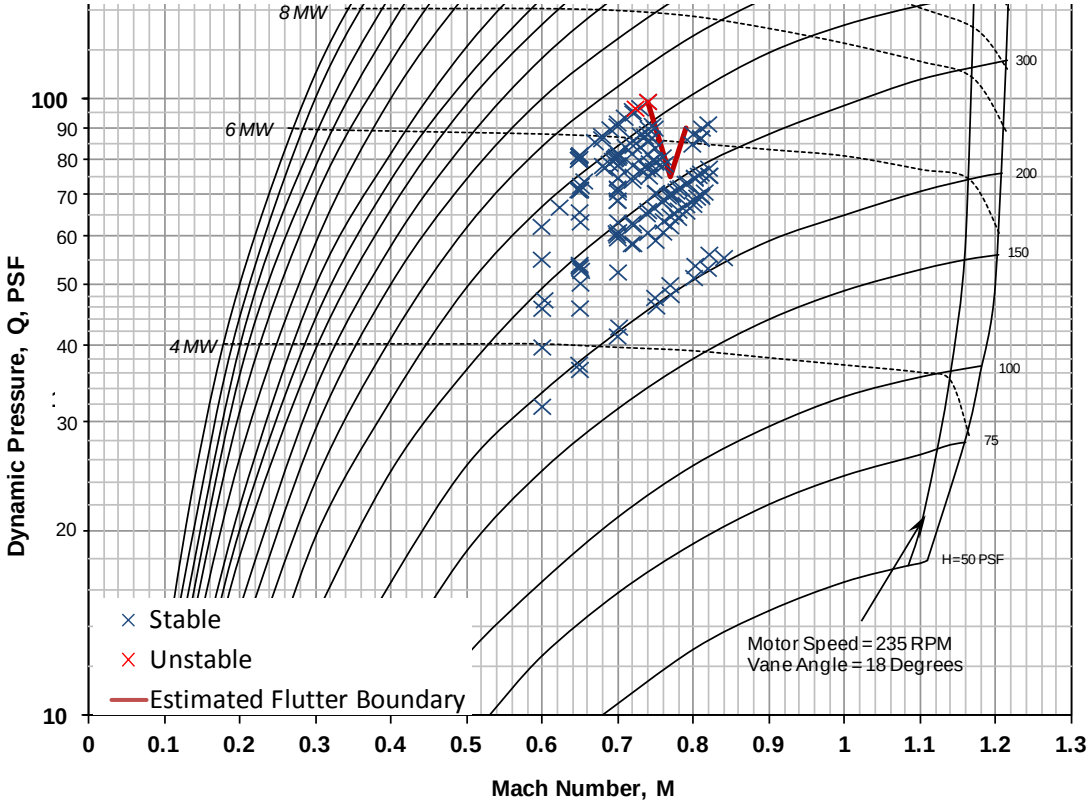

Figure 7.16 – Post-Holiday Flutter Results Alpha = -1

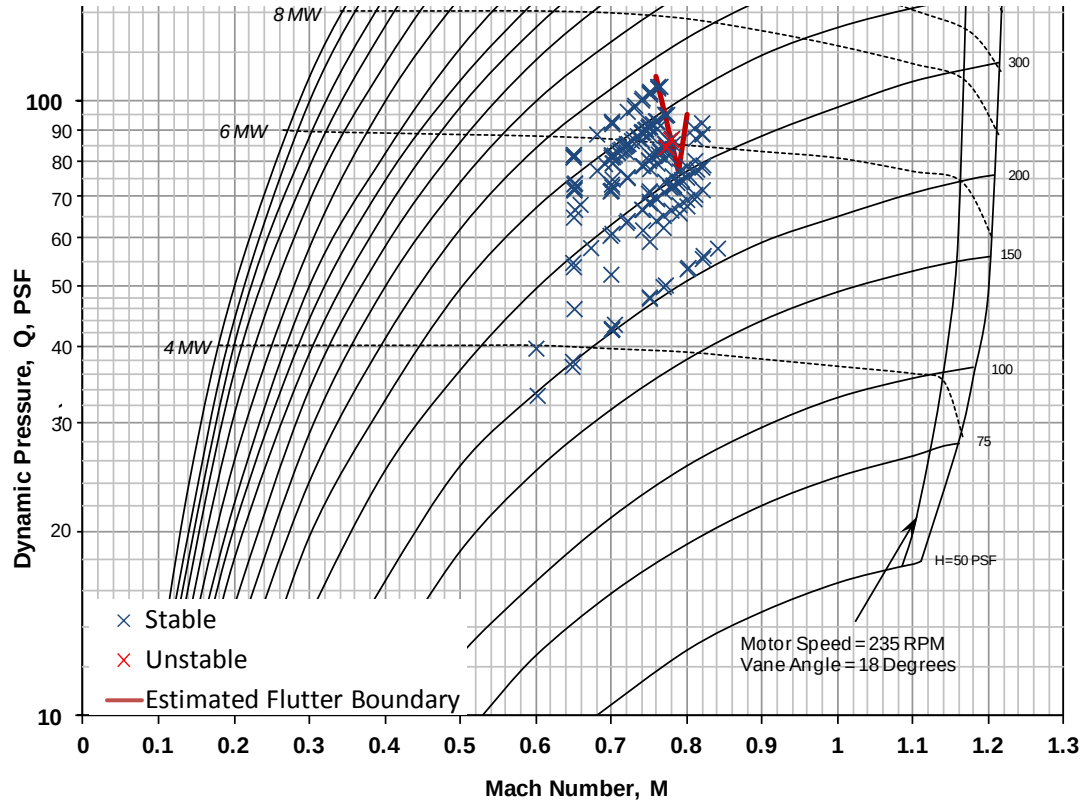

Figure 7.17 – Post-Holiday Flutter Results Alpha = +1

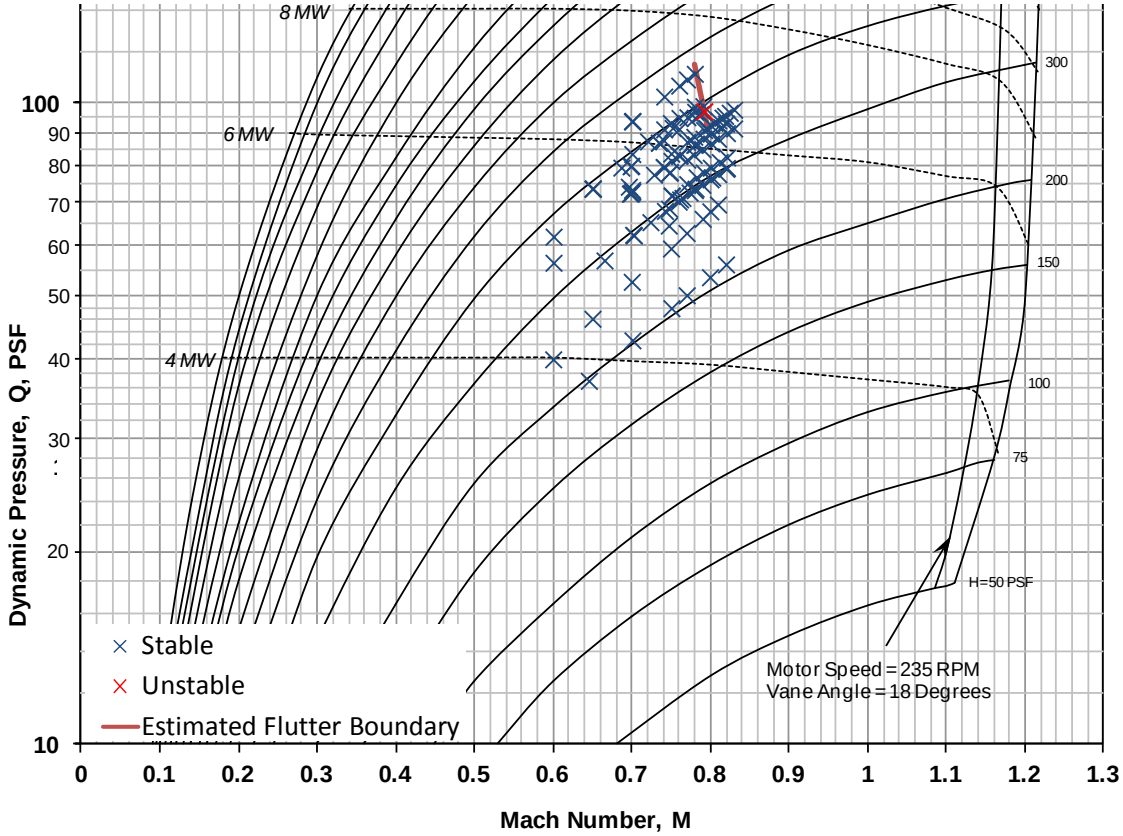

Figure 7.18 – Post-Holiday Flutter Results Alpha = +3

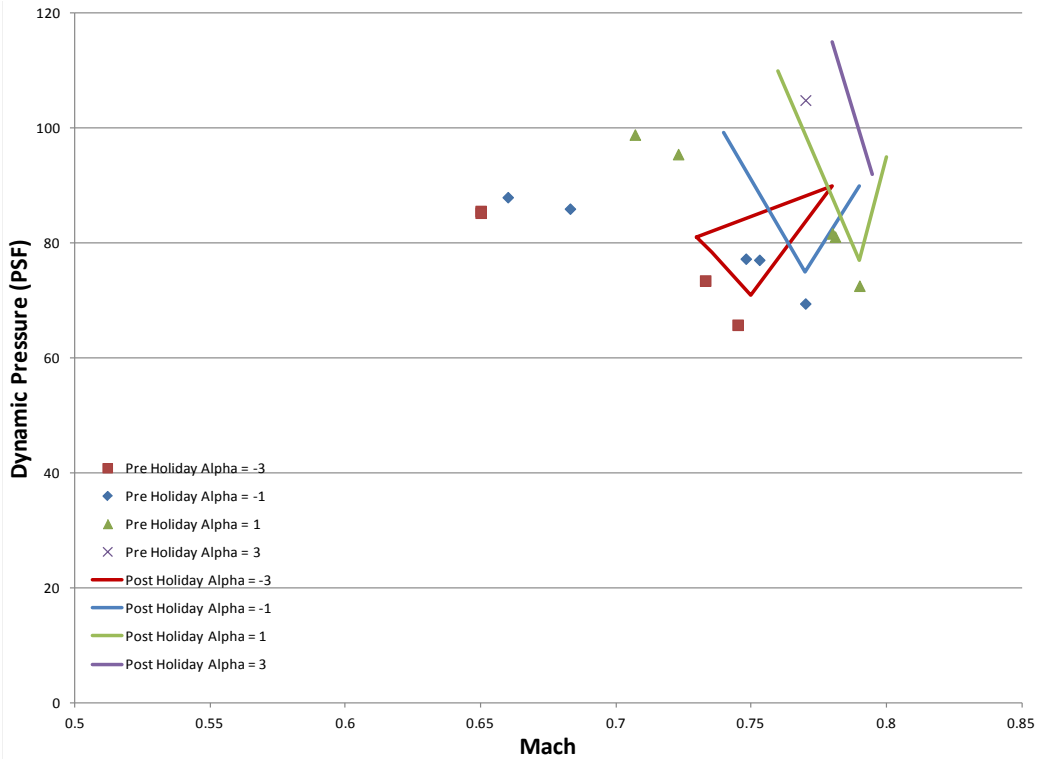

Figure 7.19 – Pre-Holiday vs Post holiday Test Results

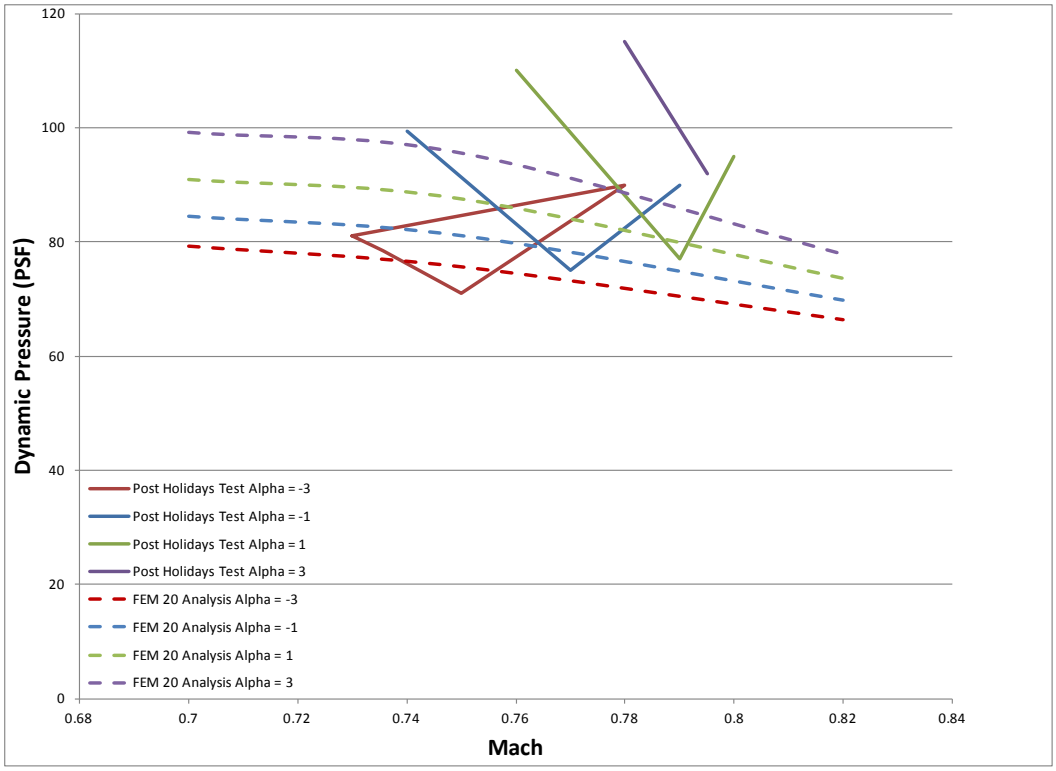

Figure 7.20 – Post Test Analysis vs Test

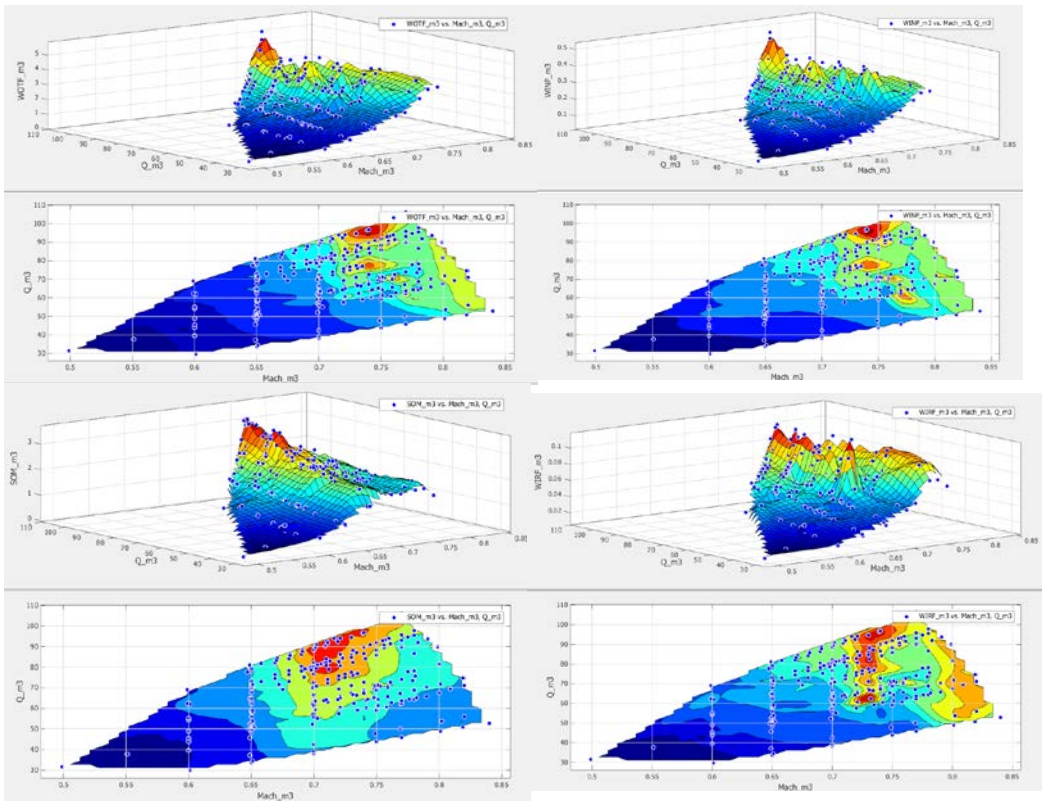

Figure 7.21 – Post-Holidays RMS Results Alpha = -3

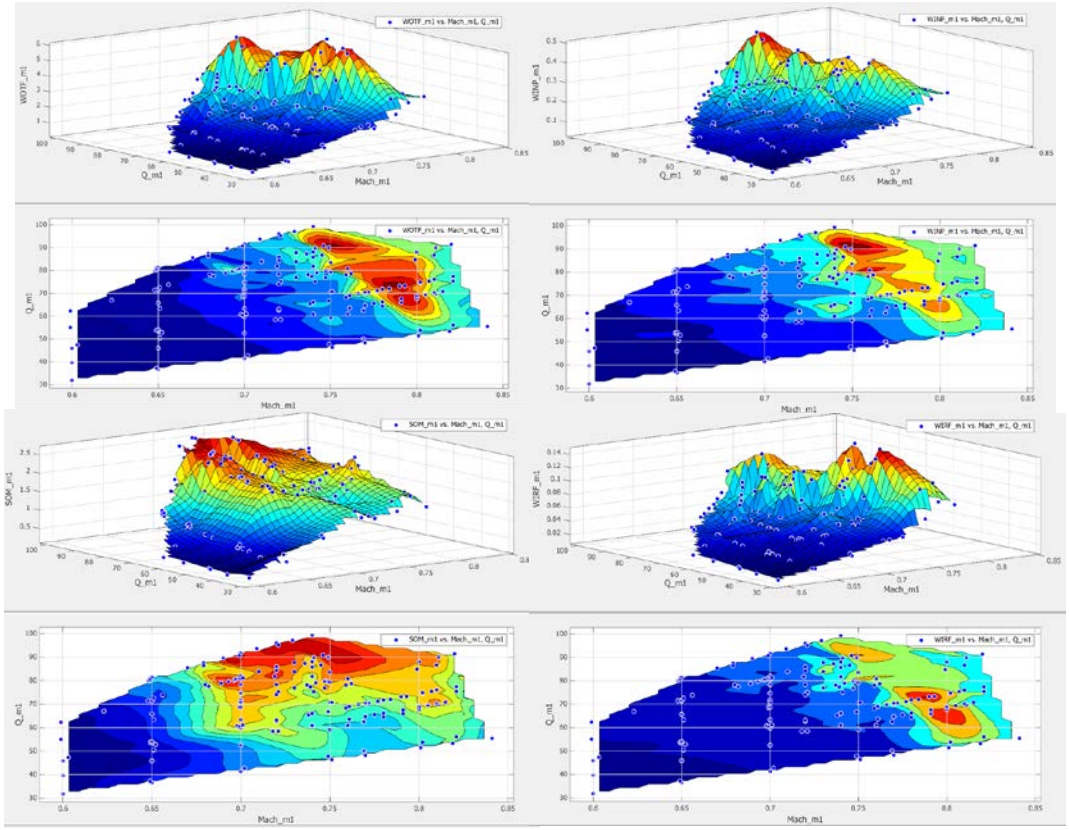

Figure 7.22 – Post-Holidays RMS Results Alpha = -1

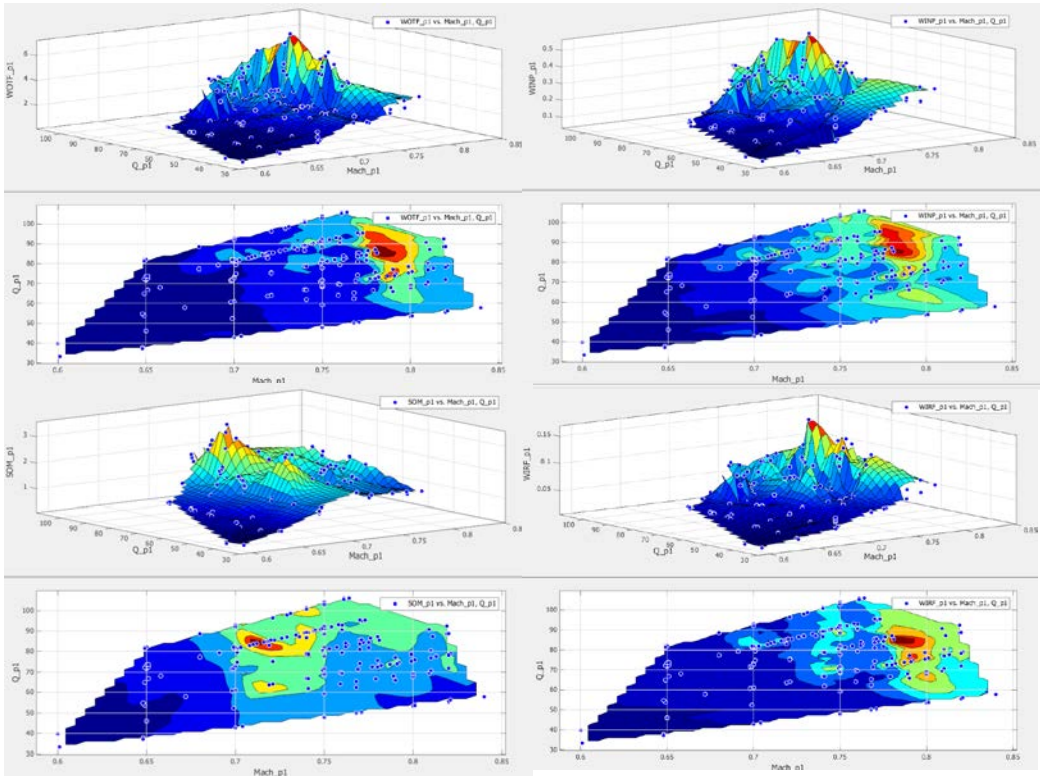

Figure 7.23 – Post-Holidays RMS Results Alpha = +1

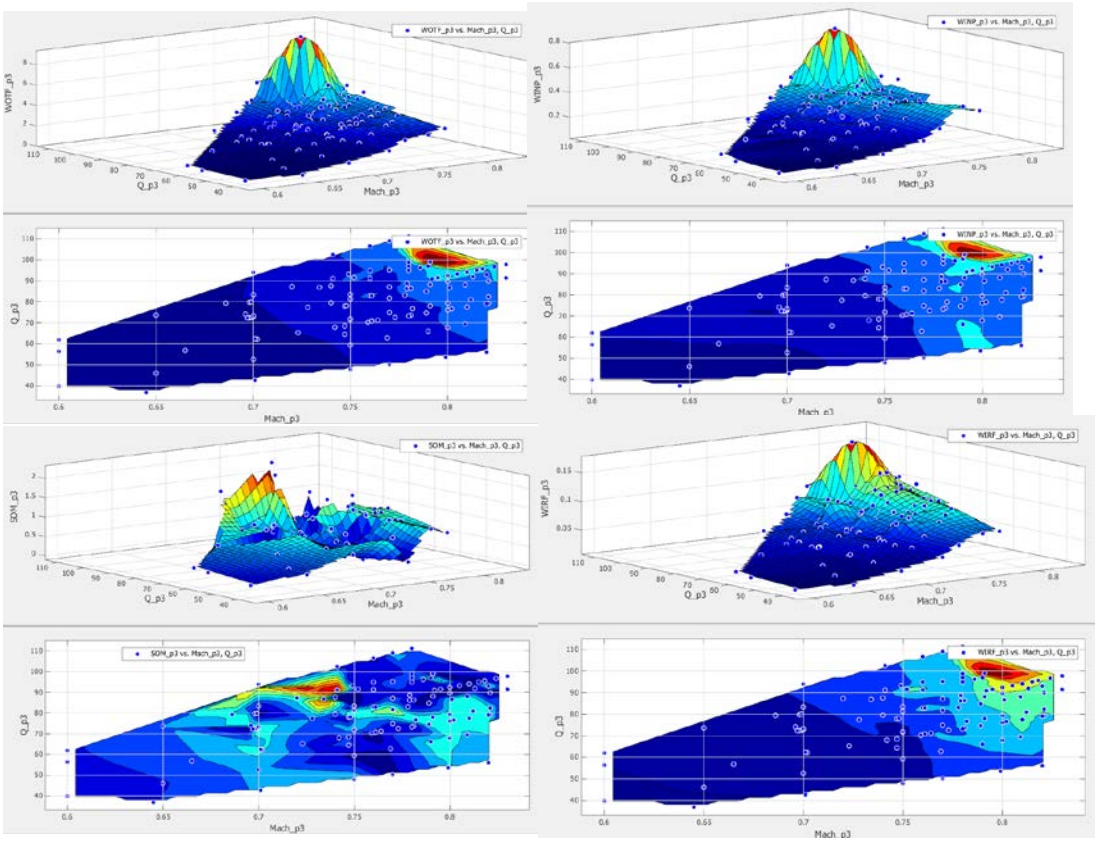

Figure 7.24 – Post-Holidays RMS Results Alpha = +3

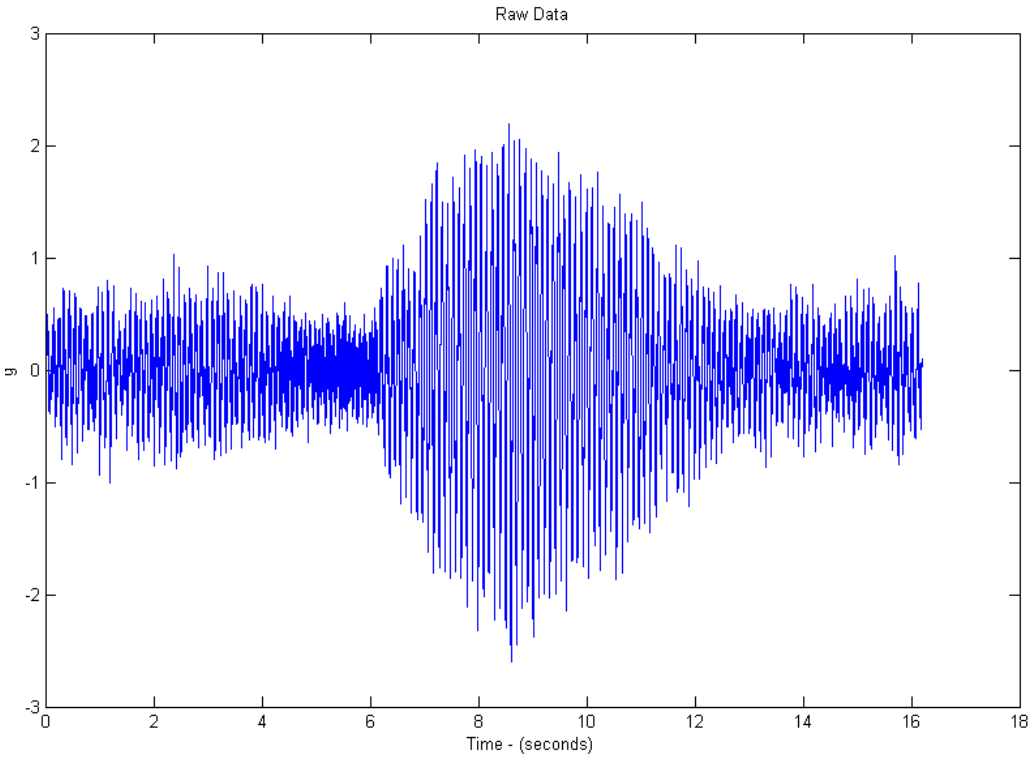

Figure 7.25 – Run 44 Tab Point 2007 Dwell Time History Data

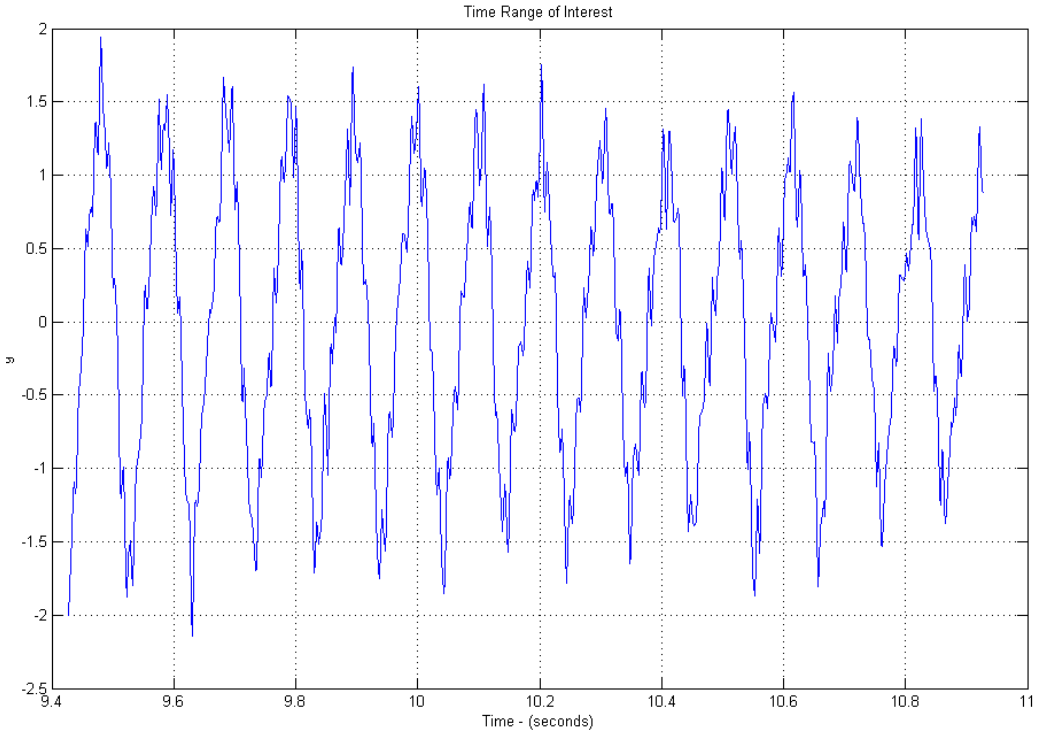

Figure 7.26 – Run 44 Tab Point 2007 Decay Time History

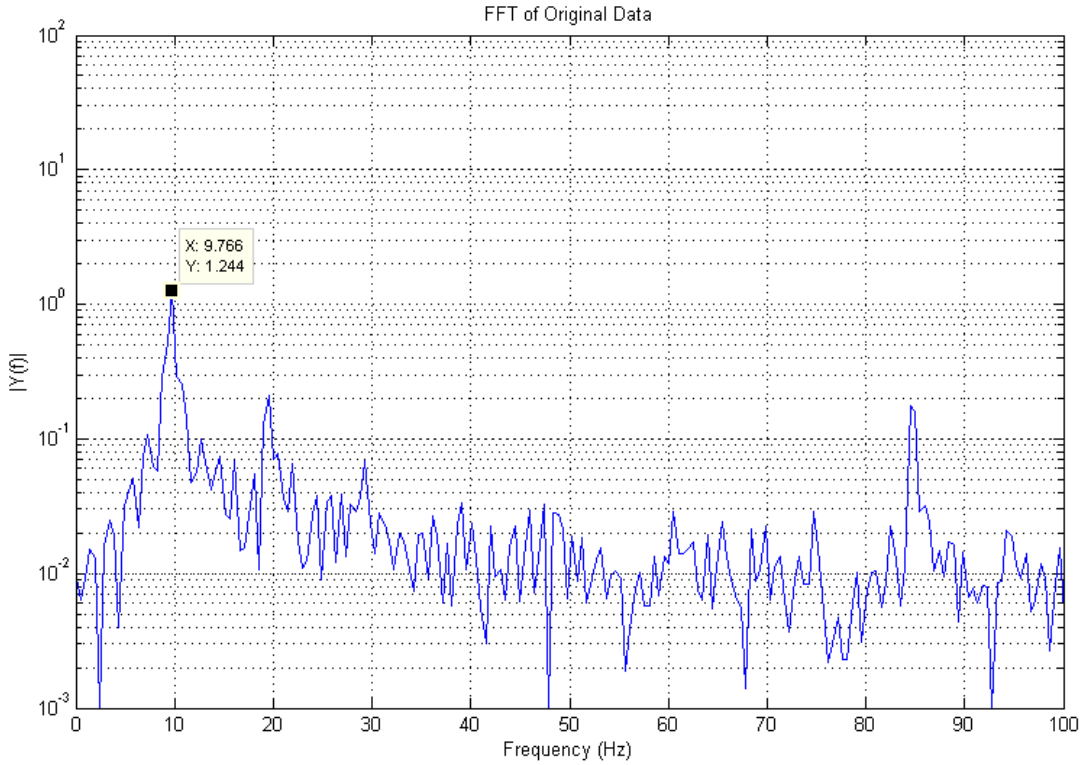

Figure 7.27 – Run 44 Tab Point 2007 FFT

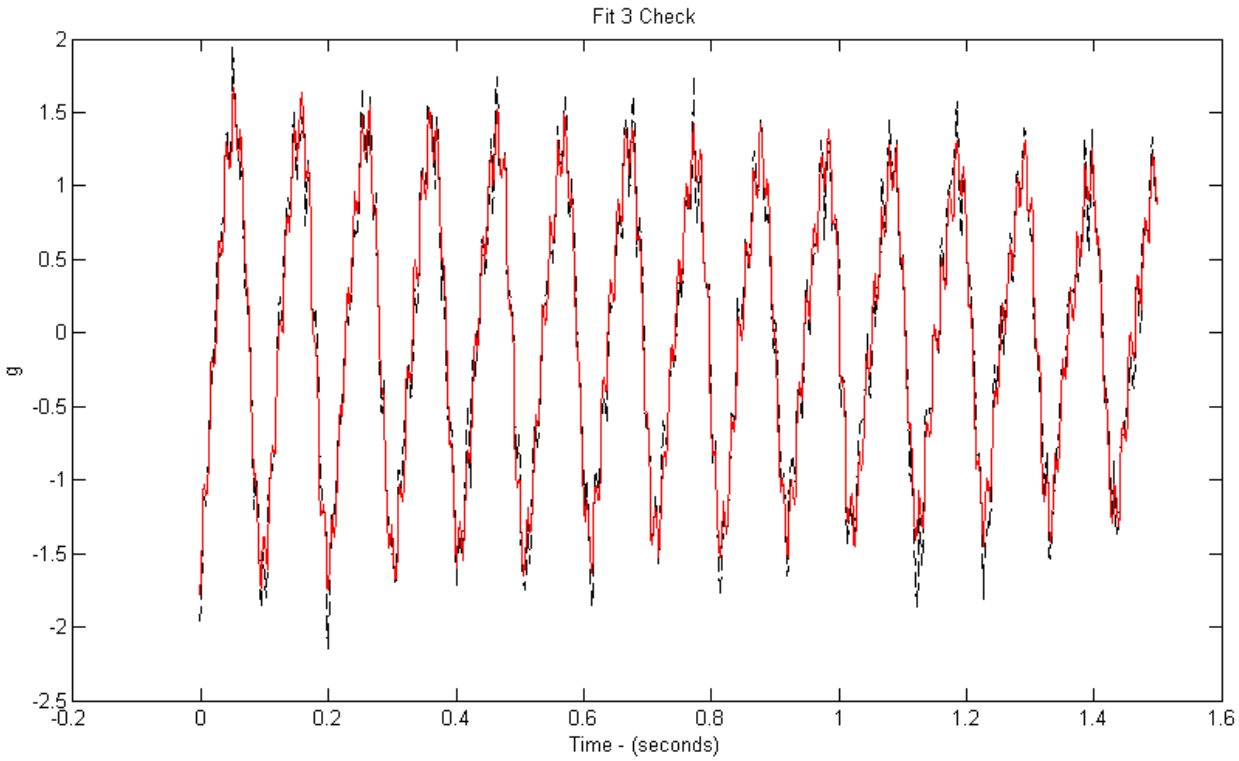

Figure 7.28 – Run 44 Tab Point 2007 3 Sine Wave Fit of Decay Time History

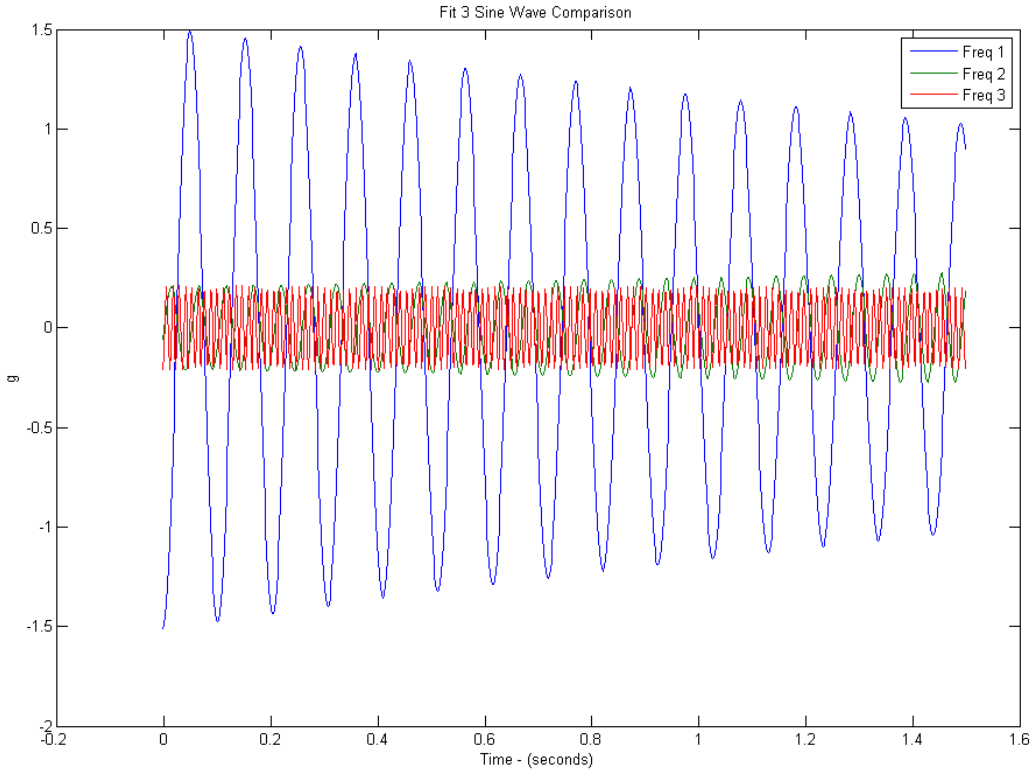

Figure 7.29 – Run 44 Tab Point 2007 3 Sine Wave Fit Results

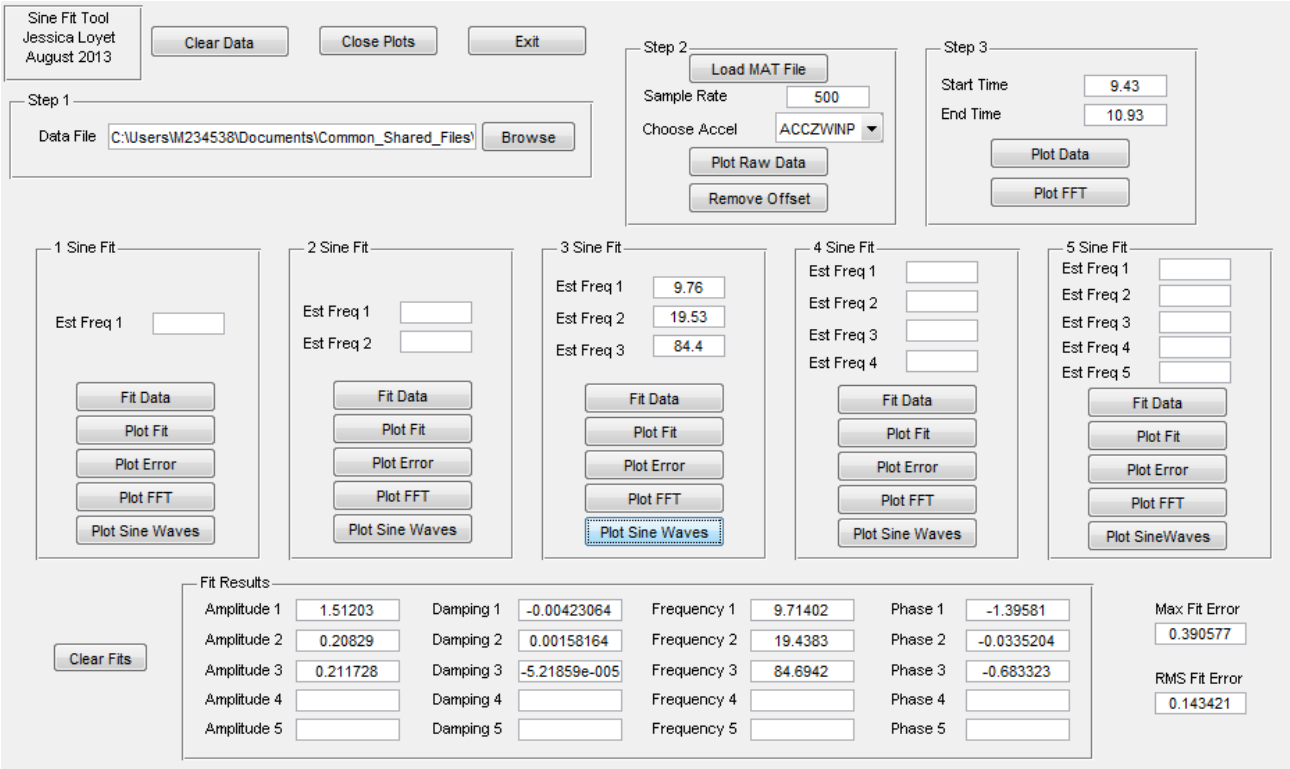

Figure 7.30 – Run 44 Tab Point 2007 3 Sine Wave Fit GUI

Table 7.2 – Sine Wave Fit Results for AOA = -3 degrees

		TDT Tunnel Parameters							
Run Number	Tab Point	Mach #	Dynamic Pressure	H (Main Ruskas)	Stagnation Temperature	MODAOA	Sine Fit Data		
		M	Q	H	TSTAGF	MODAOA			
		mean	mean	mean	mean	mean			
			psf	psf	degF	deg	Freq (Hz)	Damping (g)	# of Sine fits
63	4024	0.629	75.63	426.2	81.9	-3.00	10.089	-0.002	3 Sine
63	4031	0.638	77.72	427.9	82.1	-3.00	10.024	0.001	3 Sine
58	3506	0.639	78.41	430.0	77.9	-3.00	10.109	-0.004	3 Sine
58	3513	0.647	80.44	431.9	79.1	-3.00	10.034	-0.001	2 Sine
58	3513	0.647	80.44	431.9	79.1	-3.00	9.827	-0.003	3 Sine
58	3508	0.669	84.21	430.8	77.8	-3.00	9.857	-0.012	3 Sine
58	3508	0.669	84.21	430.8	77.8	-3.00	9.681	-0.021	3 Sine
63	4029	0.680	85.58	428.3	81.2	-3.00	9.745	-0.021	2 Sine
58	3509	0.680	86.51	432.0	78.2	-3.00	9.810	-0.011	2 Sine
58	3509	0.680	86.51	432.0	78.2	-3.00	9.820	-0.014	2 Sine
63	4028	0.680	85.64	428.3	81.2	-3.00	9.731	-0.014	3 Sine
63	4030	0.690	87.85	429.5	81.5	-3.00	9.839	-0.032	3 Sine
45	2127	0.690	78.40	381.6	76.7	-3.00	9.802	-0.032	3 Sine
58	3510	0.690	88.82	433.3	78.7	-3.00	9.790	-0.017	3 Sine
58	3510	0.690	88.82	433.3	78.7	-3.00	9.923	-0.010	3 Sine
44	1917	0.700	57.56	276.7	70.5	-3.00	9.520	-0.003	2 Sine
58	3511	0.700	90.82	434.5	79.2	-3.00	9.874	-0.015	2 Sine
58	3511	0.700	90.82	434.5	79.2	-3.00	9.931	-0.006	2 Sine
63	4026	0.700	89.74	429.7	81.6	-3.00	9.930	-0.001	3 Sine
58	3512	0.706	92.19	435.1	79.5	-3.00	10.005	-0.008	2 Sine
58	3512	0.706	92.19	435.1	79.5	-3.00	10.016	-0.010	2 Sine
45	2069	0.710	72.43	338.3	74.1	-3.00	9.608	-0.024	3 Sine
44	1920	0.720	60.53	278.7	71.4	-3.00	9.563	-0.033	3 Sine
45	2071	0.720	74.12	339.5	74.6	-3.00	9.774	-0.033	3 Sine
45	2073	0.724	74.94	340.4	75.2	-3.00	9.814	-0.012	5 Sine
45	2075	0.731	76.11	341.3	75.8	-3.00	9.830	-0.032	3 Sine
44	1932	0.740	63.87	282.7	74.0	-3.00	9.537	-0.020	3 Sine
44	1930	0.740	63.85	282.4	73.5	-3.00	9.645	-0.016	3 Sine
44	1937	0.741	64.18	283.7	72.9	-3.00	9.482	-0.017	3 Sine
44	2036	0.741	68.76	303.2	77.0	-3.00	9.583	-0.015	3 Sine
44	1940	0.746	65.11	284.7	73.3	-3.00	9.637	-0.033	3 Sine
57	3350	0.756	90.67	390.0	78.7	-3.00	9.835	-0.013	3 Sine

Table 7.3 – Sine Wave Fit Results for AOA = -2 and -1 degrees

Run Number	Tab Point	TDT Tunnel Parameters					Sine Fit Data		
		Mach #	Dynamic Pressure	H (Main Ruskas)	Stagnation Temperature	MODAOA			
		M	Q	H	TSTAGF	MODAOA			
		mean	mean	mean	mean	mean			
			psf	psf	degF	deg	Freq (Hz)	Damping (g)	# of Sine fits
63	4066	0.627	76.32	431.1	83.0	-2.00	9.860	-0.002	4 Sine
63	4056	0.680	86.42	431.9	82.2	-2.00	9.641	-0.025	3 Sine
63	4058	0.690	88.43	432.8	82.5	-2.00	10.112	-0.031	3 Sine
63	4060	0.700	90.60	433.6	82.5	-2.00	9.817	-0.032	3 Sine
63	4062	0.710	92.60	434.6	82.4	-2.00	9.924	-0.015	3 Sine
63	4064	0.720	94.89	435.9	82.6	-2.00	9.931	-0.016	3 Sine
63	4064	0.720	94.89	435.9	82.6	-2.00	10.050	-0.018	3 Sine

Run Number	Tab Point	TDT Tunnel Parameters					Sine Fit Data		
		Mach #	Dynamic Pressure	H (Main Ruskas)	Stagnation Temperature	MODAOA			
		M	Q	H	TSTAGF	MODAOA			
		mean	mean	mean	mean	mean			
			psf	psf	degF	deg	Freq (Hz)	Damping (g)	# of Sine fits
63	4075	0.680	86.56	433.1	82.3	-1.00	9.510	-0.033	3 Sine
63	4075	0.680	86.56	433.1	82.3	-1.00	9.964	-0.032	3 Sine
63	4077	0.700	90.82	435.0	82.2	-1.00	9.359	-0.034	3 Sine
63	4077	0.700	90.82	435.0	82.2	-1.00	9.668	-0.033	3 Sine
45	2090	0.719	74.92	343.7	76.9	-1.00	9.530	-0.012	3 Sine
44	1959	0.719	62.58	288.4	75.7	-1.00	9.420	-0.029	2 Sine
63	4079	0.720	95.01	437.0	82.6	-1.00	9.821	-0.018	3 Sine
63	4081	0.730	97.16	438.2	83.0	-1.00	9.530	-0.033	3 Sine
45	2093	0.736	77.99	345.8	77.9	-1.00	9.871	-0.021	2 Sine
63	4083	0.739	99.16	439.1	83.1	-1.00	9.958	-0.021	3 Sine
44	1961	0.739	65.44	290.2	76.5	-1.00	9.432	-0.008	3 Sine
44	1963	0.749	66.86	290.5	75.0	-1.00	9.481	-0.007	3 Sine
44	1966	0.759	68.46	292.0	75.0	-1.00	9.526	0.005	3 Sine
44	1965	0.760	68.43	291.8	74.6	-1.00	9.369	-0.034	3 Sine

Table 7.4 – Sine Wave Fit Results for AOA = 0 and 1 degrees

		TDT Tunnel Parameters					Sine Fit Data		
Run Number	Tab Point	Mach #	Dynamic Pressure	H (Main Ruskas)	Stagnation Temperature	MODAOA			
		M	Q	H	TSTAGF	MODAOA			
		mean	mean	mean	mean	mean			
			psf	psf	degF	deg	Freq (Hz)	Damping (g)	# of Sine fits
63	4115	0.676	87.23	439.5	84.2	0.00	9.73	-0.006	4 Sine
63	4120	0.679	87.95	440.3	84.1	0.00	9.606	-0.018	3 Sine
63	4121	0.720	96.39	443.2	83.9	0.00	9.363	0.009	3 Sine
63	4108	0.739	99.60	441.2	83.1	0.00	10.231	-0.031	3 Sine
63	4126	0.755	103.62	445.3	83.9	0.00	9.644	-0.011	4 Sine
63	4112	0.779	108.22	445.6	84.0	0.00	9.131	-0.032	3 Sine

		TDT Tunnel Parameters					Sine Fit Data		
Run Number	Tab Point	Mach #	Dynamic Pressure	H (Main Ruskas)	Stagnation Temperature	MODAOA			
		M	Q	H	TSTAGF	MODAOA			
		mean	mean	mean	mean	mean			
			psf	psf	degF	deg	Freq (Hz)	Damping (g)	# of Sine fits
63	4133	0.604	72.87	436.8	83.2	1.00	9.632	-0.033	3 Sine
63	4145	0.682	88.73	441.6	84.1	1.00	9.765	0.001	3 Sine
63	4134	0.720	96.40	442.9	83.0	1.00	9.704	-0.026	3 Sine
63	4134	0.720	96.40	442.9	83.0	1.00	9.655	-0.033	3 Sine
63	4136	0.731	98.72	444.1	83.4	1.00	9.488	-0.034	3 Sine
63	4136	0.731	98.72	444.1	83.4	1.00	9.741	-0.029	3 Sine
63	4138	0.740	100.70	445.1	83.6	1.00	9.741	-0.031	3 Sine
63	4138	0.740	100.70	445.1	83.6	1.00	10.136	-0.031	3 Sine
63	4138	0.740	100.70	445.1	83.6	1.00	10.037	-0.032	3 Sine
45	2103	0.740	78.87	347.2	77.2	1.00	10.012	0.019	3 Sine
44	1987	0.741	67.05	296.1	76.1	1.00	9.637	-0.005	3 Sine
63	4140	0.750	102.89	446.3	83.9	1.00	9.625	-0.014	2 Sine
44	1990	0.760	70.12	298.3	77.2	1.00	9.675	-0.015	3 Sine
63	4143	0.765	106.25	448.0	84.3	1.00	9.955	-0.032	3 Sine
44	1992	0.770	71.64	299.4	77.8	1.00	9.809	0.019	3 Sine

Table 7.5 – Sine Wave Fit Results for AOA = +2 and +3 degrees

		TDT Tunnel Parameters					Sine Fit Data		
Run Number	Tab Point	Mach #	Dynamic Pressure	H (Main Ruskas)	Stagnation Temperature	MODAOA			
		M	Q	H	TSTAGF	MODAOA			
		mean	mean	mean	mean	mean			
			psf	psf	degF	deg	Freq (Hz)	Damping (g)	# of Sine fits
63	4157	0.740	101.37	447.6	84.4	2.00	9.862	-0.025	1 Sine
63	4157	0.740	101.37	447.6	84.4	2.00	9.937	-0.032	2 Sine
63	4157	0.740	101.37	447.6	84.4	2.00	9.973	-0.032	3 Sine
63	4159	0.760	105.76	449.8	84.8	2.00	9.895	-0.031	3 Sine
63	4159	0.760	105.76	449.8	84.8	2.00	9.947	-0.032	3 Sine
63	4155	0.719	96.90	445.6	84.2	2.00	9.876	-0.032	3 Sine
63	4155	0.719	96.90	445.6	84.2	2.00	9.854	-0.029	3 Sine

		TDT Tunnel Parameters					Sine Fit Data		
Run Number	Tab Point	Mach #	Dynamic Pressure	H (Main Ruskas)	Stagnation Temperature	MODAOA			
		M	Q	H	TSTAGF	MODAOA			
		mean	mean	mean	mean	mean			
			psf	psf	degF	deg	Freq (Hz)	Damping (g)	# of Sine fits
44	2007	0.762	70.91	301.0	77.6	3.00	9.714	-0.008	3 Sine

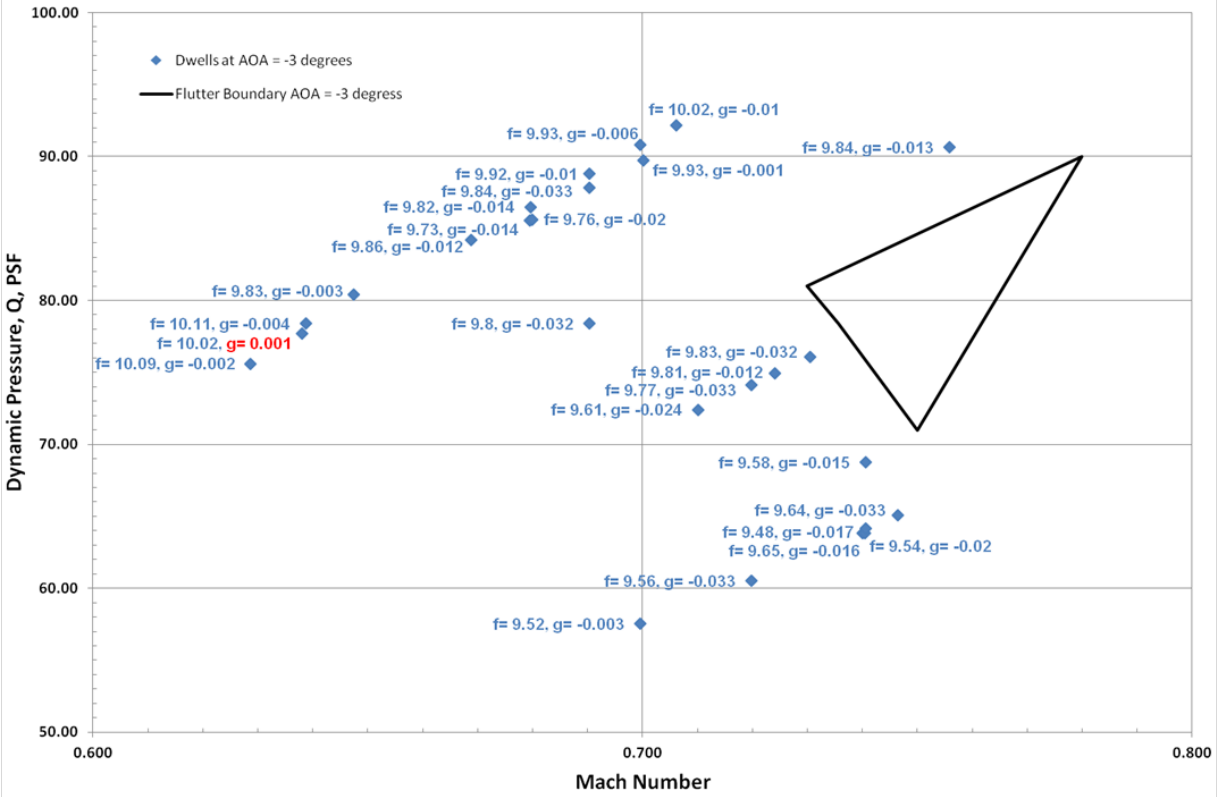

Figure 7.31 – Dwell Frequency and Damping Estimates Alpha = -3 degrees

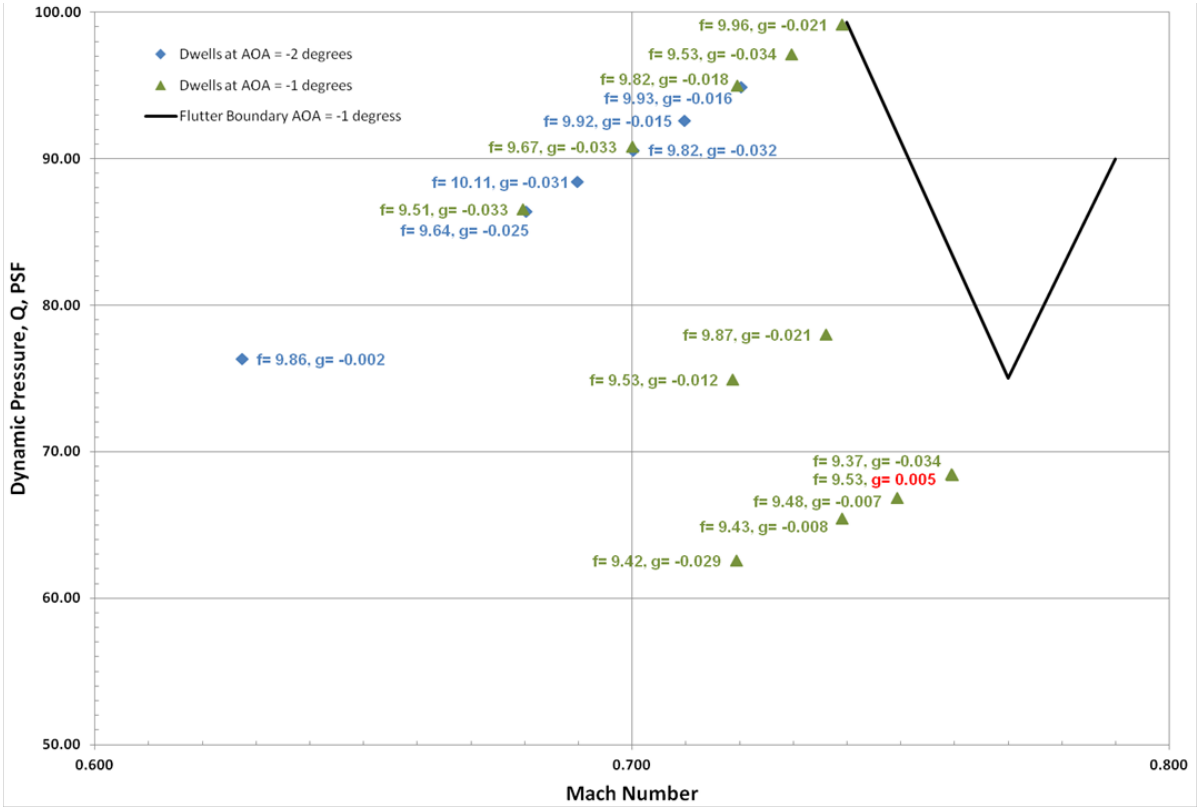

Figure 7.32 – Dwell Frequency and Damping Estimates Alpha = -2 & -1 degrees

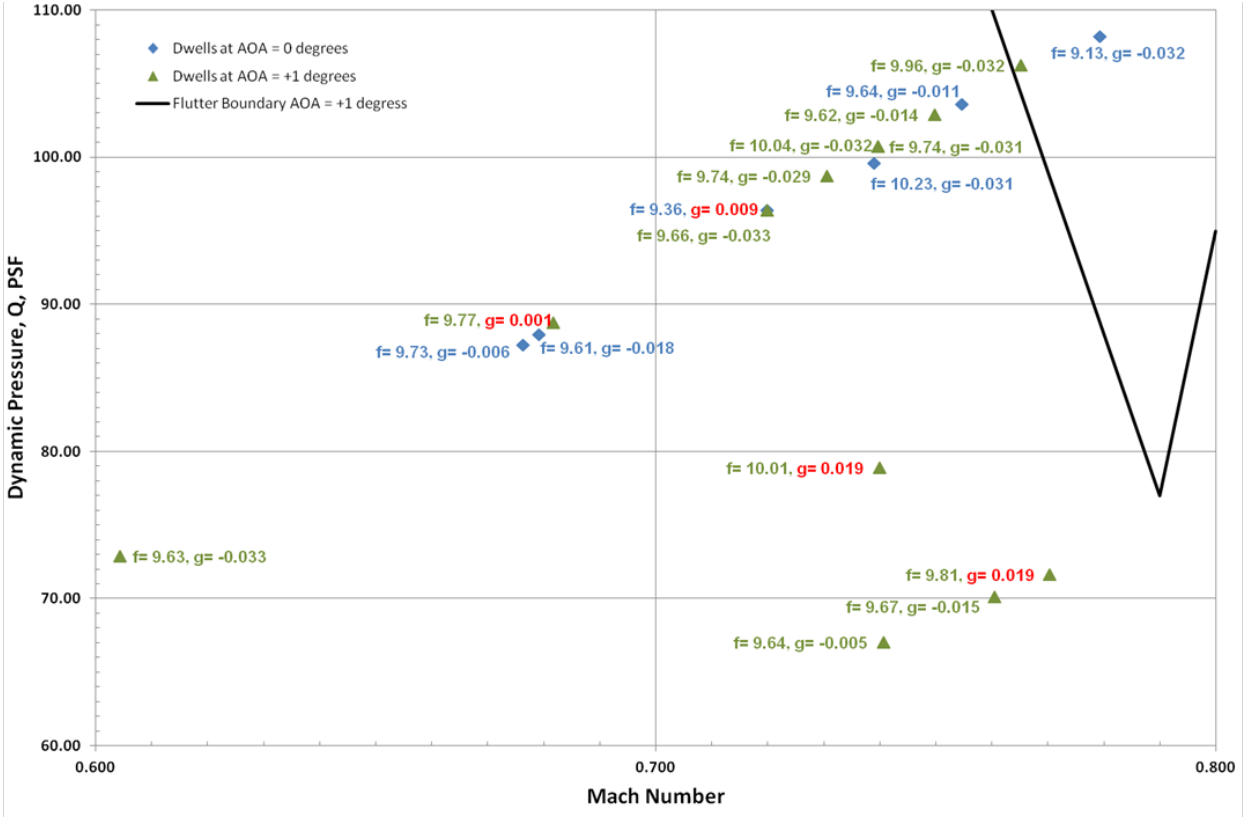

Figure 7.33 – Dwell Frequency and Damping Estimates Alpha = 0 & +1 degrees

Figure 7.34 – Dwell Frequency and Damping Estimates Alpha = 0 & +1 degrees

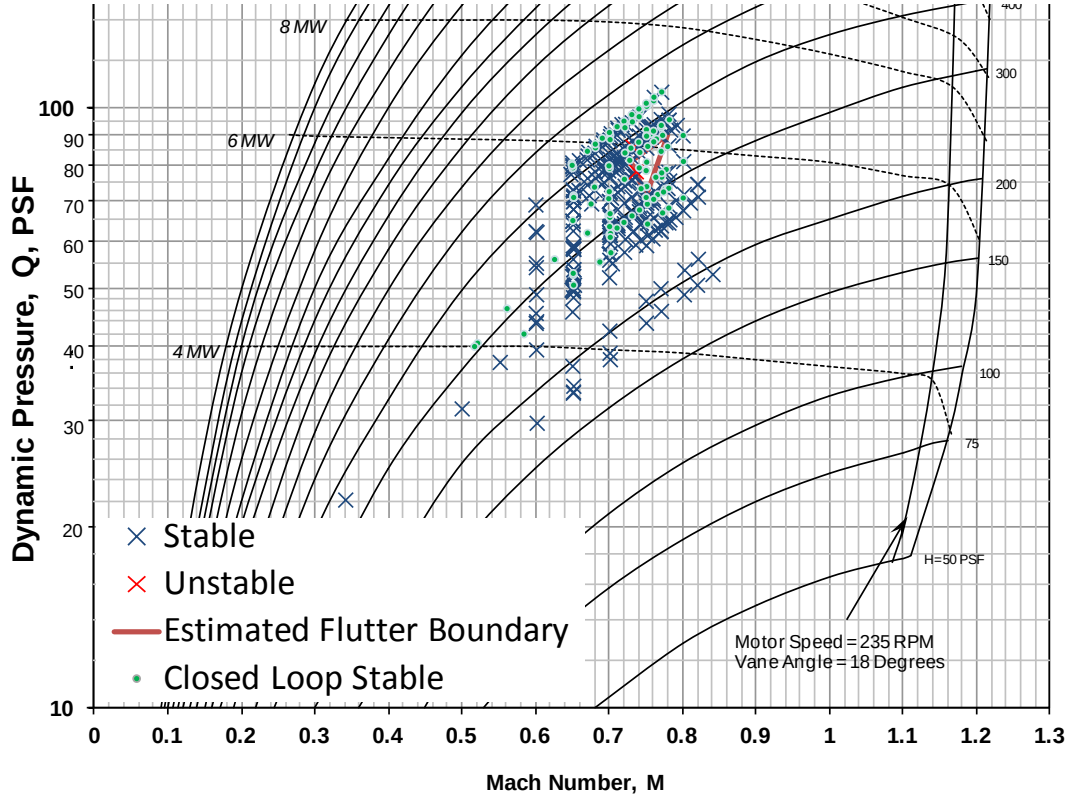

Figure 7.35 – Post-Holiday Closed Loop Stable Alpha = -3

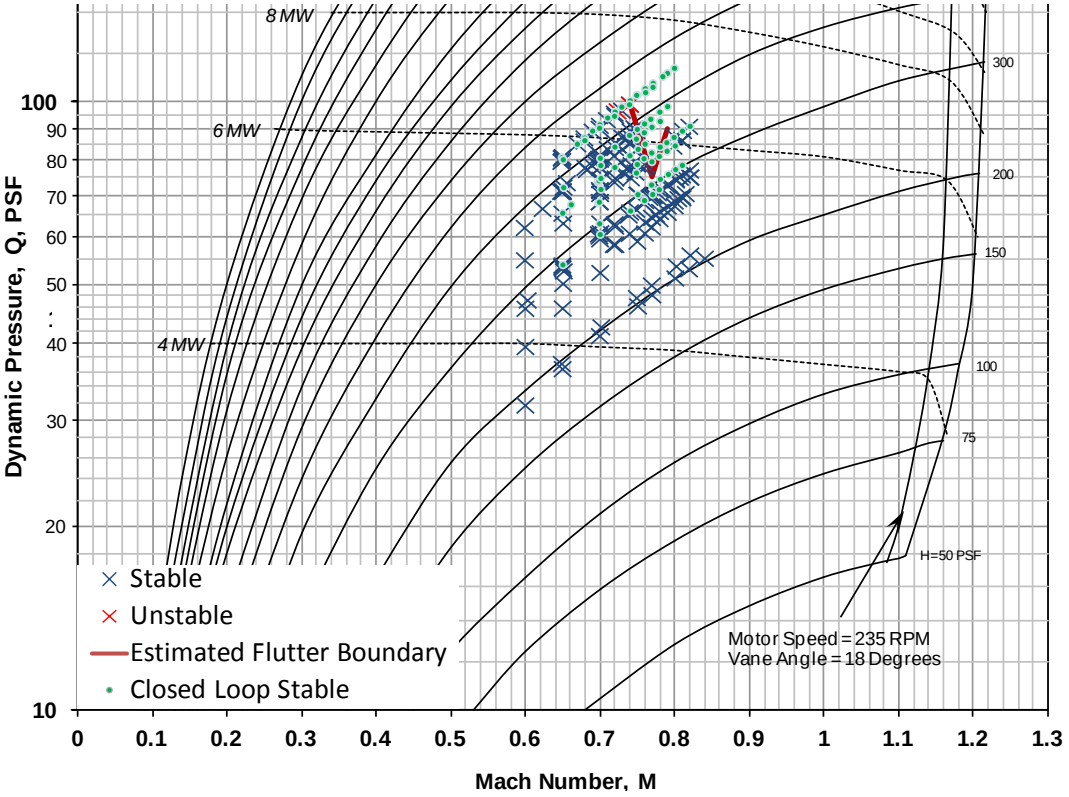

Figure 7.36 – Post-Holiday Closed Loop Stable Alpha = -1

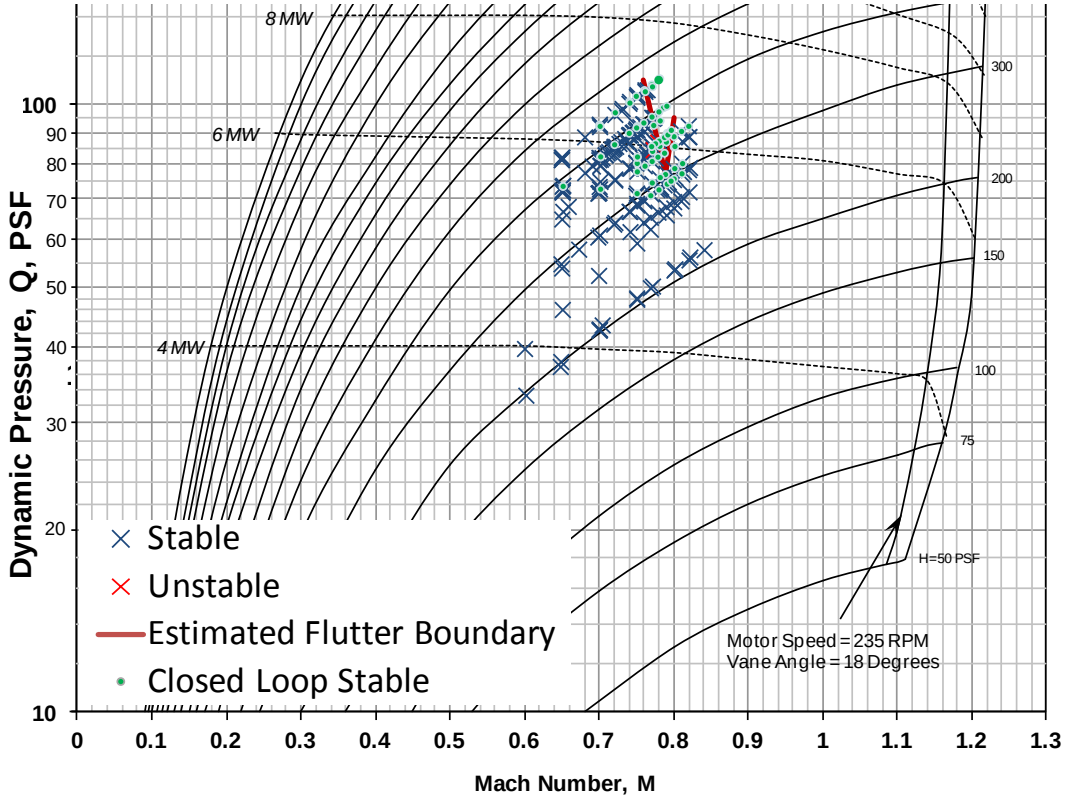

Figure 7.37 – Post-Holiday Closed Loop Stable Alpha = +1

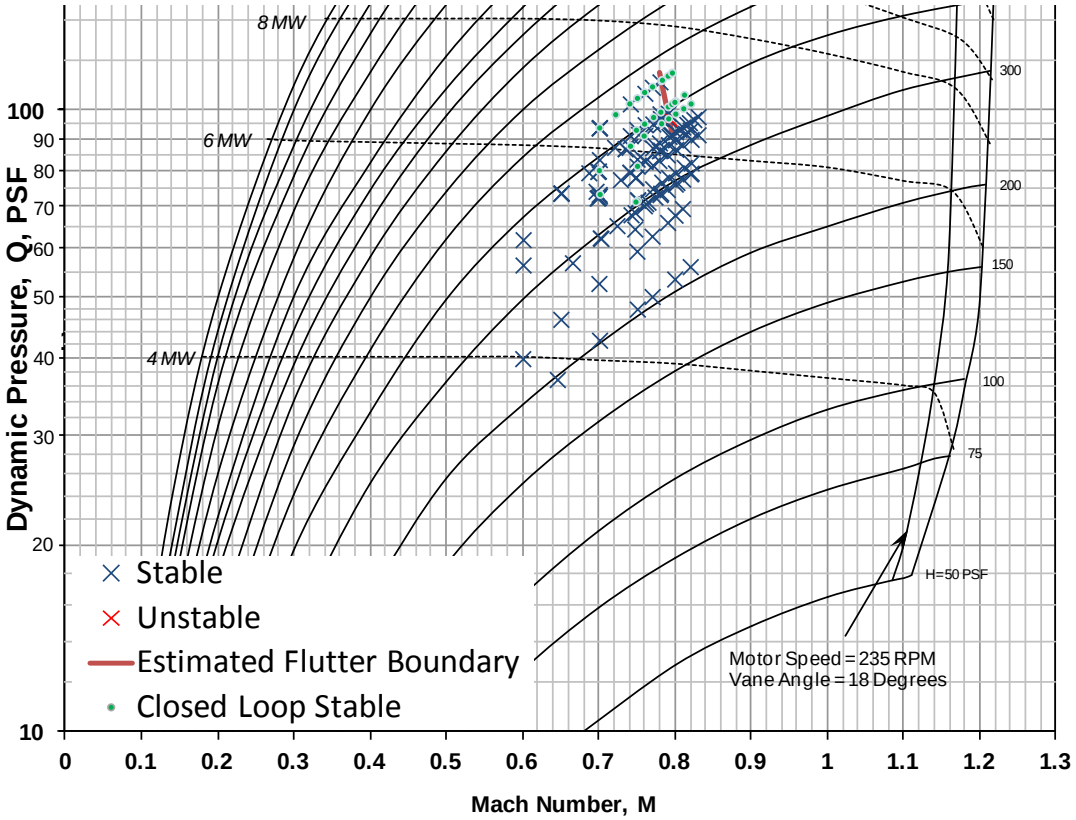

Figure 7.38 – Post-Holiday Closed Loop Stable Alpha = +3

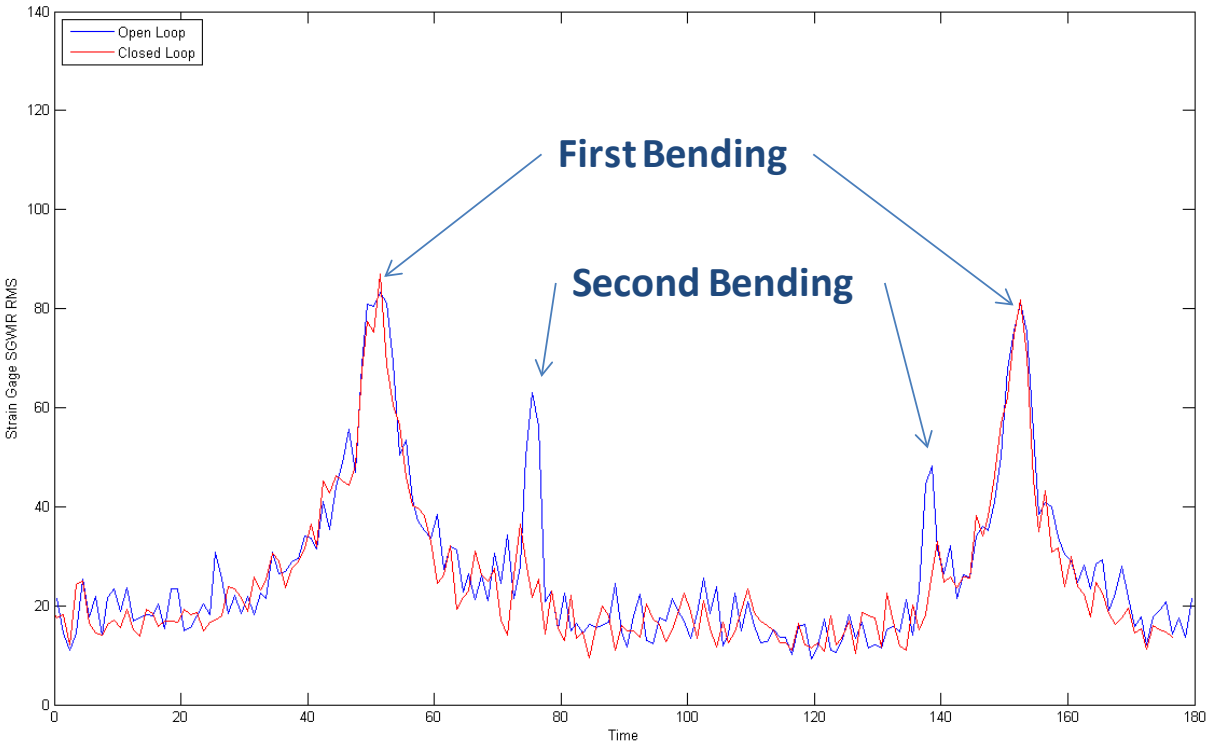

Figure 7.39 – Gust Response RMS Mach = 0.65 Q = 50 Alpha = -3

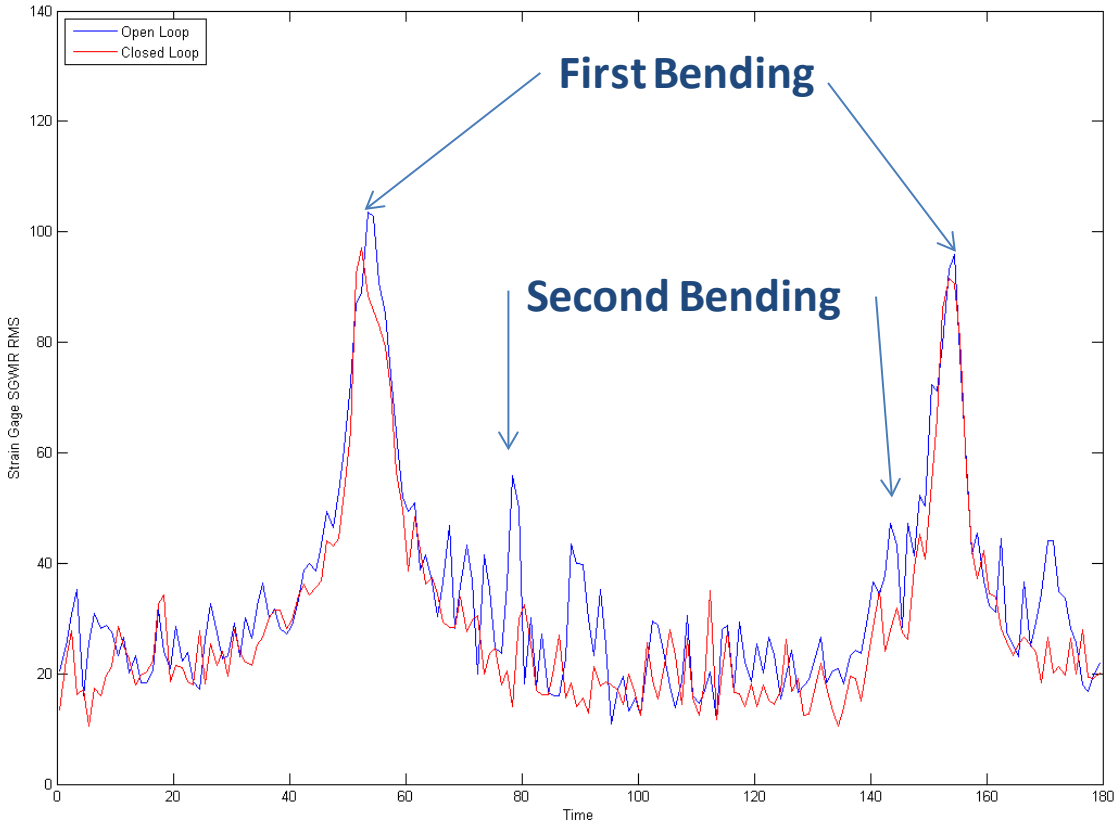

Figure 7.40 – Gust Response RMS Mach = 0.7, Q = 57, Alpha = -3

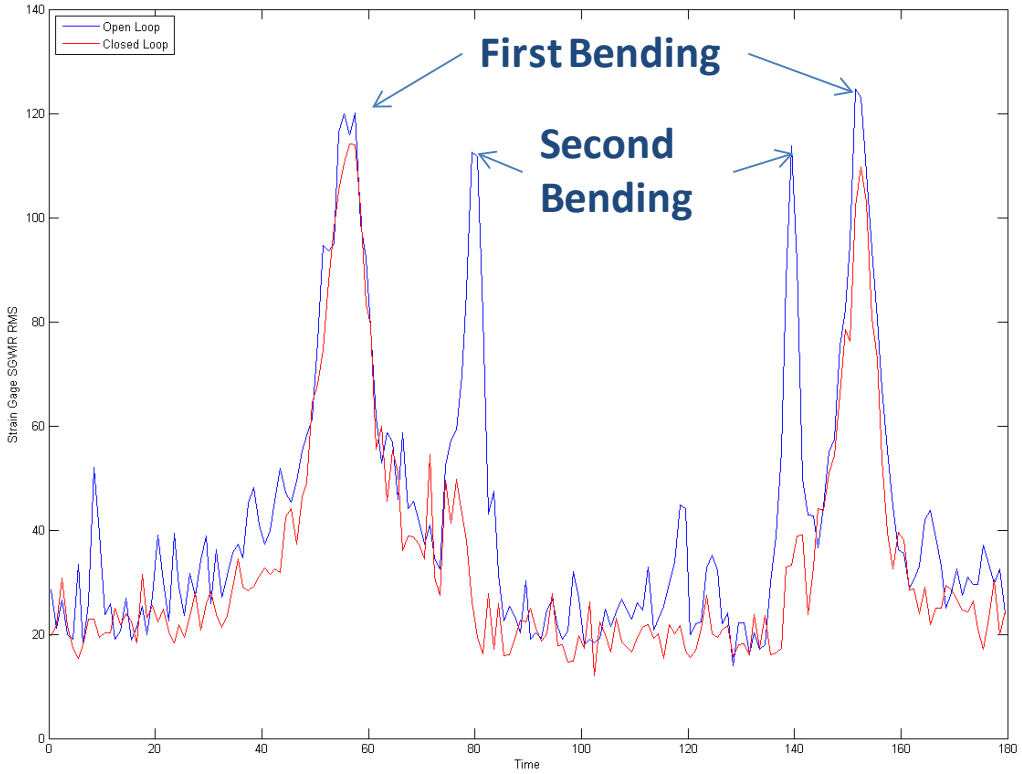

Figure 7.41 – Gust Response RMS Mach = 0.75, Q=64, Alpha = -3

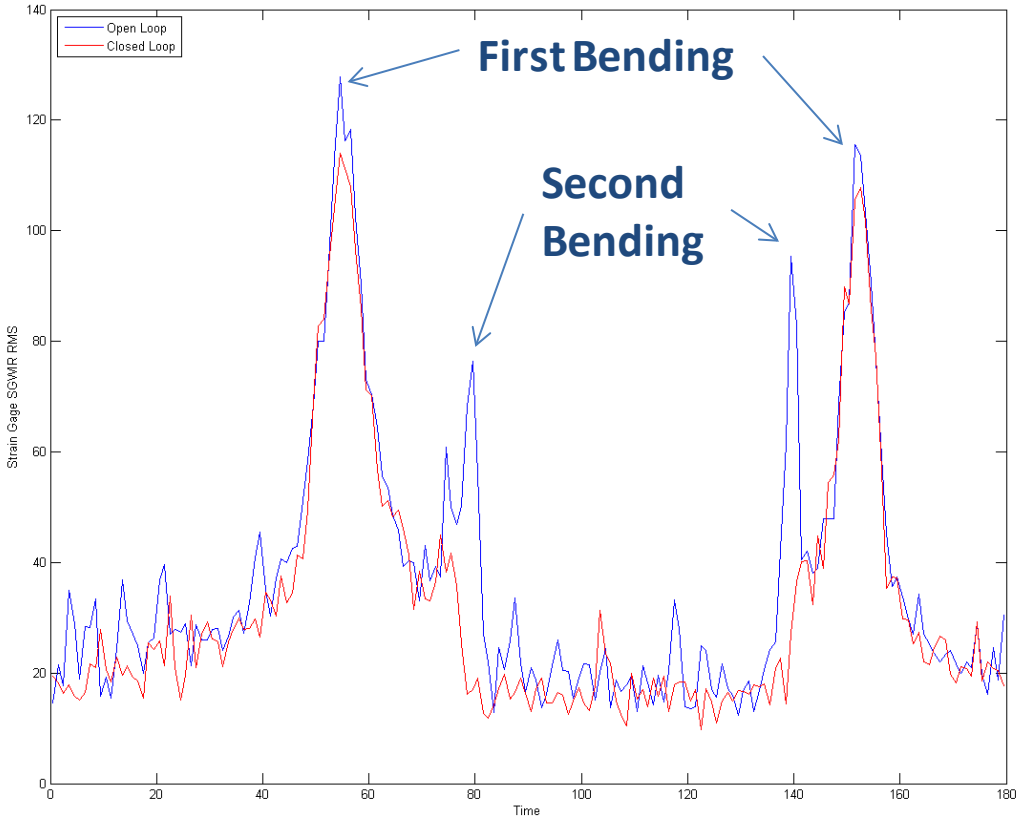

Figure 7.42 – Gust Response RMS Mach = 0.75, Q = 64, Alpha = -1

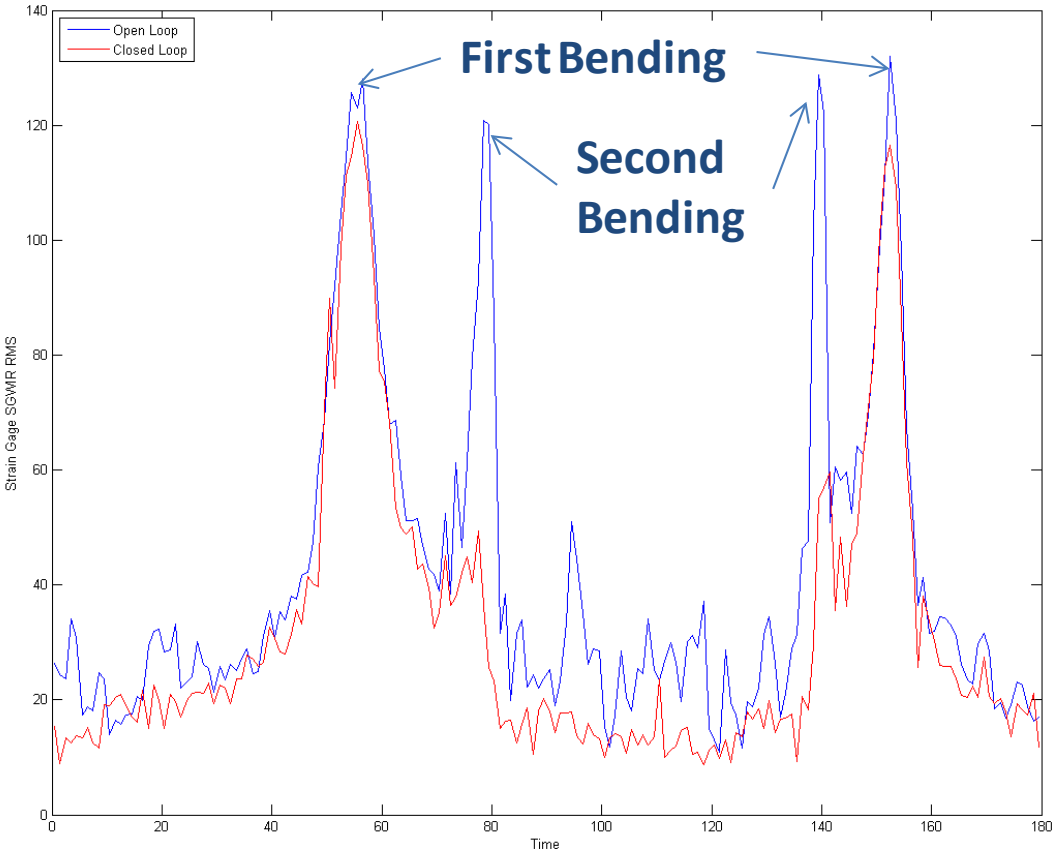

Figure 7.43 – Gust Response RMS Mach = 0.75, Q = 64, Alpha = +1

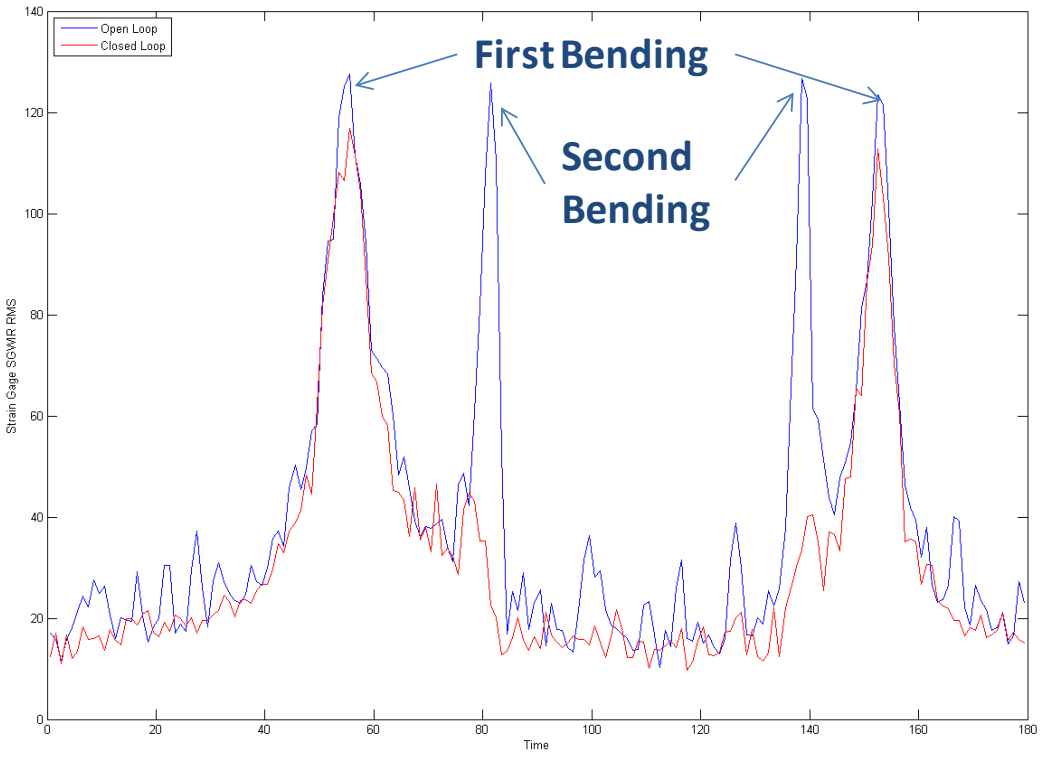

Figure 7.44 – Gust Response RMS Mach = 0.75, Q = 64, Alpha = +3

8.0 Conclusions

1. Analysis accurately predicted the flutter mechanism would be a coalescence of Mode 3 and Mode 4 at around 10 Hz.
2. Flutter results showed significant variation with different angles of attack. This appears to be a characteristic of the TBW configuration. Angle of attack variations are modeled fairly accurately using a non linear method which accounts for preload and large displacement effects.
3. The analysis using theoretical doublet lattice aerodynamics didn't produce the observed sharp decrease in flutter speed with Mach but was fairly accurate in predicting minimum flutter speed. These predictions may not be accurate for different TBW vehicle geometries and/or aerodynamic configurations.
4. No evidence was found of strut buffet causing vibration problems.
5. Flutter suppression was successfully demonstrated using control laws derived from test system ID data and analysis models.
6. Even though the control laws were designed for flutter suppression, the control laws do provide some gust load alleviation as well.

References

1. *Development of Framework for Truss-Braced Wing Conceptual MDO.* **Gur, O., et al., et al.** Orlando : 51st AIAA/ASME/ASCE/AHS/ASC Structures, Structural Dynamics, and Materials Conference, April 12-15 2010. AIAA-2010-2754.

2. **Niu, C. Y. Michael.** *Airframe Structural Design: Practical Design Information and Data On Aircraft Structures.* s.l. : Adaso Adastra Engineering Center, 1999. 9627128090.

3. **Federal Aviation Administration.** Electronic Code of Federal Regulations. *Government Printing Office.* [Online] January 11, 2012. [Cited: January 13, 2012.] http://ecfr.gpoaccess.gov/cgi/t/text/text-idx?c=ecfr&sid=96784884300b9846bc7a9ce5f552f5d3&tpl=/ecfrbrowse/Title14/14cfr25_main_02.tpl. Part 25.

4. **Bradley, Marty K. and Droney, Christopher K.** *Subsonic Ultra Green Aircraft Research: Phase I Final Report.* s.l. : NASA, 2011. CR-2011-216847.

REPORT DOCUMENTATION PAGE

Form Approved
OMB No. 0704-0188

1. REPORT DATE *(DD-MM-YYYY)*	2. REPORT TYPE	3. DATES COVERED *(From - To)*
01- 04 - 2015	Contractor Report	February 2012 - June 2014

4. TITLE AND SUBTITLE

Subsonic Ultra Green Aircraft Research: Phase II – Volume III – Truss Braced Wing Aeroelastic Test Report

5a. CONTRACT NUMBER
NNL08AA16B

5b. GRANT NUMBER

5c. PROGRAM ELEMENT NUMBER

6. AUTHOR(S)

Bradley, Marty K.; Allen, Timothy J.; Droney, Christopher K.

5d. PROJECT NUMBER

5e. TASK NUMBER
NNL11AA00T

5f. WORK UNIT NUMBER
081876.01.07.02

7. PERFORMING ORGANIZATION NAME(S) AND ADDRESS(ES)

The Boeing Company 5301 Bolsa Ave, MC H017-D334
Huntington Beach, California 92647-2099

8. PERFORMING ORGANIZATION REPORT NUMBER

9. SPONSORING/MONITORING AGENCY NAME(S) AND ADDRESS(ES)

National Aeronautics and Space Administration
Washington, DC 20546-0001

10. SPONSOR/MONITOR'S ACRONYM(S)
NASA

11. SPONSOR/MONITOR'S REPORT NUMBER(S)
NASA/CR-2015-218704/Volume III

12. DISTRIBUTION/AVAILABILITY STATEMENT
Unclassified - Unlimited
Subject Category 05
Availability: NASA STI Program (757) 864-9658

13. SUPPLEMENTARY NOTES

Test Report
Langley Technical Monitor: Erik D. Olson

14. ABSTRACT

This Test Report summarizes the Truss Braced Wing (TBW) Aeroelastic Test work accomplished by the Boeing Subsonic Ultra Green Aircraft Research (SUGAR) team, consisting of Boeing Research and Technology, Boeing Commercial Airplanes, Virginia Tech, and NextGen Aeronautics. The model was fabricated by NextGen Aeronautics and designed to meet dynamically scaled requirements from the sized full scale TBW FEM. The test of the dynamically scaled SUGAR TBW half model was broken up into open loop testing in December 2013 and closed loop testing from January 2014 to April 2014. Results showed the flutter mechanism to primarily be a coalescence of 2nd bending mode and 1st torsion mode around 10 Hz, as predicted by analysis. Results also showed significant change in flutter speed as angle of attack was varied. This non-linear behavior can be explained by including preload and large displacement changes to the structural stiffness and mass matrices in the flutter analysis. Control laws derived from both test system ID and FEM19 state space models were successful in suppressing flutter. The control laws were robust and suppressed flutter for a variety of Mach, dynamic pressures, and angle of attacks investigated.

15. SUBJECT TERMS

Aerodynamics; Aeroelastic testing; Control law; Dynamic scaling; Finite-element analysis; Flutter suppression; Ground vibration testing; Non-linear flutter; State space; System identification

16. SECURITY CLASSIFICATION OF:			17. LIMITATION OF ABSTRACT	18. NUMBER OF PAGES	19a. NAME OF RESPONSIBLE PERSON
a. REPORT	b. ABSTRACT	c. THIS PAGE			STI Help Desk (email: help@sti.nasa.gov)
					19b. TELEPHONE NUMBER *(Include area code)*
U	U	U	UU	87	(757) 864-9658